

MOLECULAR DYNAMICS MODELING AND CHARACTERIZATION OF
GRAPHENE/POLYMER NANOCOMPOSITES

by

REZWANUR RAHMAN

Dr. ANWARUL HAQUE, COMMITTEE CHAIR

Dr. SAMIT ROY
Dr. MARK E. BARKEY
Dr. MARK WEAVER
Dr. JIALAI WANG

A DISSERTATION

Submitted in partial fulfillment of the requirements
for the degree of Doctor of Philosophy
in the Department of Aerospace Engineering and Mechanics
in the Graduate School of
The University of Alabama

TUSCALOOSA, ALABAMA

2012

Copyright Rezwanur Rahman 2012
ALL RIGHTS RESERVED

ABSTRACT

The current work focuses on the characterization of graphene based nanocomposites using molecular dynamic simulation and multiscale modeling approaches. Both graphene-epoxy and graphene-cellulose nanocomposites were considered in this study. A hierarchical multiscale modeling approach has been proposed using peridynamics and molecular dynamics simulation.

Firstly, the mechanical properties of crosslinked graphene/epoxy (G-Ep) nanocomposites were investigated by molecular mechanics (MM) and molecular dynamics (MD) simulations. The influence of graphene's weight concentration, aspect ratio and dispersion on stress-strain response and elastic properties were studied. The MD models were further analyzed through the radial distribution function (RDF), molecular energy and atom density. Both the amorphous and the layered structures of G-Ep nanocomposites were considered in order to study the effect of graphene dispersion on elastic properties. A polymer consistent force field (pcff) was used throughout the analysis. Each of the G-Ep system underwent an NVT (constant number of atoms, volume and temperature) and an NPT (constant number of atoms, pressure and temperature) based equilibration followed by finite deformation. The stress-strain responses were evaluated from MD simulations for both amorphous and layered-graphene unit cells in order to determine elastic constants. Moreover, MM was also used to calculate Young's modulus and shear modulus. The results show significant improvement in Young's modulus and shear modulus for the G-Ep system in comparison to the neat epoxy resin. It appears that the RDF, molecular energy and aspect ratios are influenced by both graphene concentrations and aspect ratios. The graphene concentrations in the range of 1-3% are seen to improve Young's modulus and shorter graphenes are observed to be more effective than larger ones. In addition, the dispersed

graphene system is more promising in enhancing in-plane elastic modulus than the agglomerated graphene system. The cohesive and pullout forces versus displacements data were plotted under normal and shear modes in order to characterize interfacial properties. The cohesive force is significantly improved by attaching the graphene with a chemical bond at the graphene-epoxy interface. The elastic constants determined by molecular modeling showed a good agreement with the nanoindentation test results.

In the second part of the work, cellulose was considered to study the mechanical properties of graphene-cellulose bionanocomposite. Multiple number of cellobiose repeat units were connected together to obtain long cellulose chains. Similar to the previous study, the effect of graphene's weight concentration, aspect ratio and dispersion was studied by considering the amorphous and the layered graphene-cellulose systems. Each unitcell was equilibrated using the NVT and NPT molecular dynamics. Uniaxial deformation was applied in order to obtain stress-strain response. The Young's moduli were calculated from the linear portion of the stress-strain responses. Similar to graphene-epoxy systems, the effect of graphene dispersion and agglomeration were studied in the stress-strain plots of graphene-cellulose system. A pcff forcefield was used to define intermolecular and intramolecular interactions. The effect of graphene's aspect ratio and weight concentration on the structural property of each unitcell was analyzed in terms of the radial distribution function (RDF), molecular energy, pairwise bond stretch and angle bending. The interfacial properties between graphene and cellulose were studied by analyzing both cohesive and pullout separation of graphene from cellulose matrix. Finally, the Young's moduli calculated from the MD simulation was compared with the tensile test data. The MD results showed a reasonable agreement with the tensile test results. It was

addressed that incorporating graphane in cellulose matrix enhances the mechanical property of the cellulose based bio-polymer systems.

In the third part of the work, a hierarchical multiscale modeling framework was established between peridynamics and molecular dynamics simulation using an intermediate coarse grained atomic model. The peridynamics formulation is based on continuum theory implying nonlocal force based interaction. It means, continuum points are separated by a finite distance and exert force upon each other. Peridynamics applies integral equations rather than partial differential equations as used in the classical continuum mechanics. Hence, the peridynamics (PD) and the molecular dynamics (MD) have similarities since both use a nonlocal force based interaction. In this work PD based continuum model of graphene-epoxy (G-Ep) nanocomposite is defined by the Lagrangian PD particles. Atomistic model is coupled with PD model through a hierarchical multiscale framework. The PD particles at a coarse scale interact with the fine scale PD particles by transferring pressure, displacements and velocities among each other. Based on the same hierarchical coupling method, a fine scale PD model is seamlessly interfaced with the atomistic model through an intermediate mesoscale region i.e. coarse-grain model. At the end of this hierarchical downscaling, the information such as the deformation, energy and other important parameters were captured in the atomistic region under the applied force at micro and macro regions. The change in atomistic domain is used to update the coarser PD models by introducing a hierarchical upscaling formulation. A simple two dimensional plate of neat epoxy was considered for a complete demonstration of such multiscale simulation platform. Displacements at different scales were analyzed in order to show the validity of the proposed multiscale model. Afterward, the model was applied to a graphene-epoxy plate with an edge crack. The region near the crack tip is interfaced with atomistic model by applying

proposed hierarchical coupling method. The crack opening displacements were discussed at different scales. Finally, the multiscale framework was demonstrated with a 3D nanoindentation problem. The displacements at different scales during nanoindentation were compared. A benchmark analysis was also carried out to determine crack opening displacement (COD) in an edge cracked graphene sample using FEA, PD and MD simulation. The results showed good agreement between PD and MD simulation but FEA results addressed to have comparatively higher COD values. The results from peridynamic based framework for hierarchical multiscale modeling showed reasonable agreement between different PD and atomistic models.

DEDICATION

This dissertation is dedicated to my parents, grandparents, my sister and my brother in law.

LIST OF ABBREVIATIONS AND SYMBOLS

MD	Molecular dynamics
MM	Molecular mechanics
σ_{ij}	Stress tensor
C_{ij}	Stiffness components
ε_{ij}	Strain tensor
AR-LW	Length to width aspect ratio
AR-LT	Length to thickness aspect ratio
G-Ep-Nc	Amorphous graphene-epoxy model
SGM-G-Ep	Stacked graphene-epoxy model
ExpGEP	Graphene-epoxy sample for nanoindentation test
RDF	Radial distribution function
GC	Amorphous graphene-cellulose model
SGM-GC	Stacked graphene-cellulose model
Exp-G-C	Graphene-cellulose sample for tensile test
PD	Peridynamics
CG	Coarse-grain
PFHMM	Peridynamics framework based hierarchical multiscale model

ACKNOWLEDGMENTS

Firstly, I am thankful to almighty whose guidance and help was always with me during the completion of this work. I am expressing my deep gratitude and indebtedness to my adviser Dr. Anwarul Haque, the chairman of the thesis committee for his continuous assistance, support, encouragement and advice during this research. I'm also thanking Dr. Mark E. Barkey, Dr. Jialai Wang, Dr. Mark Weaver and Dr. Samit Roy for their valuable suggestions regarding the work.

I am thankful to my parents and sister for their consistence encouragement from thousand miles. This dissertation is a gift for them.

Finally, I am really grateful to the department of Aerospace Engineering and Mechanics, the University of Alabama and NSF EpscoR program for supporting my research.

CONTENTS

ABSTRACT.....	ii
DEDICATION.....	vi
LIST OF ABBREVIATIONS AND SYMBOLS	vii
ACKNOWLEDGMENTS	viii
LIST OF TABLES.....	xiii
LIST OF FIGURES	xiv
1. INTRODUCTION	1
2. LITERATURE REVIEW	7
3. FUNDAMENTALS OF MOLECULAR DYNAMICS SIMULATION.....	15
3.1. Molecular Interactions	16
3.2 Energy minimization.....	19
3.3 Algorithms in MD simulation.....	20
3.4 Ensemble average in MD simulation.....	22
3.5 Boundary conditions	25
3.6 Atomistic Stress Calculation.....	26
3.7 Evaluation of elastic modulus using MM method	27
3.8 Stress-strain response using MD method.....	28
3.9 Interfacial Interactions	29
4. MODELING AND CHARACTERIZATION OF GRAPHENE-POLYMER NANOCOMPOSITES	30
4.1 Molecular modeling and nano-characterization of graphene-epoxy	

Nanocomposites	30
4.1.1 Amorphous graphene-epoxy model	31
4.1.2 Stacked graphene-epoxy model	33
4.1.3 Interface model	34
4.1.4 Computational Details	36
4.1.4.1 Amorphous models	36
4.1.4.2 Stacked graphene models	38
4.1.4.3 Interface models	39
4.1.5 Nanoindentation tests.....	39
4.1.5.1 Nanoindentation test procedure	39
4.1.5.2 Nanoindentation test results.....	43
4.1.6 Results and Discussion from molecular modeling.....	44
4.1.6.1 Radial distribution function (RDF).....	45
4.1.6.2 Atom density.....	45
4.1.6.3 Molecular energy	46
4.1.6.4 Effect of graphene concentrations and aspect ratios on elastic constants	47
4.1.6.5 Dispersion and agglomeration effects.....	52
4.1.6.6 Interfacial property.....	54
4.1.7 Conclusion	57
4.2 Molecular modeling and nano-characterization of graphene-cellulose Nanocomposites	58
4.2.1 Molecular modeling and simulation details	58
4.2.1.1 Amorphous models	59

4.2.1.2 Stacked graphene-cellulose models	61
4.2.1.3 Interface models	63
4.2.2 Results and discussion	64
4.2.2.1 Effect of graphene concentrations and aspect ratios on stress-strain response	64
4.2.2.2 Structural configurations	68
4.2.2.3 Energy evolution during deformation process	70
4.2.2.4 Bond stretch and bond angle evolution during deformation process	71
4.2.2.5 Effect of graphene dispersion on elastic property of graphene-cellulose nanocomposites	73
4.2.2.6 Interfacial Property between graphene and cellulose	75
4.2.3 Conclusion	77
5. MULTISCALE SIMULATION OF GRAPHENE-EPOXY NANOCOMPOSITES USING PERIDYNAMICS AND MOLECULAR DYNAMICS.....	79
5.1 Fundamental Formulation of Peridynamics.....	79
5.2 Hierarchical Multiscale Modeling	83
5.2.1 Top-down PFHMM	84
5.2.2 Bottom-up PFHMM.....	87
5.3 Numerical Experiments and Results	92
5.3.1 Two Dimensional (2D) Plate under Axial Load	92
5.3.2 Two Dimensional (2D) Plate with Edge Crack	98
5.3.3 Three Dimensional (3D) Nanoindentation Problem	103
5.4 Benchmark analysis between FEA, PD and MD	108
5.4.1 Case-I	108

5.4.2 Case-II.....	109
5.5 Conclusion	112
6. CONCLUSION.....	113
7. REFERENCES	114
APPENDIX.....	119
A1. Parametric study of cutoff distance in PD models.....	119

LIST OF TABLES

Table 1. Material configurations of G-Ep amorphous system.....	33
Table 2. Material configurations of SGM-G-Ep system.....	34
Table 3. Unit cell configuration for interface model	36
Table 4. Effect of graphene concentrations and aspect ratio on elastic constants.....	51
Table 5. Comparison of Young’s modulus obtained from MD simulation and nanoindentation tests.....	51
Table 6. Young’s modulus calculated from stress-strain response for stacked graphene model.....	54
Table 7. Material configurations of each graphene-cellulose unitcell.....	60
Table 8. Unit cell configuration for stacked graphene models	62
Table 9. Unit cell configuration for interface model	64
Table 10. Calculated Young’s modulus for amorphous graphene-cellulose systems.....	67
Table 11. Young’s modulus calculated from stress-strain response for semi-crystalline model.....	75

LIST OF FIGURES

Figure 1. Different components of forcefield	15
Figure 2. Schematic diagram of 2D periodic boundary condition.....	26
Figure 3. Schematic diagram of developing amorphous model for graphene epoxy.....	33
Figure 4. Schematic diagram of stacked graphene model (SGM).....	34
Figure 5. Mode-I and Mode-II interface model of G-Ep system.....	35
Figure 6. Typical temperature, total energy and pressure plots at different times	38
Figure 7a. SEM image of the sectional surface of ExpEpon	41
Figure 7b. SEM image of the sectional surface of ExpGEp-1%	41
Figure 7c. SEM image of the sectional surface of ExpGEp-3%.....	41
Figure 7d. SEM image of the sectional surface of ExpGEp-5%	41
Figure 8. Schematic diagram of nanoindentation test method.....	42
Figure 9. Load vs. displacement curve during nanoindentation	44
Figure 10. RDF of any pair of atoms in graphene-epoxy amorphous system (Left: AR-LT 150 and Right: AR-LT 480)	45
Figure 11. Atom densities in different graphene-epoxy unitcells.....	46
Figure 12. Molecular energy in amorphous systems with type-a and type-b graphenes	47
Figure 13. Stress-strain response of amorphous system with type-a and type-b graphenes	50
Figure 14. Stress-strain response in xx, yy and zz directions for	

SGM-G-Ep-I	53
Figure 15. Stress-strain response in xx, yy and zz directions for SGM-G-Ep-II.....	53
Figure 16. Stress-strain response in xx, yy and zz directions for SGM-G-Ep-III.....	54
Figure 17. Force vs displacement curve for Mode-I cases	56
Figure 18. Force vs displacement curve for Mode-II cases	56
Figure 19. Force vs displacement curve for mode-I-a-with chemical bonding system.....	56
Figure 20. Graphenes (Type-a or Type-b) embedded in cellulose matrix to form amorphous graphene-cellulose system.....	60
Figure 21. Schematic diagrams for cellulose based stacked graphene models.....	62
Figure 22. Mode-I and Mode-II separation of graphene from cellulose matrix	63
Figure 23. Stress-strain response of graphene/cellulose systems with type-a graphene.....	66
Figure 24. Stress-strain response of graphene/cellulose systems with type-b graphene.....	66
Figure 25. Stress-strain response of graphene/cellulose from tensile tests	68
Figure 26. Radial distribution function of amorphous graphene-cellulose system with type-a (Left) and type-b (Right) graphene.....	69
Figure 27. Radial distribution function for carbon-carbon atoms in amorphous graphene-cellulose system with type-a (Left) and type-b (Right) graphene	70
Figure 28. Change in potential energy in different amorphous systems Left: type-a and Right: type-b.....	71
Figure 29. Pairwise bond stretch under applied strain in different amorphous systems Left: type-a and Right: type-b	72

Figure 30. Bond angle evolution under applied strain in different amorphous systems Left: type-a and Right: type-b	72
Figure 31. Stress-strain response of SGM with single graphene	74
Figure 32. Stress-strain response of SGM with agglomerated graphenes	74
Figure 33. Stress-strain response of SGM with dispersed graphenes	75
Figure 34. Force vs displacement plot of graphene in Mode-I-a and Mode-I-b cases.....	76
Figure 35. Force vs displacement plot of graphene in Mode-II-a and Mode-II-b cases	77
Figure 36. A schematic diagram of PD model.....	82
Figure 37. A schematic diagram of PFHMM	84
Figure 38. A schematic diagram of top-down PFHMM.....	86
Figure 39. Coarse-grain model contains polymer molecules.....	87
Figure 40. A schematic diagram of bottom-up PFHMM.....	91
Figure 41. A schematic diagram of closed-loop PFHMM.....	91
Figure 42. Displacement vs. positions at different scales.....	95
Figure 43. Displacement fields at different scales	98
Figure 44. Illustration of 2D crack problem using PFHMM	100
Figure 45a. Crack opening displacement vs. time in peridynamic model S_0	102
Figure 45ab Crack opening displacement vs. time in peridynamic model C_0	102
Figure 45c. Crack opening displacement vs. time in peridynamic model A_0	102
Figure 46. Schematic diagram of PFHMM for a nanoindentation problem	105

Figure 47a. Displacement fields in S and S_0 on YZ-plane	107
Figure 47b. Displacement fields in S_0, S_1, S_2 and S_3 on YZ-plane	107
Figure 47c. Displacement fields in S_3, C_0 and A_0 on YZ-plane	107
Figure 47d. 3D Displacement fields in S_0, S_1, S_2 and S_3	107
Figure 48. Different graphene sheet models	108
Figure 49a. Y-displacements at different X-locations	109
Figure 49b. Y-displacements at different timesteps	109
Figure 50. FEA, PD and MD graphene models with edge crack.....	110
Figure 51. COD from PD, FEA and MD models	110
Figure 52. FEA and MD model of graphene sheet	112
Figure 53. COD (at $x=0$ along the crack length) from FEA and MD models	112
Figure 54. Stress-strain responses for different cutoff distances	120

CHAPTER 1

INTRODUCTION

Graphene is a two dimensional structure with sp^2 bonded carbon atoms. It possesses almost all the characteristics of carbon nanotubes (CNTs), and it is comparatively affordable. Hence graphene is considered one of the most popular nano-reinforcing materials in wide variety of applications. Polymer nanocomposites are known to exhibit enhanced mechanical, electrical, thermal or magnetic properties with respect to neat polymeric materials. The outstanding properties of nanofiller make nanocomposites a novel alternative to conventional polymeric materials. In last few years, researchers have been investigating the mechanical, electrical and thermal properties of CNT reinforced nanocomposites. Among several types of polymer resins, thermoset epoxy (such as EPON 862) is known to be very compatible for modern light weight structures. It has been noticed that the properties of epoxy has been improved with CNT. CNT are expensive, however, which limits the application of CNT/epoxy nanocomposites in different aerospace and automobile applications. The issue is resolved when comparatively cheaper manufacturing process was invented for graphene [1]. Hence, scientists and engineers have been directing attention on graphene reinforced epoxy nanocomposites. Moreover, CNT has a higher strength only along the longitudinal direction whereas a 2D graphene sheet is strong in both longitudinal and transverse directions.

Along with synthetic polymers, scientists are also being interested in biopolymer based nanocomposites. Cellulose has been considered to be good candidate for its enormous advantages. Cellulose is environmentally friendly and biodegradable. It is suitable for different biomedical applications, comparatively cheaper than synthetic polymer and is abundant in

nature. As a matter of fact, cellulose has higher Young's modulus than Epoxy polymers ($E_{\text{epoxy}}=3$ GPa, $E_{\text{cellulose}}=10$ GPa). Cellulose can be manufactured in both crystalline and amorphous forms. It was observed that the amorphous portion of cellulose is more accessible than the crystalline form. Thus, a rigorous study of both graphene/epoxy and graphene/cellulose nanocomposites is necessary due to their high potential in many biomedical and green composites applications.

A critical part of investigating nanocomposites is predicting its mechanical properties (such as Young's modulus and interfacial load transfer) which can be incorporated into further macroscopic applications. Typically, it is possible to determine mechanical properties of neat polymer as well as nanocomposites experimentally. Introducing graphene nanoplatelets into polymer however, creates a new challenge due to its tendency to retain its layered structure i.e. graphite. Van der Waals force among the graphene layers leads to form graphite which is typically nanometers to micron thick. It is quite challenging to exfoliate all the graphenes in the polymer solution and produce nanocomposites. Besides Young's modulus, assessing interfacial properties between nanofiller and polymer is another challenging task due to experimental limitations in probing material properties at nanoscale. The interfacial properties are controlled at the atomistic level. The macroscopic mechanical properties of nanocomposites depend on the load transfer property between nanofillers and a polymer matrix. Hence, a computational model is potentially very useful in predicting mechanical properties. The best choice in this regard is molecular dynamics simulation of graphene-polymer nanocomposites.

Molecular dynamics (MD) simulation is a powerful and modern tool for numerical experiments. It is potentially suitable for characterizing new materials without synthesizing them. One of the aims of atomistic simulation is to reproduce experiments to elucidate the invisible microscopic details and further explain experiments. On the other hand, simulation can

also be used as a useful predictive tool. The fundamental concept behind molecular dynamics is to apply Newton's equations of motion in solving multi-body interacting system (i.e. polymers, crystals, nanocomposites etc). The macroscopic mechanical properties are approximated to the averaged properties calculated from a large number of replicated systems where each system consists of thousands of atoms. This is only possible by introducing concept of statistical ensemble in multi-atom molecular dynamics model [2]. The molecular interactions are the vital parts in MD simulation. Molecular interactions are defined by an appropriate force-field. The key components of a force-field are bonded interactions and non-bonded interactions such as van der Waals force. These interactions make molecular dynamics simulation to be a primary tool in assessing interfacial properties between nanofiller and polymer matrix. The equations of motion for these particles which interact with each other via intra-molecular and inter-molecular potentials can be solved accurately using various numerical integration methods such as the common predictor-corrector or Verlet methods. Molecular dynamics efficiently evaluates different configurational properties and dynamic quantities which are not achievable by Monte Carlo method [2].

Various phenomena in material science involve processes over a wide range of length scales from the atomistic to the continuum. A deeper understanding of solids particularly nanocomposites detect that the multiscale analysis is required in identifying the effects of structural parameters at the nanoscale. In this study two scales are considered: continuum mechanics and the molecular dynamics. In continuum mechanics (*coarse* scale) atomistic details are neglected, whereas in molecular dynamics (*fine* scale) the atoms and their mechanics are accounted for. The continuum mechanics is based on partial differential equations describing the conservation laws and the constitutive relations. This approach is effectively implied in solid

mechanics problems. However, it may become inaccurate for problems in which the detailed atomistic processes affect the macroscopic behavior of the material. On the other hand, the theoretical understanding of the atomic level mechanisms of deformation leads to the conclusion that atomistic simulation techniques should be the most appropriate tool for analyzing nanocomposites. The drawback of the fine scale simulation is the overwhelming demand on calculation speed and the large amount of data. Thus, employing a multiscale strategy for an efficient and accurate modeling seems favorable. By separating the problem into two different frameworks, the accuracy of a fine scale model can be combined with the advantages of a computationally efficient model. A comparably small region of atoms surrounding any region of interest is modeled by molecular dynamics. Outside of this region, far from the region of interest, we take advantage of the fact that the displacement is almost homogeneous and can thus be modeled efficiently by a linear elastic continuum model.

The proposed research has three major parts:

- Molecular dynamics modeling of two types of nanocomposites (graphene/epoxy and graphene/cellulose) in order to calculate the mechanical property such as Young's modulus, interfacial property and comparing the theoretically calculated results with experimental data
- Develop a multiscale modeling framework between this atomistic model and continuum model
- Experimental characterization of the graphene-epoxy nanocomposites

The details about different segments of this work are outlined as follows:

Molecular dynamics modeling

- Develop the molecular models of synthetic nanocomposite: graphene-epoxy and bionanocomposite: graphene-cellulose
- Address the effect of graphene weight concentration (1%, 3%, 5%), aspect ratio (150, 480) on stress-strain response of graphene-epoxy and graphene-cellulose systems
- Study the effect of graphene dispersion and agglomeration on the stress-strain response using layered-graphene-epoxy and layered-graphene-cellulose systems
- Calculate the elastic moduli from the linear portion of the stress-strain curves
- A rigorous analysis of structural property of the amorphous models by considering radial distribution function (RDF), molecular energy, bond stretch and angle bending
- Study the force-displacement curve for debonding of graphene from the polymer (epoxy and cellulose) in longitudinal and transverse directions in order to obtain interfacial property

Multiscale modeling

- Use peridynamics (PD) modeling in order to define continuum scale problem
- Develop a PD based hierarchical multiscale modeling framework (PFHMM) in order to establish a seamless coupling between coarse scale continuum model and atomistic model
- Apply the multiscale modeling frame work in both 2D and 3D solid mechanics problems

- Use PFHMM to study crack opening displacement

Experimental characterization

- Perform nanoindentation test on 1%, 3% and 5% graphene reinforced nanocomposites
- Analyze SEM images of different graphene-epoxy samples in order to study graphene distribution in epoxy matrix

CHAPTER 2

LITERATURE REVIEW

In the last few years, graphene has drawn the attention of the nanoscience community due to its attractive electrical and mechanical properties. It has become one of the most exciting nanomaterials in the century. As a result, graphene's inventor Geim and Novoselov and co-researchers [3] won Nobel prize in the year of 2010. As it was mentioned earlier that a single layer of graphene possesses a higher Young's modulus and is cheaper than CNT, this opens up a new opportunity to introduce this nanomaterial in enhancing the properties of different polymer composites (i.e. epoxy and cellulose based nanocomposites). Epoxy resins are an important class of compounds containing two or more epoxy groups which react with different curing agents consisting of chemical groups like amines and anhydrides. The result is cross-linked epoxy systems which exhibits a series of excellent performance, i.e. high modulus and fracture strength, low creep and high-temperature performance. Hence, many experimental and theoretical studies were carried out in order to explore the properties of epoxy based systems. Wu and Xu [4] performed an MD simulation of cross-linked Diglycidyl Ether Bisphenol A (DGEBA) epoxy with isophorone diamine (IPD) as a curing agent. They determined elastic constants, optimum unit cell dimension and density of the epoxy system. Fan and Yuen [5] also carried out MD simulation for cross-linked Diglycidyl Ether Bisphenol F (EPON 862) epoxy in the presence of curing agent Triethylenetetramine (TETA). They outlined the MD simulation methodology and eventually determined the Young's modulus and the glass transition temperature of the cross-linked network. Bandyopadhyay and co-researchers [6] also have studied the mechanical and

thermal properties of cross-linked epoxy polymer using MD simulation. All these works are entirely based on neat epoxy systems.

Similar to the study on epoxy systems, there has not been much research work carried out on pristine cellulose polymers. Cellulose can be found in both crystalline and amorphous forms. But the amorphous form of cellulose is more easily accessible than the crystalline cellulose. The bulk Young's modulus for amorphous cellulose was calculated by Chen et al. [7] by using MD simulation. They applied uniaxial deformation to an amorphous cell and calculated resulting stress. Besides this work there are few other works available in the literature on cellulose based systems. However, these works are mainly based on crystalline cellulose. Favier et al. [8] used cellulose whiskers as nanofillers with different polymer systems. They reported improvement in mechanical properties and glass transition temperature. Yano et al. [9] addressed the dependence of the mechanical properties of amorphous cellulose on the temperature. So, it has been a matter of interest to study the change in mechanical property of amorphous cellulose after incorporation of graphenes.

Besides epoxy and cellulose systems, substantial work has been performed on pristine graphene. Experimentally, it is difficult to obtain perfectly 2D graphene plates which are completely dispersed. Hence, theoretical studies of graphene's electrical and mechanical properties became quite important. Bu et al. [10] calculated Young's modulus of graphene using molecular dynamics simulation. Frank et al. [11] measured the Young's modulus of stacks of graphene sheets to be as high as 0.5 TPa by nanoindentation using an atomic force microscope. Using the same method, Lee et al. [12] obtained the Young's modulus of 1 TPa and intrinsic breaking strength of 0.13 TPa for a monolayer defect-free graphene sheets. Theoretically, Liu et al. [13] calculated the elastic modulus of 1.05 TPa by phonon density functional perturbation

theory and reported an inherent behavior of brittle cleavage fracture at a low temperature. A continuum mechanics approach was applied by Reddy et al. [14]. They calculated the elastic modulus at equilibrium and non-equilibrium conditions to be 0.7 TPa and 1.0 TPa, respectively. Huang et al. [15] estimated the Young's modulus as high as 4.21 TPa, directly from the interatomic potential. Konstantinova et al. [16] obtained the value of Young's modulus to be approximately 1.24 TPa by ab initio method. So, there is a demand for theoretical and experimental investigation of graphene/epoxy and graphene/cellulose nanocomposites in order to achieve improved properties compared to the neat epoxy and cellulose.

In this context, scientists have been studying properties of epoxy or cellulose based nanocomposites with different types of nanofillers. Yu and others [17] performed an MD analysis of epoxy (EPON 862) nanocomposite with alumina (Al_2O_3) as nanoreinforcement. Their study revealed that the mechanical property is improved by embedding alumina nanofillers in the epoxy matrix. Zhu [18] performed MD simulation on the unit cell consisting of a single wall carbon nanotube (SWNT) and cross-linked EPON 862 epoxy resin to study the stress-strain behaviors. Frankland and co-researchers [19] investigated the effect of polymer-nanotube cross-linking on critical load transfer from carbon nanotubes to polymer matrix by using molecular dynamics (MD) simulation. Zhu calculated the stress-strain behavior of SWNT-epoxy nanocomposites based on molecular dynamics (MD) simulation scheme. He performed MD by deforming the large unit cell followed by calculating average stress in the entire unit cell. Yasmine and Daniel calculated thermal properties and elastic modulus of graphite/epoxy nanocomposites based on experimental study [20]. However, it is quite challenging to prepare graphene-polymer nanocomposites instead of graphite-polymer nanocomposites experimentally as graphene has a tendency to remain in agglomerated form. As a result, the experimentally

calculated mechanical property is influenced by several parameters such as graphene dispersion, load transfer mechanism, void percentage etc. Because it is harder to do experiments than it is to do calculations, researchers focused on theoretical modeling of graphene-polymer nanocomposites. Ji and coworkers [21] developed a micromechanics model for graphene-polymer nanocomposite based on the Mori-Tanaka model. Raiffee et al. [22] used a modified Halpin-Tsai model to compare their experimental results from tensile tests. However, the effect of exfoliation quality, graphene's geometric morphology and void percentage in polymer matrix are difficult to address in a micromechanics model. Micromechanics models consider the homogenized unit cell which is not necessarily the exact scenario in real life problems. The density of polymer chains may not be well distributed throughout the unit cell. Hence some discrepancy remains between experimental observation and micromechanics model [22]. Unlike epoxy, there is no work available in the literature on graphene/cellulose.

Recently, it has been observed that improved mechanical properties of the polymer composites not only depend on the inherent properties of the nanofiller, but also on the quality of matrix-nanofiller interface [23]. The load transfer mechanism between graphene and polymer solely depends on the interfacial bonding. Molecular dynamics modeling is known to be a very useful tool to investigate interfacial properties at nanoscale. In past few years several researchers studied the interfacial bonding between CNT and different polymers [24]. They calculated the pullout strength and critical length of CNT in matrix. As graphene is a 2D material, both pullout (shear) and cohesive strengths (normal) are significantly important. The cohesive interaction between a nanofiller surface and polymer is controlled by the van der Waals force. Awasthi [23] analyzed pullout as well as cohesive interaction in the graphene-polyethylene system using molecular dynamics (MD) simulation. However, the pullout and cohesive properties between

graphene and epoxy are yet to be determined. So far there has been no work noticed in the literature on evaluating interfacial properties of graphene-epoxy or graphene-cellulose nanocomposites.

Over the past decade, various methods have been developed to address different problems involving atomistically large material domains [25]. The most challenging part in atomistic-continuum coupling is the formulation of a seamless connection between material representations at different scales. In coupling atomistic and continuum material representations, the continuity of material properties must be maintained while the transition is made from individual atoms interacting through non-local forces to the local stress-strain field of continuum mechanics. For crack problems, the early efforts of Gumbsch and Beltz [26] developed a finite element-atomistic (FEAt) coupling procedure that combined an embedded MD system with a finite element (FE) domain. Again, in the coupling of length scales (CLS) method [27], the nodes in a two-dimensional plane strain FE model representing the continuum region are connected to a three-dimensional atomic field by a mean field averaging through the thickness. The quasicontinuum (QC) method, reviewed by Miller and Tadmor [28], is formally based on an entirely atomistic description of the material domain. In the QC formulation, non-local representative atoms are used to represent ‘real’ atoms to form atomistic regions treated by molecular dynamics method while local representative atoms are used to define continuum domains by applying both the Cauchy-Born rule [29] and aspects of FEM. Another coupling approach is the bridging method by Xiao and Belytschko [30]. It is based on an overlay approach in which MD and FEM representations are superimposed in an interface region. This method allows interpolated FE nodal displacements to be associated with atomic displacements in the

bridging domain. Though, FE coupled with atomistic models is very useful in multiscale modeling, there are few issues that need to be addressed. These are as follows:

- i) FEM meshing and remeshing for the multiscale analysis is computationally expensive particularly for large deformation, high non-linearity and moving boundaries
- ii) A typical FEM is solely dependent upon mesh-generation and often causes problems in ensuring a smooth and seamless transition from the atomic to continuum sub-domains

The above issues can be mitigated by introducing a meshfree method in coupling with atomistic scale. Recently, various meshfree, approaches have been proposed. Some meshfree methods are based on the strong-forms and the meshfree shape functions, such as the finite point method [31], meshfree collocation method [32] and some are based on global or local weak-forms and meshfree shape functions. Typical examples are the element-free Galerkin (EFG) method [33], the radial point interpolation method (RPIM) [34], the meshless local Petrov-Galerkin (MLPG) method and local radial point interpolation method (LRPIM) [35, 36]. Wang et al. [34] developed a coupling methodology between a meshfree model defined by element free Galerkin (EFG) method and molecular dynamics model. All of these continuum meshfree methods solely rely on the classical theory of solid mechanics which requires continuously differentiable displacement field. This leads to some difficulties in modeling discontinuities in the continuum model. Thus, seamless coupling between different scales is also becomes quite challenging while fine scale atomistic models are discrete. Moreover, for concurrent method the continuum model needs to be scaled down to atomistic scale in order to exchange information with atomistic scale through handshake region. This becomes an issue using the existing methods such as FEA or meshfree methods. These issue are resolved by introducing “Peridynamics modeling” of solids [37, 38]. In peridynamic theory, the governing partial differential equations

of classical solid mechanics are replaced by integral or integro-differential equations. These equations are based on nonlocal interactions among the material points in a body which interact to each other at a certain distance. Another type of continuum modeling formulation is the material point method (MPM). MPM was first developed by Sulsky et al. [39] which uses the particle in cell algorithm. MPM has been used in several linear and non-linear problems as an effective alternative solution of FEA. In recent years researchers have been using MPM as a continuum solver in different multiscale and mutiphysics problems [40-47]. Ma et al. and Lu et al. [48,49] introduced the concurrent atomistic-continuum coupling using MPM and MD simulation. However, all of these abovementioned atomistic-continuum coupling methods were applied to crystal structures. This is very challenging if the atomistic model is for amorphous polymer. Hence it has become an interesting topic to develop a multiscale modeling framework for polymeric materials. Roy and Nair introduced a generalized MPM-MD based concurrent coupling scheme for polymer nanocomposites using the embedded statistical method [25, 50]. They showed that the MPM-atomistic coupling scheme can be applied to solve multiscale fracture mechanics problems. Though MPM is a particle based method, it does not consider the mutual interaction among the particles through mutibody interaction. The formulation is different than the MD simulation. So on this context PD can be good alternative to FEA or MPM as it accounts for mutibody interaction and incorporates them into the governing equations of continuum mechanics and incorporated into a molecular dynamics package (i.e. LAMMPS) [51, 52].

Silling developed the peridynamics formulation by introducing the integral equation in the “equation of motion” and the “equilibrium equation” of continuum mechanics [37]. Later on, several works have been carried out on different aspects of peridynamics formulation and its

application in multiscale modeling, fracture mechanics etc. Seleson et al. [38] concluded that the peridynamics model can be considered as an upscaling of classical molecular dynamics based on the similarity in discrete formulation of both of these models. Using this concept, it is possible to develop a seamless multiscale continuum model which can be focused down to atomistic scale. However, atomistic models become computationally expensive with respect to dimension of the system. A peridynamics model at the atomistic scale compatible with an atomistic model needs to be comparatively finer than a peridynamics model at the macro-scale. Thus, it is important to introduce peridynamic models at different scales in order to mitigate the issue regarding computational cost. The coarse scale will consist of less number of particles than fine scale. A seamless coupling formulation among all these hierarchical models leads us to focus on an arbitrary region of interest at atomistic scale and establish a multiscale framework by exchanging information (such as average stress) between different models. Unlike concurrent coupling there is no interface domain in this hierarchical multiscale model. Thus this model can be named as “A Peridynamics based framework for hierarchical multiscale modeling” or PFHMM.

CHAPTER 3

FUNDAMENTALS OF MOLECULAR DYNAMICS SIMULATION

Molecular dynamics uses Newton's equations of motion to calculate the trajectory of atoms in any system. The advantage of MD simulation is its capability of updating a system in future time step based on the current state of the system. At each step, the forces on atoms are computed and combined with current position as velocity to update positions and velocities in next step. The primary equations of molecular dynamics simulation are:

$$m_i \ddot{r}_i = f_i \quad (1)$$

$$f_i = -\frac{\partial E(r_1, r_2, r_3 \dots r_N)}{\partial r_i} \quad (2)$$

Here,

m_i : Mass of i^{th} atom

r_i : Position of i^{th} atom

f_i : Force on i^{th} atom

$E(r_1, r_2, r_3 \dots r_N)$: Potential energy in N-atoms system

Molecular dynamics simulation consists of several important parts. Each part has its own importance as a building block of MD simulation scheme. These are discussed as follows:

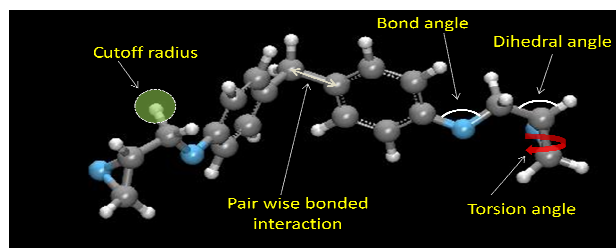


Figure 1. Different components of forcefield

3.1 Molecular interactions

Typically molecular interactions are divided into two major parts: Intramolecular and intermolecular interactions. In this work the *pcff* (polymer consistent force field) force field is used to specify the molecular interactions. The *pcff* force field is known to be appropriate for MD simulation of organic or inorganic polymeric systems. It consists of bonded energy terms, cross-terms and non-bonded energy terms. The bonded energy terms consist of bond stretch energy, (E_{bond}), angle bending energy (E_{angle}), dihedral angle rotation energy (E_{dihedral}) and out-of plane angle or improper energy (E_{Improper}). In addition, cross interaction energy ($E_{\text{cross-term}}$) come from dynamic vibrations among bond stretch, angle bending and dihedral rotation. The non-bonded energy terms refer to energy due to Columbic ($E_{\text{Coulombic}}$) and van-der-Walls (E_{vdW}) interactions. Columbic interaction was applied using Ewald summation technique. According to *pcff* force field, different components of potential energy can be written as [53]:

$$E(r_1, r_2, r_3 \dots r_N) = E_{\text{bond}} + E_{\text{angle}} + E_{\text{dihedral}} + E_{\text{improper}} + E_{\text{cross-terms}} + E_{\text{non-bonded}} \quad (3)$$

$E(r_1, r_2, r_3 \dots r_N)$: Total potential energy

E_{bond} : Bond energy

E_{angle} : Angle energy

E_{dihedral} : Dihedral energy

E_{improper} : Improper energy

The above equation represents all the components of *pcff* force field. Primarily bond, angle, dihedral and improper energy terms represent bonded interactions among atoms. In order to incorporate effect of atom vibration on the total potential energy of the system, the cross-terms are brought into the potential energy term. The cross-term consists of different energy components which originate from bond and angles between atoms. All these terms can be explicitly written in Equations (4.1-4.14):

$$E_{bond} = A_2 (r - r_0)^2 + A_3 (r - r_0)^3 + A_4 (r - r_0)^4 \quad (4.1)$$

$$E_{angle} = K_2 (\theta - \theta_0)^2 + K_3 (\theta - \theta_0)^3 + K_4 (\theta - \theta_0)^4 \quad (4.2)$$

$$E_{dihedral} = \sum_{n=1}^3 K'_n [1 - \cos(n\varphi - \varphi_n)] \quad (4.3)$$

$$E_{improper} = K \left[\frac{\chi_{ijkl} + \chi_{kjli} + \chi_{lyik} - \chi_0}{3} \right]^2 \quad (4.4)$$

$$E_{bb} = M (r_{ij} - r_1)(r_{jk} - r_2) \quad (4.5)$$

$$E_{ba} = [N_1 (r_{ij} - r_1) + N_2 (r_{jk} - r_2)](\theta - \theta_0) \quad (4.6)$$

$$E_{mbt} = (r_{jk} - r_2) [A'_1 \cos \varphi + A'_2 \cos 2\varphi + A'_3 \cos 3\varphi] \quad (4.7)$$

$$E_{ebt} = (r_{ij} - r_1) [B_1 \cos \varphi + B_2 \cos 2\varphi + B_3 \cos 3\varphi] + (r_{kl} - r_3) [C_1 \cos \varphi + C_2 \cos 2\varphi + C_3 \cos 3\varphi] \quad (4.8)$$

$$E_{at} = (\theta_{ijk} - \theta_1) [D_1 \cos \varphi + D_2 \cos 2\varphi + D_3 \cos 3\varphi] + (\theta_{jkl} - \theta_2) [E_1 \cos \varphi + E_2 \cos 2\varphi + E_3 \cos 3\varphi] \quad (4.9)$$

$$E_{aat} = M' (\theta_{ijk} - \theta_1)(\theta_{jkl} - \theta_2) \cos \varphi \quad (4.10)$$

$$E_{bb13} = N' (r_{ij} - r_1)(r_{kl} - r_3) \quad (4.11)$$

$$E_{aa} = M_1 (\theta_{ijk} - \theta_1)(\theta_{kjl} - \theta_3) + M_2 (\theta_{ijk} - \theta_1)(\theta_{ijl} - \theta_2) + M_3 (\theta_{ijl} - \theta_2)(\theta_{kjl} - \theta_3) \quad (4.12)$$

$$E_{Coulomb} = C \frac{q_1 q_2}{\epsilon r} \quad (4.13)$$

$$E_{vdW} = \sum_{ij} \epsilon \left[2 \left(\frac{\sigma}{r_{ij}} \right)^9 - 3 \left(\frac{\sigma}{r_{ij}} \right)^6 \right] \quad r < r_c \quad (4.14)$$

Where,

E_{bb} : Bond-bond energy

E_{ba} : Bond-angle energy

E_{mbt} : Middle-bond-torsion energy

E_{ebt} : End-bond-torsion energy

E_{at} : Angle-torsion energy

E_{aat} : Angle-angle-torsion energy

E_{bb13} : Bond-bond-13 energy

E_{aa} : Angle-angle energy

$E_{Coulomb}$: Coulombic energy

E_{vdW} : Energy due to Van der Waals interaction

Here, r_0 is the equilibrium bond length in pair wise configuration,

$A_i \left(\frac{\text{kcal/mole}}{\text{angstrom}^i} \right) : i = 2, 3, 4$ are the constants for pair wise bond configuration, θ is angle among

three atoms and θ_0 is the equilibrium angle (degrees) in angle configuration, K_2, K_3, K_4 are

constants with units $\left(\frac{\text{kcal/mole}}{\text{angstrom}^i} \right) : i = 2, 3, 4$, $\varphi_i : i = 1, 2, 3$ are dihedral angles in degree, K'_n

(kcal/mole) are the coefficients, χ_{ijkl}, χ_0 are out of plane quadruplet angles in degrees, K is

the constant with unit $\frac{\text{kcal/mole}}{\text{radian}^2}$. In the cross-terms, r_{ij}, r_{jk}, r_{kl} are the bond distances between

i, j, k, l -th atoms with units in angstroms. M is a constant (kcal/mole per square angstroms)

for bond-bond interaction in three atoms, N_1, N_2 are constants for bond-angle energy term in

kcal/mole per square angstroms, r_1, r_2, r_3 are the equilibrium bond lengths. The middle-bond-

torsion and end-bond-torsion terms consist of constants $A'_i, B'_i, C'_i : i = 1, 2, 3$ are with units in kcal

per angstrom. The constants $D_i, E_i : i = 1, 2, 3$ in angle-torsion energy are in $\frac{\text{kcal/mole}}{\text{radian}}$ and

θ_1, θ_2 in degree. The angle-angle-torsion energy contains $M' \left(\frac{\text{kcal/mole}}{\text{radian}^2} \right)$. The bond-bond13 term

contains $N' \left(\frac{\text{kcal/mole}}{\text{angstroms}^2} \right)$. The constants in angle-angle energy term $M_i : i = 1, 2, 3$ are with unit

$$\frac{\text{kcal/mole}}{\text{angstroms}}$$

The non-bonded energy term contains two terms: Columbic energy term due to electrostatic interaction Van der Waals interaction term defined by Lennard-Jones potential. In the Columbic energy C, ϵ are energy conversion constant and dielectric terms respectively. q_1, q_2 are charges at two locations apart from each other by distance r . The constants ϵ, σ are in Van der Waals energy are of units kcal/mole and angstroms respectively. r_c is cutoff distance (angstroms) which specifies the long-range non-bonded interaction radius of each atom.

3.2 Energy minimization

This part is quite vital in the MD simulation scheme. Initially the atoms needs to be moved iteratively to obtain the molecular configuration with minimum lowest energy $\min(E_{Total})$. Conjugate gradient (CG) algorithm [2] is applied in order to find out the global minima of the potential energy. In this algorithm, g_{k-1} is the gradient at r_{k-1} and g_k is the gradient at r_k . Using the gradient at r_k the global minima is traced in the new updated direction Z_k at k -the iteration. So, this is expressed according to CG algorithm as:

$$Z_k = -g_k + \gamma_k Z_{k-1} \quad (5.1)$$

$$\gamma_k = \frac{g_k \cdot g_k}{g_{k-1} \cdot g_{k-1}} \quad (5.2)$$

This algorithm is constrained under following conditions:

$$\mathbf{g}_i \cdot \mathbf{g}_j = 0 \quad (6.1)$$

$$\mathbf{Z}_i \cdot \frac{\partial^2 E(r_1, r_2, r_3 \dots r_N)}{\partial r_i \partial r_j} \cdot \mathbf{Z}_j = 0 \quad (6.2)$$

$$\mathbf{g}_i \cdot \mathbf{Z}_j = 0 \quad (6.3)$$

CG algorithm is dependent on timestep size, total number of iteration, energy and force tolerances. Prior to MD simulation of polymers it is essential to obtain a stable topology. Hence, it is very common to run energy minimization before MD simulation in any polymer based system.

3.3 Algorithms in MD simulation

MD simulation concerns about solving Newton's equations of motions for N-atoms system. At each timestep the total energy or Hamiltonian of the system is written as:

$$H = K(p_1, p_2, p_3 \dots p_N) + E(r_1, r_2, r_3 \dots r_N) \quad (7)$$

$$K(p_1, p_2, p_3 \dots p_N) = \sum_{i=1}^N \frac{|p_i|^2}{2m_i}$$

p_i : Momentum of i -th atom

m_i : Mass of i -th atom

Based on the total energy conservation criteria the equations of motion of the N-atoms system can be defined in terms of a system of ordinary differential equations:

$$\dot{r}_i - \frac{p_i}{m_i} = 0 \quad (8.1)$$

$$\dot{p}_i + \frac{\partial E(r_1, r_2, r_3 \dots r_N)}{\partial r_i} = 0 \quad (8.2)$$

Let's assume the above system of equations is obtained at time t . Finite difference method is used to update the current trajectory after solving the equations of motion. At the current state, acceleration of each atom $a_i(t) = \ddot{r}_i$ is calculated by combining the equations (8.1) and (8.2) and the written as:

$$m_i \ddot{r}_i + \frac{\partial E(r_1, r_2, r_3, \dots, r_N)}{\partial r_i} = 0 \quad (9)$$

This acceleration is combined with positions and velocities at time t to calculate the positions $r_i(t)$ and velocities $v_i(t)$ of the atoms at time $(t + \Delta t)$ and so on. This is commonly known as the “Time integration (TI) scheme” in MD simulation. There are several types of TI schemes available. Verlet algorithm is the most widely used among all the available methods. This algorithm uses the positions and accelerations at time $(t - \Delta t)$ to predict the position and velocities at time $(t + \Delta t)$. Positions at these two time steps are related by following equations:

$$r_i(t + \Delta t) = 2r_i(t) - r_i(t - \Delta t) + \Delta t^2 a_i(t) \quad (10)$$

The velocities are not calculated explicitly from Verlet algorithm. There is couple of simple ways to calculate new velocities:

$$v_i(t) = \frac{[r_i(t + \Delta t) - r_i(t - \Delta t)]}{2\Delta t} \quad (11.1)$$

$$v_i\left(t + \frac{1}{2}\Delta t\right) = \frac{[r_i(t + \Delta t) - r_i(t)]}{\Delta t} \quad (11.2)$$

The Verlet algorithm is simple, fast and memory efficient. So, Verlet algorithm is highly used in large systems. However, it has some disadvantages too. This algorithm is not renowned as a TI algorithm with high precision. It is evident that the higher order terms are discarded. The updated positions $r_i(t + \Delta t)$ are calculated by adding a very small quantity $\Delta t^2 a_i(t)$ to a comparatively large quantity $2r_i(t) - r_i(t - \Delta t)$. This may cause loss of precision. There is no explicit way to calculate $v_i(t)$. The algorithm is not a self starting. At $t = 0$ there is no straight forward way to obtain positions of atoms. So, this is done by truncating the Taylor’s expression of atom position:

$$r_i(-\Delta t) = r_i(0) - 2\Delta t v_i(0) \quad (12)$$

Hence, in order to overcome some drawbacks, the Verlet algorithm is modified to velocity-Verlet algorithm. The velocity-Verlet algorithm gives positions, velocities and accelerations simultaneously. So, the issue with precision is resolved. The positions are calculated at $(t + \Delta t)$ by using velocities and accelerations at t by using following equation:

$$r_i(t + \Delta t) = r_i(t) + \Delta t v_i(t) + \frac{1}{2} \Delta t^2 a_i(t) \quad (13)$$

The velocities at time $\left(t + \frac{1}{2} \Delta t\right)$ is calculated using the velocities and accelerations at time t :

$$v_i\left(t + \frac{1}{2} \Delta t\right) = v_i(t) + \frac{1}{2} \Delta t a_i(t) \quad (14)$$

Hence, using these velocities and positions the forces on each atom is computed at current positions. This gives $a_i(t + \Delta t)$. Finally, the velocities at $(t + \Delta t)$ are calculated using Equation (15).

$$v_i(t + \Delta t) = v_i(t) + \frac{1}{3} \Delta t a_i(t) + \frac{5}{6} \Delta t a_i(t) - \frac{1}{6} \Delta t a_i(t - \Delta t) \quad (15)$$

3.4 Ensemble average in MD simulation

As discussed earlier, the main objective of MD simulation is to replicate a material's structure at atomic scale and predict macroscopic properties without directly depending on experiments. A large system of atoms (approximately: 10^{23}) might represent a system which is equivalent to a typical model at macroscopic scale. Hence, any property Ω_{Average} of this large system can be calculated by averaging $\Omega[p_i(t), r_i(t)]$ for very long time $\tau = t \rightarrow \infty$:

$$\Omega_{\text{Average}} = \lim_{\tau \rightarrow \infty} \frac{1}{\tau} \int_{\tau=t=0}^{\tau} \Omega[p_i(t), r_i(t)] dt \quad (16)$$

$\Omega[p_i(t), r_i(t)]$: Functions of f_i

However, MD simulation of a large system for a long time is computationally unrealistic and expensive. Boltzman and Gibbs developed a solution to this problem. Based on statistical mechanics a single system evolving in time is replaced by large number of replications of that system. This is called “Ensemble”. According to “Ergodic hypothesis”, the time average Ω_{Average} of a quantity can be replaced by ensemble average $\langle \Omega \rangle$. There are different types of ensemble available. Among them NVE, NVT and NPT ensembles are widely used in MD simulations.

- Constant number of atoms, volume, energy (NVE)
- Constant number of atoms, temperature, volume (NVT)
- Constant number of atoms, temperature, pressure (NPT)

NVE is known as “microcanonical ensemble”. The pressure and temperature is not controlled during the simulation. The main objective is to conserve the energy. However, this might cause the pressure or temperature overshoot during time integration process. Typically, a system with higher stability is suitable for NVE. Thermodynamically systems following NVE ensemble are insulated from the surrounding environment.

NVT is known as “canonical ensemble”. The ensemble is obtained by controlling the temperature through direct temperature scaling during the initialization stage and by temperature-bath coupling during the data collection phase. Temperature controlled MD simulation is important in several types of systems. During the simulation, the temperature scaling is one way to control it. Thus, the velocities of atoms at timestep t are multiplied by a

factor, $\lambda = \sqrt{\frac{T_{\text{required}}}{T_{\text{current}}}}$ in order to scale the temperature of the system T_{current} to T_{required} . So, the

temperature change can be written in terms of scaled velocities:

$$|T_{\text{current}} - T_{\text{required}}| = \frac{1}{2} \sum_{i=1}^N \frac{2}{3} \frac{m_i (\lambda v_i)^2}{N k_B} - \frac{1}{2} \sum_{i=1}^N \frac{2}{3} \frac{m_i v_i^2}{N k_B} \quad (17)$$

k_B : Boltzman constant

λ : Scaling factor

The required temperature is maintained by coupling the system to a external heat bath at temperature, T_{required} . The heat bath acts as a heat source or sink by supplying or removing heat from the system. The velocities are scaled in such a way that the rate of change of temperature is proportional to the difference in temperature between heat bath and system. So, the scaling parameter, λ is written as:

$$\lambda^2 = 1 + \frac{\Delta t}{\tau_c} \left(\frac{T_{\text{bath}}}{T_{\text{current}}} - 1 \right) \quad (18)$$

τ_c : Coupling parameter

Both of these techniques are implemented in typical MD simulation programs. The coupling parameter, τ_c is highly dependent on the system. In NVT ensemble the volume is kept constant.

NPT (also ‘‘canonical ensemble’’) allows control over both the temperature and pressure. The volume is allowed to change, and the pressure is adjusted by compensating the volume. This is the ensemble of choice when the correct pressure, volume, and densities are important in the simulation. The volume fluctuation and pressure fluctuation in inversely related. Lets define the isothermal compressibility κ :

$$\kappa = -\frac{1}{V} \left(\frac{\partial V}{\partial P} \right)_T \quad (19)$$

During the NPT run, a *compressible* system has higher volume fluctuation and low pressure fluctuation compared to incompressible system. Hence, constant pressure simulation leads to change in unit cell dimension in order to achieve more stability.

Similar to NVT ensemble the pressure is controlled by both scaling the volume and using a pressure bath P_{bath} . The volume of the unit cell or simulation box scaled by λ which is analogous to scaling the atom positions by $\underline{\lambda}^{1/3}$. Mathematically these are expressed as:

$$\underline{\lambda} = 1 - \kappa \frac{\Delta t}{\tau_p} (P - P_{\text{bath}}) \quad (20)$$

τ_p : Relaxation constant

$$r_i^{\text{new}} = \underline{\lambda}^{1/3} r_i^{\text{old}}$$

The coupled parameter $\underline{\lambda}, \tau_p$ can be controlled isotropically (changing simulation box uniformly in all three directions) or anisotropically (change simulation box independently in any direction). In the entire work NVT, NVE and NPT ensembles were used for different models. Besides these another type of ensemble is “grand canonical” ensemble. In grand canonical ensemble number of atoms is not constant in the system. MD using this ensemble is not considered in the present work.

3.5 Boundary conditions

The role of boundary condition is very important in MD simulation. The boundary can be defined as a periodic or non-periodic boundary. Periodic boundary condition (PBC) eliminates the effect of free surface. It treats the system with small number of particles in such a way that the particles experience force as if they are in a bulk solution. This is very important while calculating mechanical properties. In periodic boundary conditions, the cubical simulation box is replicated throughout space to form an infinite lattice. In the course of the simulation, when a molecule moves in the central box, its periodic image in every one of the other boxes moves with

exactly the same orientation in exactly the same way. Thus, as a molecule leaves the central box, one of its images will enter through the opposite face. There are no walls at the boundary of the central unitcell, and the system has no surface. The central box simply forms a convenient coordinate system for measuring locations of the N molecules. This is shown in Figure 2.

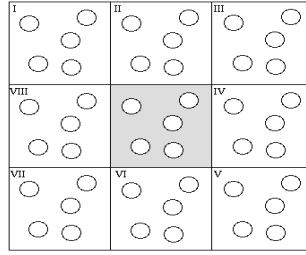


Figure 2. Schematic diagram of 2D periodic boundary condition

Unlike PBC, non-periodic boundary condition does not allow any replication of unitcell. It can be in all 3-directions or it can be in any specific direction. Non-periodic BC is important in evaluating thermal properties or interfacial properties. In this work both periodic and non-periodic BC were used depending upon the scope of simulation.

3.6 Atomistic stress calculation

The total energy in a system is based on contribution from both kinetic and potential energies. Hence the Hamiltonian based on this kinetic and potential part of total energy leads to calculate stress tensor σ_{ij}^{α} per α -th atom, (both tensile and compressive) is obtained from the following *virial* expression [54].

$$\sigma_{ij}^{\alpha} = -\frac{1}{Vol^{\alpha}} \left(m^{\alpha} v_i^{\alpha} v_j^{\beta} + \sum_{\substack{\beta \\ \beta \neq \alpha}} r_j^{\alpha\beta} f_i^{\alpha\beta} \right) \quad (21)$$

where, Vol^{α} is the volume of α -th atom. m^{α} is mass of α^{th} atom. $v_i^{\alpha}, v_j^{\alpha}$ are the velocities of α^{th} atom in i direction and α^{th} atom in j direction, respectively. $r_j^{\alpha\beta}$ is j -component of the pairwise

distance between α^{th} and β^{th} atoms. $f_i^{\alpha\beta}$ is i -component of the force between α^{th} and β^{th} atoms. It is difficult to obtain volume of each atom. Hence, from each α -th atom, LAMMPS gives $\sigma_{ij}^\alpha \cdot Vol^\alpha$ as an output. This quantity is summed over all the atoms and divided by the volume of the unitcell in order to obtain average stress in the unitcell.

3.7 Evaluation of elastic modulus using molecular mechanics (MM) method

The elastic constants of a polymer system can be determined by using several methods. In MM method, the elastic constants were determined from the changes in total potential energy subjected to uniaxial deformation of the structures ignoring the kinetic energy due to molecular motion. The amorphous cell model undergoes extension and compression in order to determine elastic properties. The entropic contribution to an elastic response can be neglected in polymeric glasses due to insignificant influence of the kinetic energy on the linear elastic regime of the stress-strain response [55]. As a result the first term with velocity components in Equation (21) is not considered in MM simulation. The first derivative of the potential energy with respect to strain provides internal stress tensor and the second derivative represents stiffness matrix. The unit cell (simulation box) undergoes unidirectional tensile and compressive deformations in all direction, $\boldsymbol{\varepsilon} = [\varepsilon_{11} \ \varepsilon_{22} \ \varepsilon_{33} \ \varepsilon_{44} \ \varepsilon_{55} \ \varepsilon_{66}]$. Thus, the corresponding stresses in the system (σ_i^+ and σ_i^-) are calculated using Equation (21). Hence, the stiffness components can be written in terms of stress components as [19, 55].

$$C_{ij} = \frac{\sigma_i^+ - \sigma_i^-}{2\Delta\varepsilon_j} \quad (22)$$

The deformation process is considered to be strain controlled. In Equation (21), σ_i is the i^{th} component of internal stress tensor and σ_i^+, σ_i^- correspond to stress component under tension

and compression. The change in strain components $\Delta\varepsilon_j$ is $2\varepsilon_j$ due to tensile and compressive deformation. The entire stiffness matrix can be calculated using Equation (22). Assuming ideal isotropic condition, Lamé's constants λ, μ were calculated using Equation (23). So, the Young's modulus and shear modulus of the system can be calculated using the following equations [55]:

$$\begin{aligned}
 E &= \mu \frac{3\lambda + 2\mu}{\lambda + \mu} && \text{Young's modulus} \\
 G &= \mu && \text{Shear modulus} \\
 \lambda &= \frac{1}{3}(C_{11} + C_{22} + C_{33}) - \frac{2}{3}(C_{44} + C_{55} + C_{66}) \\
 \mu &= \frac{1}{3}(C_{44} + C_{55} + C_{66})
 \end{aligned} \tag{23}$$

3.8 Stress-strain responses using MD method

Besides computing the elastic properties using MM method, it is also possible to obtain stress-strain relationship using MD simulation. The purpose is to perform numerical experiments with the unit cell by applying uniaxial deformation. In general, any uniaxial deformation causes atoms in the system to move along the applied strain. The stress can be represented as an average of all the principle stresses or “hydrostatic stress”. So, for any small applied strain ε , the average stress in the system is calculated using Equation (24). Each stress component is calculated from the virial stress expression in Equation (21) without ignoring the dynamic motion of the molecules

$$\bar{\sigma} = \frac{(\sigma_{11} + \sigma_{22} + \sigma_{33})}{3} \tag{24}$$

where, $\sigma_{11}, \sigma_{22}, \sigma_{33}$ virial stress in axial directions, $\bar{\sigma}$ is the hydrostatic stress. After every applied deformation the running averaged hydrostatic stress $\bar{\sigma}$ is calculated in order to smoothen the stress-strain response. The Young's modulus is also obtained from the slope of the linear regime of the stress-strain curve.

3.9 Interfacial Interactions

Molecular model calculates total potential energy $E(r_1, r_2, r_3 \dots r_N)$ of a N-atoms system. This leads to calculating force on each atom in the system. Similar to the previous discussion, it is possible to evaluate interaction between a polymer and nanostructure at atomic scale.

The interactions can be determined in couple of ways. One is by evaluating normal separation force F_{Cohesive} and another is by evaluating shear separation force F_{Pullout} . These forces are calculated from the change in interaction energy between the nanostructure and polymer system is given as follows:

$$E_{\text{Interaction}} = E_{\text{Total}} - (E_{\text{Polymer-without nanostructure}} + E_{\text{Nanostructure}}) \quad (25)$$

Here, E_{Total} is the total potential energy obtained from molecular simulation of combined polymer-nanostructure system. Once the nanofiller is moved away from the polymer matrix, it experiences reaction forces either F_{Cohesive} or F_{Pullout} based on the displacement of the nanofiller. The system is non-periodic along the direction of displacement in order to minimize the effect from surrounding neighborhood unit cells. Considering 2D geometry of graphene, the equations for calculating cohesive and pullout strength are written as:

$$\sigma_{\text{Cohesive}}^u = \frac{F_{\text{Cohesive}}}{L \times W} \quad (26.1)$$

$$\sigma_{\text{Pullout}}^u = \frac{F_{\text{Pullout}}}{l_c W} \quad (26.2)$$

L : Length of graphene

W : Width of graphene

l_c : Critical length at failure

CHAPTER 4

MODELING AND CHARACTERIZATION OF GRAPHENE-POLYMER NANOCOMPOSITES

In this chapter the main focus is to calculate mechanical properties of graphene-polymer nanocomposites. Two different types of polymers are considered. One is epoxy, synthetic polymer and another is cellulose, a bio-polymer. Epoxy has several structural applications whereas cellulose is getting popular day by day due to its bio-degradability. The common interest is enhancing the mechanical properties of both epoxy and cellulose based composite materials. Hence incorporating graphene as nanoreinforcing particle seems to have good prospect in further improving mechanical properties of epoxy and cellulose based materials. Along this direction, classical molecular dynamics simulation is used to determine the elastic properties of these two nanocomposites. The estimated results are compared with experimentally obtained data.

4.1 Molecular modeling and nano-characterization of graphene-epoxy nanocomposites

The primary focus of this section is on characterization of graphene-epoxy nanocomposites using molecular dynamics simulation. The elastic and interfacial properties are calculated using molecular dynamics (MD) simulation. Both amorphous and stacked graphene models were considered in order to evaluate effect of graphene's weight concentration, aspect ratio and dispersion on elastic properties. Eventually, the Young's modulus calculated from MD simulation was verified with nanoindentation test results.

4.1.1 Amorphous graphene-epoxy model

The molecular model of amorphous crosslinked graphene-epoxy (G-Ep) nanocomposite system is developed in order to study the effects of graphene concentrations and aspect ratios on mechanical properties such as stress-strain responses, Young's modulus and shear modulus. The model is also implied in investigating some important structural parameters such as radial distribution function (RDF), atomic density, and molecular energy pertinent to G-Ep system. A typical amorphous cross-linked epoxy unit cell contains epoxy and curing agent in the ratio of 12:4 [5]. During cross-linking process, reactive sites from EPON 862 (epoxide groups) create new bonds with reactive sites from TETA (nitrogen groups: NH, NH_2). If they come close enough to each other within range of $4\text{\AA}^0 - 10\text{\AA}^0$ [56], the cross-linking occurs. This is schematically shown in the left side of Figure. 3. Cross-linking process between EPON 862 and TETA is non-trivial. The computational cost becomes higher as the number of EPON 862 and TETA molecules increases. Hence, Yu and coauthors proposed to use a *representative cross-linked epoxy unit* composed of three EPON 862 molecules and one TETA molecule with cross-link ratio of 0.5 [56]. In this representative unit, three reactive sites of TETA are connected to three EPON molecules. Each unit consists of 157 atoms. Yu and coauthors concluded that, the mechanical properties of cross-linked epoxy comprising of this representative epoxy unit showed reasonable agreement with experimental observations as well as the cross-linked epoxy system obtained from MD simulation. So, keeping the similar idea in mind, this representative cross-linked unit was used in the current work as well. As a result, the dynamics cross-linking approach was not considered. Instead, an initial single representative molecule was constructed and the inter-molecular and intra-molecular interaction energy components (such as bond, angle,

dihedral etc) were assigned based on pcff forcefield [53]. Afterwards, amorphous unitcells were generated by replicating this representative epoxy molecule in multiple number of times along with graphene sheets.

Graphene sheet is a 2D nano structure consists of carbon atoms bonded by sp^2 hybridized electrons as shown in Figure. 3. The carbon atoms are arranged in a hexagonal pattern with the shortest distance of 1.42 \AA between atoms with bond angle 120° . Single layer graphene possesses very high mechanical properties. The average Young's modulus of single layer zigzag graphene sheet with length 20.18 nm and width 4.18 nm is 1.033 TPa [57]. In this study graphene sheets with two different sizes were considered. These were defined in terms of aspect ratios AR-LW or AR-LT. AR-LW is length to width ratio and AR-LT is length to thickness ratio. Based on aspect ratio, the graphene sheets are named as Type-a ($AR-LW \geq 5.0$, $AR-LT \geq 150$) and Type-b ($AR-LW \geq 10.0$ and $AR-LT \geq 480$). The graphene sheets with hydrogen terminated edges were embedded in 3D periodic amorphous unit cells for evaluating elastic properties.

In this study 1%, 3% and 5% of graphene by weight was considered in the cubic amorphous unit cells. The initial density of amorphous graphene-epoxy unit cells was kept in the range of 0.7-1.0 gm/cc. Based on this initial density, the dimension of each unitcell was estimated. The number of epoxy monomers was determined in such a way that it ensures expected weight percentage of graphene in the unit cell. Each unitcell consists of a single graphene and randomly positioned multiple number of representative epoxy molecules based on the weight concentration of graphene. It is possible to obtain predetermined weight percentage of graphene in the unitcell by changing the number of cross-linked epoxy molecules while keeping the number of graphene sheet to one. Final configuration of each unitcell was obtained by equilibrating the model using MD. Table 1 shows unitcell configurations with relevant graphene

aspect ratios and weight percentages. Figure 3 schematically describes the development of graphene-epoxy amorphous unitcells.

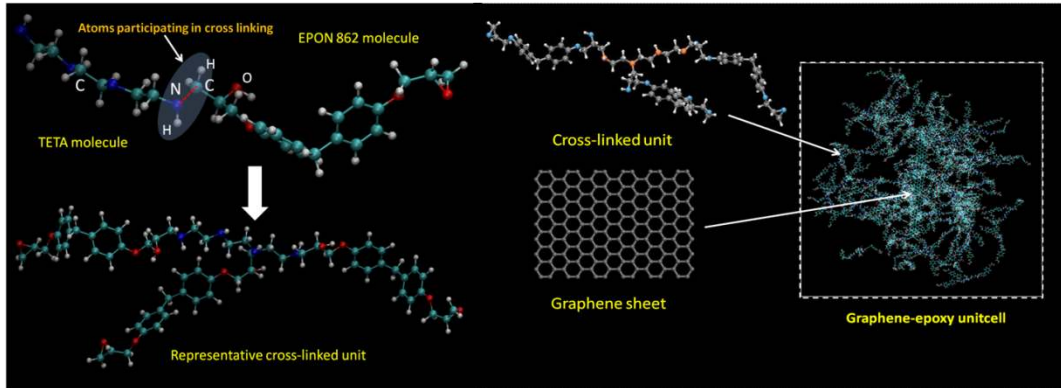


Figure 3. Schematic diagram of developing amorphous model for graphene-epoxy

Material Configuration	Aspect ratio (AR)	Weight percentage of graphene	Number of graphenes	Cubic Unit cell length : a (Å)	Number of representative epoxy molecules
G-Ep-Nc-I	AR-LW \geq 5, AR-LT \geq 150 (Type-a)	1%	1	65	70
G-Ep-Nc-II	AR-LW \geq 10, AR-LT \geq 480 (Type-b)	1%	1	90	280
G-Ep-Nc-III	AR-LW \geq 5, AR-LT \geq 150 (Type-a)	3%	1	38.8	22
G-Ep-Nc-IV	AR-LW \geq 10, AR-LT \geq 480 (Type-b)	3%	1	62	90
G-Ep-Nc-V	AR-LW \geq 5, AR-LT \geq 150 (Type-a)	5%	1	33	13
G-Ep-Nc-VI	AR-LW \geq 10, AR-LT \geq 480 (Type-b)	5%	1	52.3	53

Table 1. Material configurations of G-Ep amorphous system

4.1.2 Stacked graphene-epoxy model

The effects of single, dispersed and agglomerated graphene layers on stress-strain responses and Young's modulus were studied using stacked graphene model (SGM). The SGM of graphene-epoxy nanocomposite consisting of single graphene, dispersed and agglomerated layered graphenes were developed as shown in Figure 4. The unit cell configurations of three

stacked graphene models are listed in Table 2. Each unitcell consists of less than 3% graphene with symmetry P3m [58]. Average spacing between graphene and epoxy matrix is seen to be approximately 2\AA . The fundamental difference between amorphous and stacked graphene models is the local periodicity of graphene platelets.

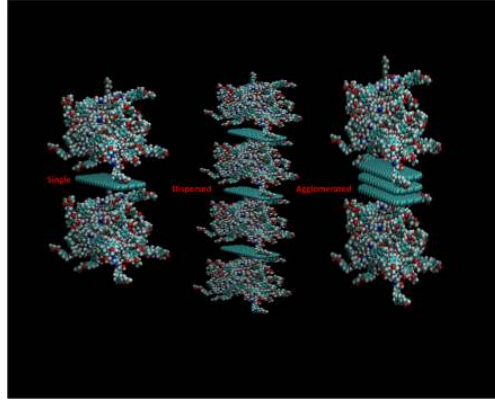


Figure 4. Schematic diagram of stacked graphene model (SGM)

Configuration	Unit cell dimension (\AA^0)	Number of graphene plates	Number of representative epoxy molecules
SGM-G-Ep-I	a=9.84, b=19.02, c=1056.42	1	46
SGM-G-Ep-II	a=9.84, b=19.02, c=2116.24	3 (Dispersed)	68
SGM-G-Ep-III	a=9.84, b=19.02, c=3104.21	3 (Agglomerated)	68

Table 2. Material configurations of stacked G-Ep system

4.1.3 Interface model

Molecular model calculates total potential energy of a system with N number of atoms system. This leads to calculating force on each atom as force is negative of gradient of the energy. It is possible to evaluate interaction between a polymer and nanostructure at atomic scale. The interactions can be determined in many ways. One is by evaluating normal separation force F_{Cohesive} and another is by evaluating shear separation force F_{Pullout} . These forces are

calculated from the change in interaction energy between the nanostructure and polymer system. Once the nanofiller is moved away from the polymer matrix, it experiences reaction forces either F_{Cohesive} or F_{Pullout} based on the direction of nanofiller movement. The system is non-periodic along the direction of displacement [2]. The interface models shown in Figure 5 were developed in order to study the load transfer mechanism between graphene and epoxy matrix. Graphenes with two different lengths (39.36 \AA^0 and 118.08 \AA^0) were considered in order to evaluate the effect of aspect ratio. Both normal (mode-I) and shear separations (mode-II) were considered. For normal mode separation, epoxy molecules reside above a single graphene sheet whereas in shear separation, epoxy molecules reside on both side of the graphene sheet. Graphene is free to move in z-direction and x-direction for normal and shear separations respectively. Details about unit cell configurations are provided in Table 3.

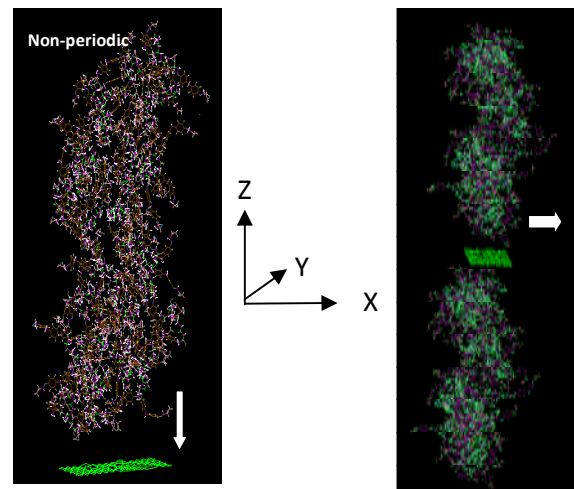


Figure 5. Mode-I and Mode-II interface model of G-Ep system

Configuration	Graphene sheet dimension (length x width) (\AA^2)	Aspect ratio	Number of carbon atoms in graphene	Interaction force type
Mode-I-a	39.36 x 19.02	AR-LW \geq 2.06, AR-LT \geq 25.5	248	Normal
Mode-I-b	118.08 x 19.02	AR-LW \geq 6.20, AR-LT \geq 76.67	766	Normal
Mode-II-a	39.36 x 19.02	AR-LW \geq 2.06, AR-LT \geq 25.5	248	Shear
Mode-II-b	118.08 x 19.02	AR-LW \geq 6.20, AR-LT \geq 76.67	766	Shear

Table 3. Unit cell configuration for interface model

4.1.4 Computational details

MD equilibration was done prior to calculating mechanical properties. In this work three different categories such as amorphous, stacked graphene and interface models were considered. The following sections describe MD simulation scheme that was considered in each category. All the calculations were done using the open source molecular dynamics code LAMMPS developed in Sandia National Laboratory [59].

4.1.4.1 Amorphous models

The initial stable configuration was obtained by minimizing the energy of each system by conjugate gradient method [2]. The average cutoff range for non-bonded interaction was 8 \AA . All systems with type-a were subject to molecular dynamic equilibration under NVT (constant number of atoms, temperature and volume) condition with Nose-Hoover thermostat for 10000 steps followed by NPT ensemble (constant number of atoms, pressure and temperature) for 5000 thousand steps at 300 K temperature and 0.0 atm external pressure. The amorphous models with type-b graphene were equilibrated under NVT for 30000 steps at 300K and NPT for 10000 steps at 300K temperature and 0.0 atm external pressure. Timestep size was 0.5-1.0 fs. Nose-Hoover

barostat was used to add damping in the system [2]. Once the system is equilibrated, it underwent uniaxial deformation. Verlet time integration scheme was used throughout the whole simulation. At this stage, the amorphous systems were subjected to either uniaxial deformation in order to obtain stress-strain response using MD or series of deformations in all directions using MM in order to calculate Young's modulus and shear modulus. Within 1500 steps, the unitcells were subjected to 0.0001 unidirectional strain at every 300 step under NVT ensemble at 0.1K. The effect thermal noise on stress-strain response was avoided by keeping the temperature at 0.1K. The contribution of kinetic energy is not significantly important while evaluating the linear elastic regime of the stress-strain response. After applying strains at each step, the running averaged stress throughout the unitcell was calculated. Timestep size was 0.7-1.0 fs during deformation.

Molecular mechanics (MM) based deformation method requires a series of deformations in xx-yy-zz-xy-yz-xz directions. The equilibrated unitcells were subjected to $\pm 10^{-6}$ % strain in all the directions. After each deformation spatially averaged stress throughout the system was calculated. The stiffness matrix components were calculated using Equation (22).

Figure 6 shows typical energy, temperature and pressure profiles with respect to time during MD equilibration process. These data were collected from the system "G-Ep-Nc-IV" during NVT and NPT based equilibration. The objective of studying these parameters is to ensure that the systems are properly equilibrated prior to applying deformation. Temperature and total energy profiles are obtained during NVT runs. It is noticed that, after 1500 fs the energy as well as temperature become very stable. The temperature is expected to converge approximately at 300K as the temperature of the heat bath is 300K. And the energy converges to 4.0×10^4 Kcal/mole for this specific system. This confirms that the system was properly equilibrated

during NVT runs. According to the third plot in Figure 6, the pressure in this system was observed to be stable around 0.0 atm during NPT runs.

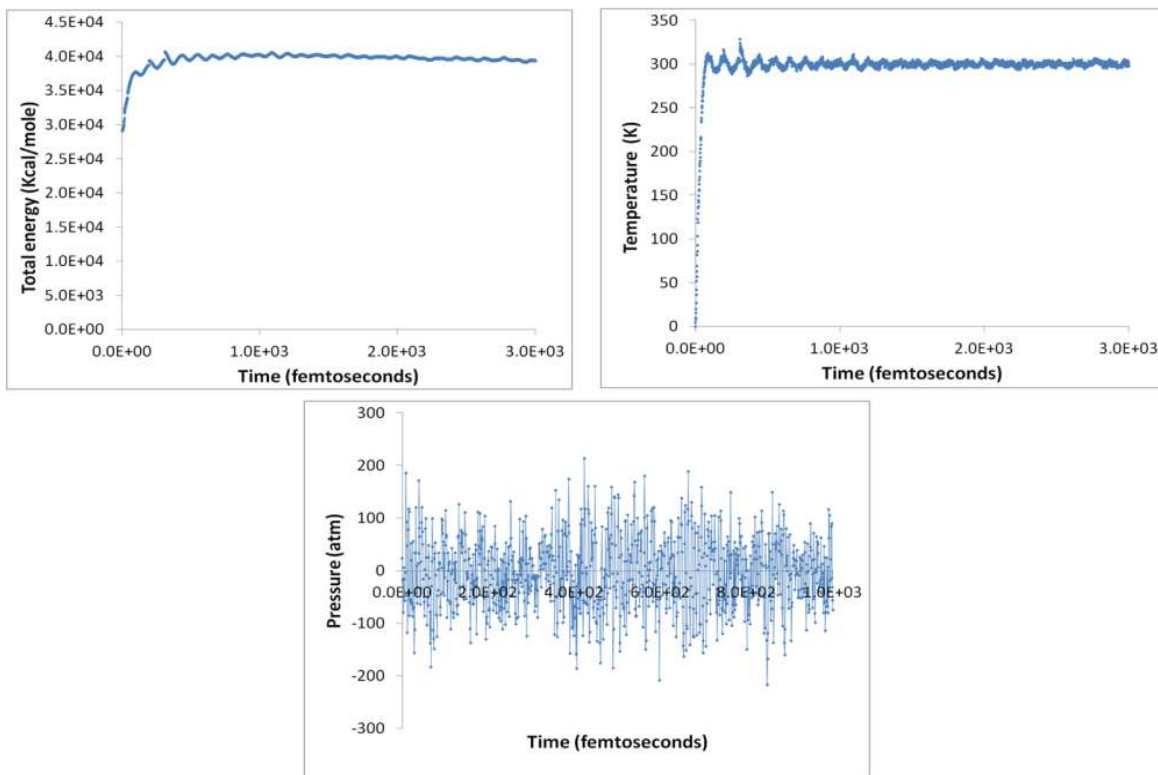


Figure 6. Typical temperature, total energy and pressure plots at different times

4.1.4.2 Stacked graphene model

In the stacked graphene models, the energy was minimized using conjugate gradient method followed by NVT based MD runs for 5000 steps at 300K. Timestep size was 0.8-1.0 fs and the cutoff distance was 8 \AA . The positions and velocities of the atoms were updated using verlet time integration scheme. Once the system is equilibrated, it was subjected to deform in xx-yy-zz directions. Within 1000 steps, each unit cell was deformed at every 100 steps under NVT at 0.1K. Strain varied within the range of $10^{-2}\%$ - $10^{-7}\%$. Nose-Hoover thermostat was used. The atoms in the systems were also subjected to Langevin dynamics [2] with a damping term of 100

fs. After each deformation, the running averaged stress was calculated using Equation (21) to obtain stress-strain response.

4.1.4.3 Interface models

Both normal and shear separation forces were calculated on a slowly displaced graphene sheet in normal and shear directions as shown in Figure 3. Such displacements lead to mode-I and mode-II separation. Initially, the space between epoxy and graphene sheet was maintained approximately $2A^0$. The cutoff distance was $20 A^0$. For mode-I case, the graphene-epoxy unit cell is non-periodic in z-axis. Similarly, for mode-II case the system was nonperiodic in xy plane. The reaction forces on graphene due to mode-I or mode-II separation were calculated. This leads us to obtain forces vs. displacement curve for both mode-I and mode-II cases. The weight percentage of graphene was maintained higher than 3% in order to emphasize the effect of graphene on van der Waals interaction between epoxy and graphene. Prior to transverse or longitudinal movements of graphene plate, energy was minimized in all the systems using conjugate gradient method. Energy and force tolerance were quantified in the order of 10^{-10} . After the minimization, each system was equilibrated under NVT for 5000 steps with step size 1.0 fs. Once the systems are equilibrated, graphene was moved away from the polymer matrix by average translation rate of $0.01 A^0/\text{fs}$ for 0.5 – 3.0 ps in transverse direction (pullout) and $0.001\text{-}0.0001 A^0/\text{fs}$ for 1.5 ps in longitudinal direction (cohesive). The positions and velocities of the atoms were updated using verlet time integration scheme.

4.1.5 Nanoindentation tests

4.1.5.1 Nanoindentation test procedure

The experimental characterization was done for graphene-epoxy systems using nanoindentation method. EPON 862 and EPIKURE 3234 curing agent were used with graphene

nanopowders with average thickness of 8 nm (20-30 graphene layers). The graphene/epoxy nanocomposites were prepared with 1%, 3% and 5% weight percentage of graphene. The graphene and epoxy mixture was sonicated for an hour using VXC 750 tip sonicator followed by adding curing agent. Epoxy/curing agent was kept in the weight ratio of 100:14.5. The mixture was stirred using a magnetic mixer for 5 minutes and poured onto a 5x5 in glass mold which was sprayed with frekote. Besides graphene-epoxy samples one additional sample was prepared with neat epoxy. These samples were cured for 24 hours at room temperature and post cured at 100⁰C for an hour. From these prepared panels, coupon test specimens for macroscopic property measurement were obtained with dimension: 4 in x 0.33 in x 0.036 in (LxWxt). The gauge length was 2 inch. These samples were used to perform tensile test using MTS electromechanical testing equipment. From the same composite panel, specimens for nanoindentation test were also prepared using diamond cutter. The dimension of nanoindentation test samples were of dimension: 0.5 in x 0.33 in x 0.036 in. Based on graphene weight concentration, the specimens were named as ExpGEp-1%, ExpGEp-3%, ExpGEp-5% and ExpEpon for specimens with 1%, 3%, 5% graphenes and neat epoxy, respectively. The top surface of the specimens (along thickness direction) were cleaned with acetone and polished with fine sand paper in order to obtain appropriate surface for indentation test. This was done iteratively until the surface roughness was reduced. The scanning electron microscope (SEM) image of the sample surfaces is shown in Figure. 7. JEOL 7000 SEM microscope was used. The surfaces of the graphene-epoxy samples were looked at carefully in order to locate graphenes in the epoxy matrix. The most likely spotted graphenes are encircled in Figure 7b-7d.

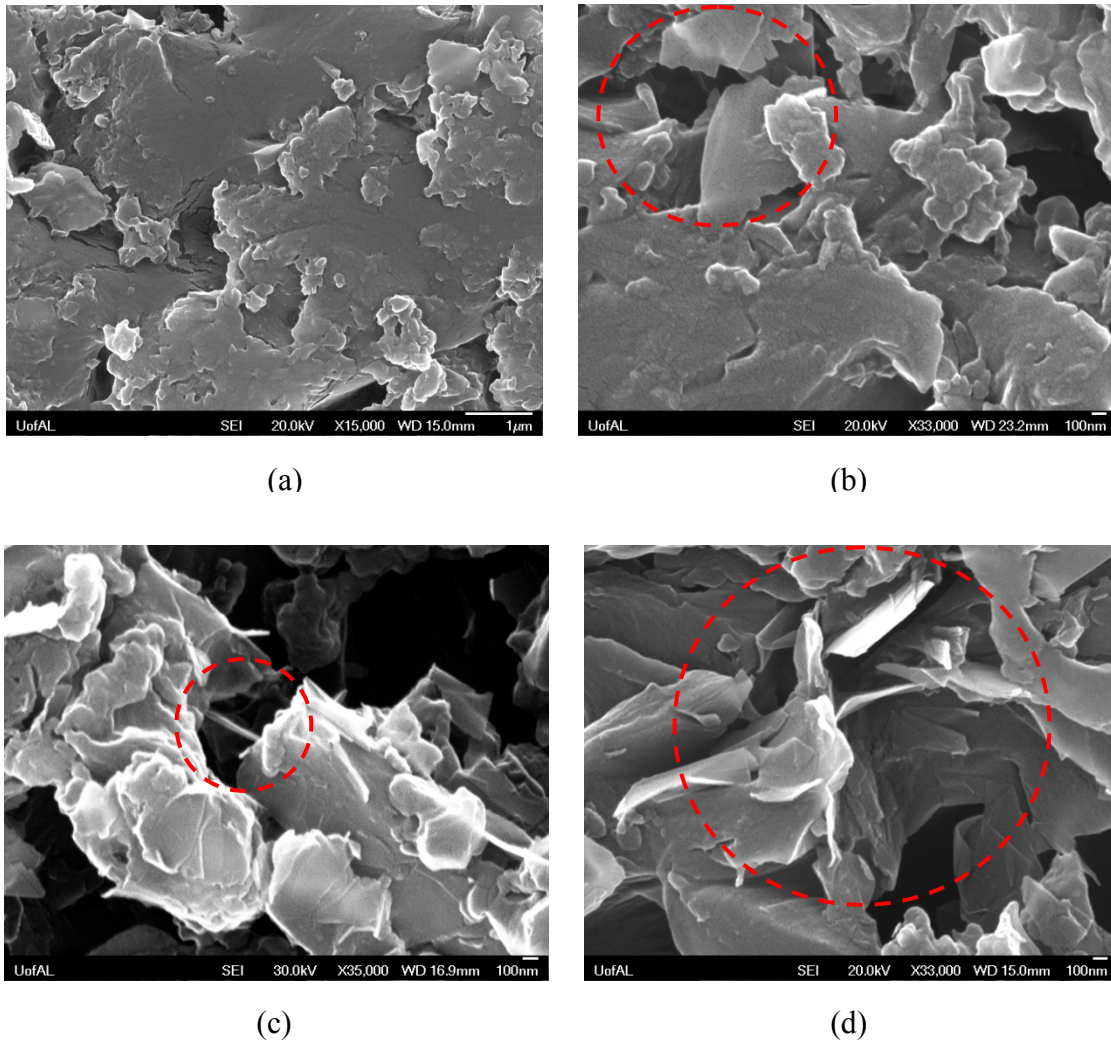


Figure 7. SEM image of the sectional surface of (a) ExpEpon (b) ExpGEP-1%
(c) ExpGEP-3% (d) ExpGEP-5%

Afterwards nanoindentation tests were carried out using Hysitron TI 900 Triboindenter. Prior to conducting the actual nanoindentation tests with graphene-epoxy samples, the T1 900 Triboindenter had to be calibrated using standard calibration procedure. There are three calibration steps. Firstly, “air indent calibration” was conducted in order to consider the weights of the tip and piezoelectric indenter head. Secondly, “optical calibration” was done on the Aluminum sample in order to adjust the tip positioning. Finally, “probe calibration” was carried

out on Quartz sample with the current tip in order to obtain the standard load vs. displacement curve fitting parameters. The whole calibration process took approximately 6-7 hours. Once the nanoindenter is calibrated appropriately, the actual nanoindentation tests were started. Berkovich nanoindentation tip with 100 nm radius of curvature and angle of 142.3° was used throughout the testing. The nanoindentation test was carried out at sixteen different locations on the graphene-epoxy specimen surface separated by 10 micron distance. For neat epoxy specimen, this was done at nine locations separated by 10 micron distance. All the nanoindentation tests were quasi-static. The loading profile had three segments: loading, hold and unloading. The average total length of time interval was 13 s. Within this interval, first 5s is loading regime where load starts from $0 \mu\text{N}$ to $5000 \mu\text{N}$. After that, the hold regime lasted from 5s to 8s followed by unload regime. During unloading process load decreased from $5000 \mu\text{N}$ to $0 \mu\text{N}$ between 8s to 13s. The hold regime leads to avoid creep during unloading regime. Eventually, elastic modulus was calculated from the slope of unloading curve. The schematic diagram of nanoindentation and the loading/unloading curve is shown in Figure. 8

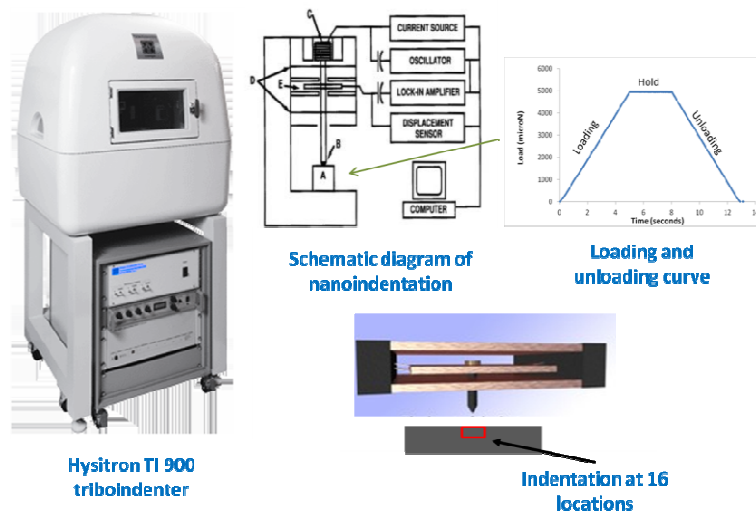


Figure 8. Schematic diagram of nanoindentation method

4.1.5.2 Nanoindentation test results

Figure 9 shows the representative load vs. displacement curves for graphene-epoxy specimens with different weight percentages of graphene and neat epoxy samples. For ExpGEp-1%, the indentation depth is significantly lower than the other two cases. There was no jump or local discontinuity observed. This indicates that no cracks were initiated during the loading process. The maximum indentation depth during load holding regime was 2190.94 nm for specimen with 5% graphenes and minimum depth was 1181.92 nm from 1% graphene based specimen. The slope of load-displacement curve during unloading is the highest for ExpGEp-1% and lowest for ExpGEp-5%. ExpGEp-3% and ExpEpon reside in between. The elastic modulus is calculated by fitting the unloading curve with a power relation. This is related to the first part of the unloading curve. Thus, the reduced elastic moduli obtained from nanoindentation tests for ExpGEp-1%, ExpGEp-3%, ExpGEp-5% and ExpEpon are 5.35 ± 1.37 GPa, 5.08 ± 1.71 GPa, 4.43 ± 1.03 GPa and 4.58 ± 1.47 GPa respectively. This is clearly noticed that incorporating 1% and 3% graphene certainly enhances the elastic property of neat epoxy based systems. Besides elastic modulus, hardness is also function of indentation depth. The hardness H is calculated as:

$$H = \frac{P_{\max}}{A}, \text{ where } P_{\max} \text{ and } A \text{ are the maximum load and projected indentation area respectively.}$$

The projected indentation area depends on the geometry of the indenter and is a function of indentation displacement. The effect of graphene weight percentage influences the hardness as well. The maximum hardness H_{\max} among each sixteen locations is seen to be decreasing with weight concentration of graphene. For ExpGEp-1%, ExpGEp-3%, ExpGEp-5% and ExpEpon, the values of H_{\max} were 0.392 GPa, 0.295 GPa, 0.280 Gpa, and 0.3 GPa respectively. So, it is evident that 1% graphene improves the hardness of graphene-epoxy nanocomposites. From this perspective, 3% and 5% graphene based specimens possess hardness which is more comparable

with neat epoxy resin. The tensile test of the same specimens showed Young's modulus value approximately 2.17 GPa, 2.50 GPa, 2.07 GPa and 2.12 GPa for ExpGEP-1%, ExpGEP-3%, ExpGEP-5% and ExpEpon, respectively. While comparing nanoindentation and coupon test data, it is observed that the Young's moduli from coupon test relatively lower than nanoindentation test data.

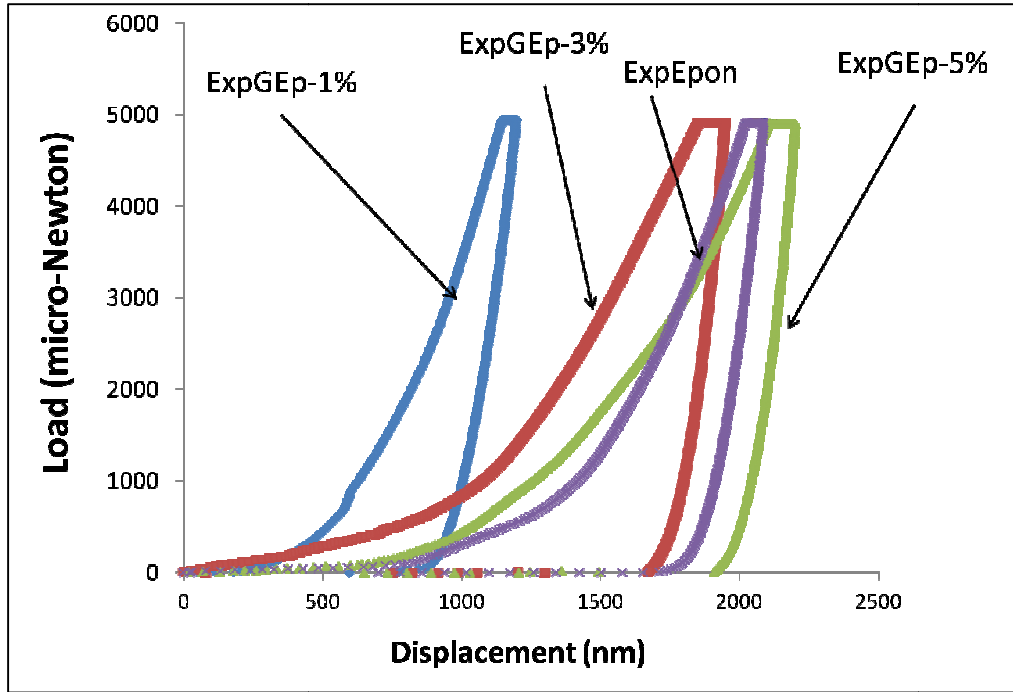


Figure 9. Load vs displacement curves during nanoindentation

4.1.6 Results and discussion from molecular modeling

The first part of this section focuses on analyzing radial distribution function (RDF), atom density and evolution in molecular energy of different G-Ep systems. This is important in understanding the characteristics of simulated molecular models. Later the effects of graphene aspect ratio, weight percentage and dispersion on elastic modulus of G-Ep nanocomposites are discussed. The interfacial properties such as cohesive force and pull out forces of G-Ep system

are analyzed. Finally, the results obtained from this study are compared with the same determined using micromechanics model, nanoindentation test and coupon test data.

4.1.6.1 Radial distribution function (RDF)

In general, RDF $g(r)$ is a correlation function which relates the pairwise particle (atoms, molecules) density in a system to the distance from a reference point. As a result RDF provides information about the distribution pattern of particles such as graphene atoms and epoxy molecule in G-Ep system. Figure 10 shows RDF of any pair of atoms in G-Ep system. The absence of any noticeable sharp peaks in the RDF ensures the amorphous nature of the graphene-epoxy system. The highest peak is observed at 3.9 \AA^0 which indicates maximum concentration of atoms in the entire system at this pairwise distance. The influence of graphene concentration is seen to be insignificant on RDF for type-a sample. But highest and lowest values of $g(r)$ are seen in type-b G-Ep system with 1% and 5% graphene concentrations, respectively. G-Ep systems lose any possibility of local order beyond pairwise distance of 6 \AA^0 .

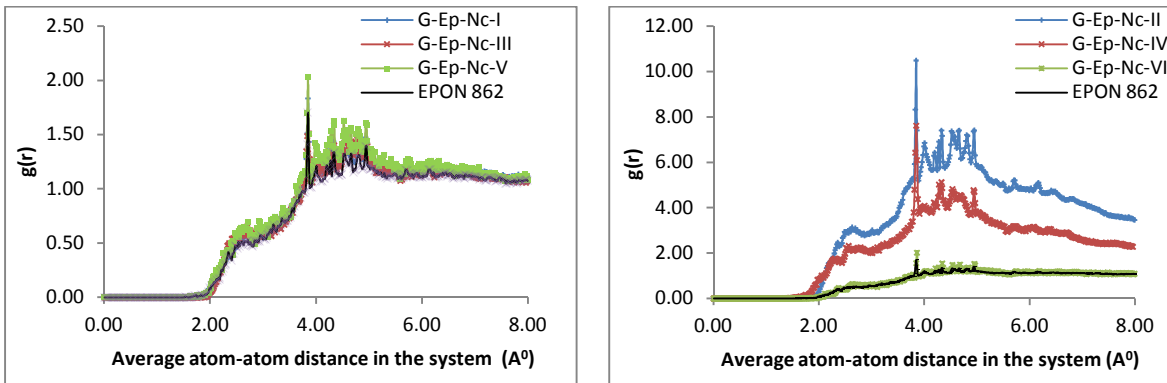


Figure 10. RDF of any pair of atoms in graphene-epoxy amorphous system (Left: AR-LT 150 and Right: AR-LT 480)

4.1.6.2 Atom density

In molecular modeling atom density in the unit cell plays an important role in affecting mechanical properties. In all these unit cells, number of epoxy molecules was changed in order

to obtain necessary weight percentage of graphene. Thus, atom density in a unit cell is changed with respect to different weight percentage. Figure. 11 shows atom densities as a function of graphene concentrations in the unit cell for both type-a and type-b nanocomposites. The atom density in type-b G-Ep nanocomposites is significantly low for 3% and 5% graphene systems and corresponding Young's modulus is also seen to be significantly low as shown in Table 4. Highest atom density is observed in unit cells with 1% graphene content which also shows comparatively highest Young's and shear modulus. The RDF for type-b graphene system in Figure. 10 showed comparatively weaker pairwise correlation in the G-Ep systems with 5% graphene. This is possibly due to lower atom density in G-Ep-Nc-IV and G-Ep-Nc-V unitcells.

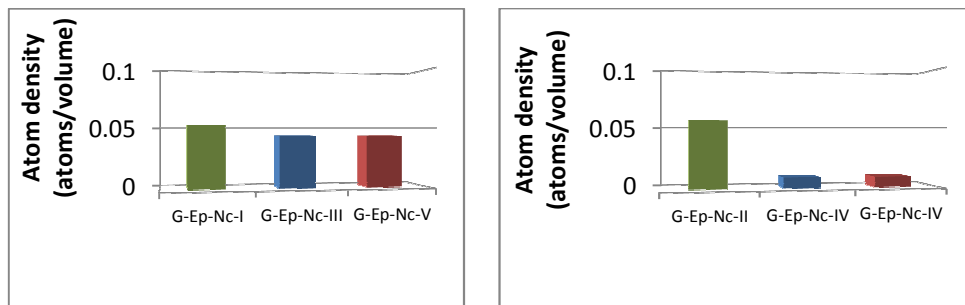


Figure 11. Atom densities in different graphene-epoxy unitcells

4.1.6.3 Molecular energy

The applied strain causes change in atom positions, velocities and overall molecular structure resulting an increase in overall potential energy. In general, potential energy consists of molecular energy ($E_{mol} = E_{Bond} + E_{Angle} + E_{Dihedral} + E_{Improper} + E_{Cross-terms}$) and van der Waals energy. The potential energy has comparatively larger contribution in total molecular energy than van der Waals energy. The change in molecular energy followed by applied deformation indicates the sensitivity of the molecules against applied strain. Figure. 12 shows molecular energy verses strain plots for G-Ep nanocomposites with graphene concentration 1%, 3% and 5% for both type-a and type-b graphenes. The increase in slope of molecular energy clearly explains the

deformation in the molecular topology with applied strain. The molecular energy plot is seen to be comparatively steeper and higher for G-Ep with 1% graphene which provided higher modulus. But the change in molecular energy is observed to be very small in G-Ep with 5% graphene showing comparatively lower modulus. It is to be noted that the amount of molecular energy is also seen to be higher with increased aspect ratio as seen in Figure. 12.

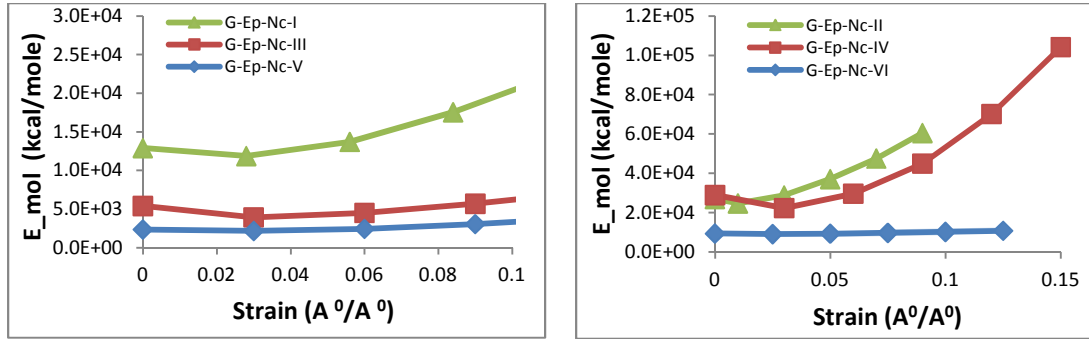


Figure 12. Molecular energy in amorphous systems with type-a and type-b graphenes

4.1.6.4 Effects of graphene concentrations and aspect ratio on elastic constants

The MD simulated stress-strain responses of G-Ep nanocomposites with graphene concentrations (1%, 3% and 5%) and aspect ratios (AR-LT: 150, 480) are plotted in Figure 13. The values of Young's modulus (E) were determined from the slope of individual curve. The fluctuations in the stress-strain responses are minimized applying moving average technique. In MM method, Young's modulus, E and shear modulus G , were calculated from Lamé's constants λ , μ defined by Equation (23). In Table 4, Young's modulus E and shear modulus G of G-Ep nanocomposites calculated by molecular mechanics (MM) and molecular dynamic (MD) methods are provided. The MM and MD simulation results are then compared with the data generated by Mori-Tanaka micromechanics (MTM) model [21]. The effects of graphene weight concentrations and aspect ratios on Young's modulus and shear modulus of G-Ep

nanocomposites are shown in Table 4. Finally, these data are compared with neat epoxy resin. In Table 4, Young's modulus and shear modulus of neat epoxy resin (EPON 862) are seen to be 2.5 GPa and 0.95 GPa, respectively by MM simulation. But the MD simulation shows Young's modulus of neat epoxy resin equals to 3.42 GPa. From literature, the calculated Young's modulus and shear modulus of neat epoxy are 3.362 GPa and 1.22 GPa respectively [56]. The Young's modulus and shear modulus data of G-Ep nanocomposites predicted using MM, MD and MTM simulations are seen to be comparatively higher than those of neat epoxy resin. The Young's moduli for different G-Ep systems are seen to be in the range 1.34-4.56 GPa by MM and 1.77-5.0 GPa by MD simulations. It is observed that Young's modulus predicted by MD is comparatively higher than the same predicted by MM method. This trend is seen for both type-a and type-b samples. These variations are reasonable since the energy associated with atom's linear momentum is not incorporated in MM simulation. It is seen that modulus of nanocomposites with lower graphene concentration (1% by weight) is comparatively higher than the same with higher concentration (5% by weight). This is possibly due to the variation in atom density. The results show comparatively higher E value with decreased aspect ratio in comparison to increased aspect ratio. In Table 4, shear modulus, G is observed to be in the range of 0.45-1.73 GPa for G-Ep nanocomposites (type-a) in comparison to 0.95 GPa for neat epoxy resin. The results of this study show highest G (1.37 GPa) with lowest graphene concentration (1%) and lowest aspect ratio (150). The Young's modulus calculated using Mori Tanaka micromechanics (MTM) model show comparatively lower values in G-Ep system with 1% and 3% by weight concentration of graphene compared to MD simulation data [21]. These represent the scaling effects between MD and MTM methods. It is to be noted that the Young's modulus calculated by MTM method shows higher values with increased graphene concentrations but in

MD simulation the similar trend is not observed. It is to be noted that the micromechanics model assumes the unit cell to be homogeneous. It is to be mentioned that increased concentration also enhance possibility of agglomeration in the system. Hence, the prediction shows a monotonically increasing nature in Young's modulus with the increasing volume fraction of nanofiller. But in atomistic models, spatially distribution of atoms, atom density and change in molecular energy etc. in the system play an important rule. Hence, monotonically increasing Young's modulus with respect to weight percentage of graphenes may not be realistic in actual scenario. Work by Rafiee [22] showed initially increase and eventually decrease in the Young's modulus of graphene-epoxy nanocomposites as the weight percentage of graphene increases. They considered graphene sheet with length to width aspect ratio of 19 (approximately).

The elastic modulus calculated from MD simulation exhibits similar trend with the ones obtained from nanoindentation tests. Both MD and nanoindentation results show reduced elastic modulus with increased graphene concentration (1% to 5%). The Young's modulus from nanoindentation test are 5.35 ± 1.37 GPa, 5.08 ± 1.71 GPa, 4.43 ± 1.03 GPa and 4.58 ± 1.47 GPa for the nanocomposites with 1%, 3%, 5% graphene and neat epoxy samples, respectively. The coupon test of the same specimens showed Young's modulus value approximately 2.17 GPa, 2.50 GPa, 2.07 GPa and 2.12 GPa, for 1%, 3% 5% and neat epoxy, respectively. The coupon test data were less than the nanoindentation test results. The specimens were not prepared under vacuum which lead to form cavities in the matrix. Hence, the Young's modulus of neat epoxy form coupon test was less than literature value [56]. The presence of graphene in higher concentration increased the possibility of void content due to inter graphene layer gap and graphene-polymer gap. So, it is observed in both nanoindentation and coupon test data that 5%

graphene degrades the mechanical property compared to 1%. Similar trend was also noticed in MD and MM results.

It is to be noted that the standard deviation in nanoindentation test data is comparatively large. This is possibly due to indentation at multiple locations where different phases exist. At some locations the indentation might be occurring on epoxy which caused smaller values in Young's modulus. Some of the indentations might have occurred at graphene or graphene-epoxy phases which caused higher Young's modulus. Hence, the large variation was observed although the elastic modulus was calculated from the average of these values over sixteen different locations.

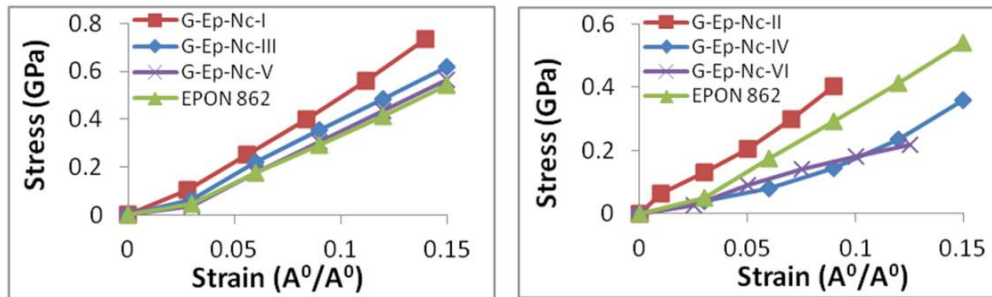


Figure 13. Stress-strain response of amorphous system with type-a and type-b graphenes

Material Configuration	Aspect ratio (AR)	Weight percentage of graphene	Young's modulus (MM): E (GPa)	shear modulus (MM): G (GPa)	Young's modulus from stress-strain (MD) response (GPa)	Young's modulus from micromechanics (MTM) model (GPa) [21]
G-Ep-Nc-I	AR-LW>=5, AR-LT>=150 (Type-a)	1%	4.56	1.73	5.00	2.96
G-Ep-Nc-II	AR-LW>=10, AR-LT>=480 (Type-b)	1%	3.45	1.16	4.27	2.63
G-Ep-Nc-III	AR-LW>=5, AR-LT>=150 (Type-a)	3%	3.98	1.37	3.98	3.6
G-Ep-Nc-IV	AR-LW>=10, AR-LT>=480 (Type-b)	3%	1.16	0.391	2.04	2.71
G-Ep-Nc-V	AR-LW>=5, AR-LT>=150 (Type-a)	5%	2.98	1.07	3.56	4.33
G-Ep-Nc-VI	AR-LW>=10, AR-LT>=480 (Type-b)	5%	1.34	0.45	1.77	4.69
EPON-862	Current work		2.5	0.95	3.42	
	Literature value [44]		3.362	1.22	3.362	

Table 4. Effect of graphene concentrations and aspect ratio on elastic constants

Material Configuration	Weight percentage of graphene	Young's modulus from MD simulation (GPa)	Material Configuration	Reduced elastic modulus from nanoindentation (GPa)
G-Ep-Nc-I	1%	5.00	ExpGEp-1%	5.35 ± 1.37
G-Ep-Nc-II	1%	4.27		
G-Ep-Nc-III	3%	3.98	ExpGEp-3%	5.08 ± 1.71
G-Ep-Nc-IV	3%	2.04		
G-Ep-Nc-V	5%	3.56	ExpGEp-5%	4.43 ± 1.03
G-Ep-Nc-VI	5%	1.77		
Neat Epoxy		3.362 [44]	ExpEpon	4.58 ± 1.47

Table 5. Comparison of Young's modulus obtained from MD simulation and nanoindentation tests

4.1.6.5 Dispersion and agglomeration effects

Figures 14-16 show MD simulated stress-strain responses in x, y and z directions of single, dispersed and agglomerated G-Ep models shown earlier in Figure. 4. In this case, x and y represent graphene length and width direction and z corresponds to thickness direction. The strain was applied independently in x, y and z direction. It is seen that stress generated in z direction is significantly low compared to x and y direction for all three cases. This occurs since stress in thickness direction is mostly matrix dominant whereas in-plane properties are dominated by stronger reinforcing graphene. The variations in stress-strain responses in x and y direction as seen in Figures 14 and 15 are mostly due to different graphene length to width ratio and variable cell size used in these models. The stress-strain plots in z-directions shown in Figures 10 and 16 indicate that at a typical design strain (4%), the stiffness of dispersed system is comparatively lower than the same in agglomerated system.

Table 6 shows Young's modulus of single, dispersed and agglomerated graphene system calculated from stress-strain responses in x, y and z directions. It is evident that in plane Young's modulus, E_x and E_y for the dispersed system (4.81 GPa, 8.76 GPa) is comparatively higher than the same in agglomerated system (3.99 GPa, 5.67 GPa). It is to be noted that higher modulus was observed in graphene width direction rather than length direction. As a result well dispersed graphene with high aspect ratio is seen to provide improved in-plane Young's modulus. It is seen that in-plane modulus in three graphene system is comparatively larger than single graphene system. This indicates that in-plane modulus is significantly influenced by graphene volume fraction since graphene's in-plane property is significantly high (Young's modulus, 1 TPa). However, the out of plane Young's modulus, E_z of the G-Ep nanocomposites is mostly controlled by stiffness of epoxy and non-bonded interaction (van der Waals) between graphene-

epoxy or graphene-graphene. The results show lowest E_z value (0.32 GPa) for three layer dispersed graphene system. The highest E_z value (2.36 GPa) was provided by three layer agglomerated system. The single layer graphene system shows E_z equals to 0.9 GPa. In agglomerated system, van der Walls interaction between graphene-graphene molecules possibly results such increased Young's modulus.

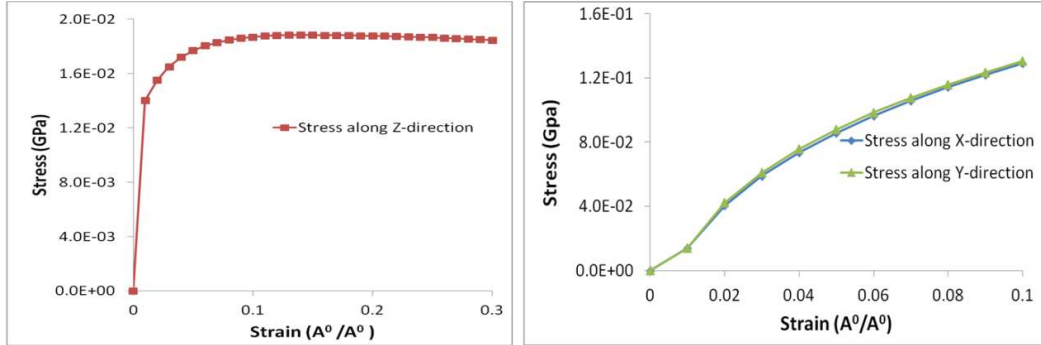


Figure 14. Stress-strain response in xx, yy and zz directions for SGM-G-Ep-I

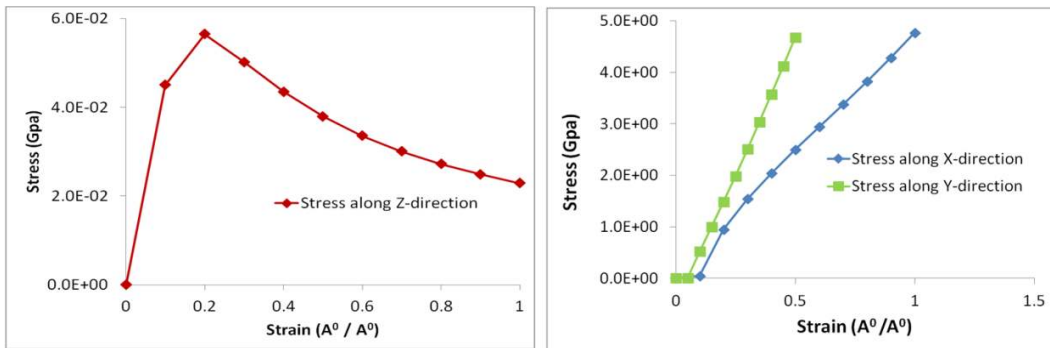


Figure 15. Stress-strain response in xx, yy and zz directions for SGM-G-Ep-II

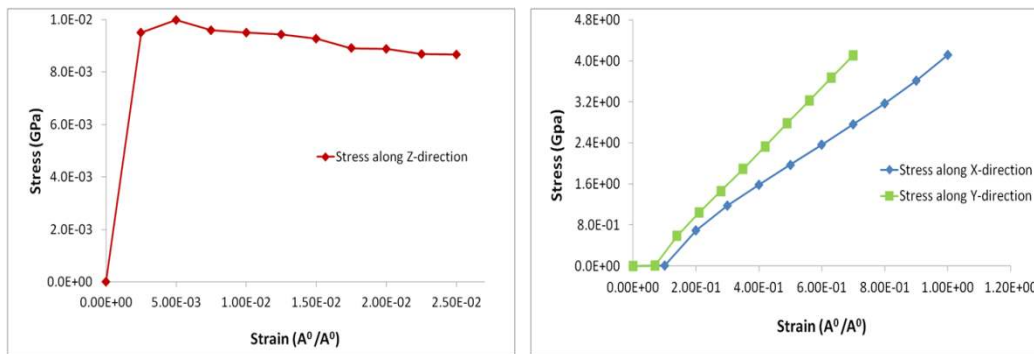


Figure 16. Stress-strain response in xx, yy and zz directions for SGM-G-Ep-III

Configuration	Number of graphene plates	E _x (GPa)	E _y (GPa)	E _z (GPa)
SGM-G-Ep-I	1	1.89	1.94	0.9
SGM-G-Ep-II	3 (dispersed)	4.81	8.76	0.32
SGM-G-Ep-III	3 (agglomerated)	3.99	5.67	2.36

Table 6. Young's modulus calculated from stress-strain response for stacked graphene model

4.1.6.6 Interfacial property

Interface between graphene and epoxy plays a significant role in load transfer mechanism between graphene and epoxy. The normal and shear displacement at the interface under applied strain have been investigated. Normal displacement of graphene leads to understand cohesive mechanism between graphene and epoxy whereas shear displacement provides information about the pullout mechanism. The unit cell configurations and relevant interface models under normal and shear displacements are shown in Table 3 and Figure. 5. As MD simulation was conducted under displacement control, a reaction force was developed on the graphene sheet. Figure.17 shows normal force verses displacement plots at the interface under mode-I separation for both type-a (AR-25.5) and type-b (AR-76.67) graphene plates. The trend of the force-displacement plot under mode-I is seen to be linear at the initial stage. It shows some nonlinearity before reaching to a peak point. The cohesive force then gradually drops to zero with increased displacement. In Figure 17, the maximum cohesive force and the displacement for Mode-I-a case are seen to be 80 picoNewtons and 1.6×10^{-4} nm but the same are observed to be 130 picoNewtons and 1.6×10^{-2} nm for mode-I-b. As a result the cohesive force is seen to be enhanced with increased aspect ratio of the graphene sheet. In this study, the magnitude of the

cohesive force is seen to be very small which mostly resulted from van der Waals force interaction between graphene and epoxy. Such cohesive force may be increased by minimizing the gap between graphene and epoxy or introducing a covalent bond between graphene and epoxy.

In Figure 18, shear force versus displacement plots are shown under pullout separation mode for both type-a (AR-25.5) and type-b (AR-76.67) graphene system. The maximum pullout force is observed to be 9 picoNewtons at a displacement of 0.05 nm for Mode-II-a. The same is seen to be 22 picoNewtons at a displacement of 0.15 nm for Mode-II-b. The maximum pullout force is also seen to be increased with increased graphene aspect ratio due to enhanced interfacial surface area. It is obvious that maximum pullout force under shear separation mode is significantly low compared to maximum cohesive force under normal separation mode. It is to be noted that interfacial properties were entirely dependent on the van der Waals interactions. This leads to comparatively weaker interfacial property. Thus in order to improve the interfacial properties chemical bonding was introduced between graphene and epoxy as shown in Figure.19. An ethylene chain was introduced as a connecting interface between graphene and carbon atom in epoxy. Figure 19 shows force vs. displacement plots of chemically bonded graphene epoxy system. The result shows significantly increased cohesive force of 40000 picoNewtons compared to 80 picoNewtons for chemically bonded graphene. This suggests functionalization of graphene to introduce chemical bonding at the interface and improved interfacial properties of graphene epoxy nanocomposites.

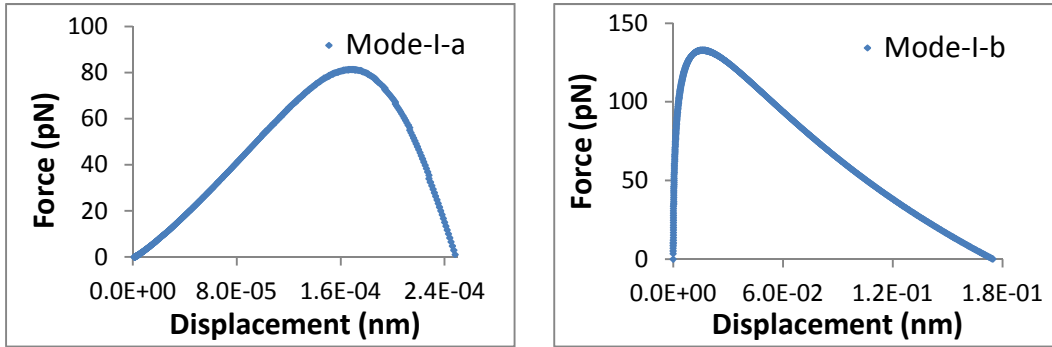


Figure 17. Force vs displacement curve for Mode-I cases

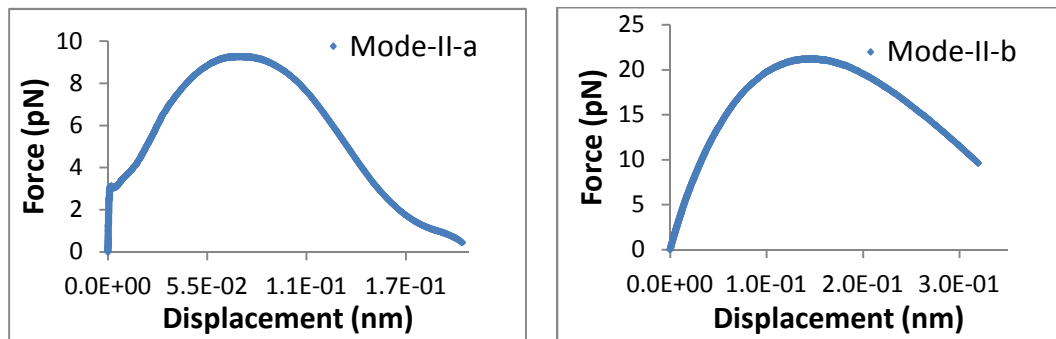


Figure 18. Force vs displacement curve for Mode-II cases

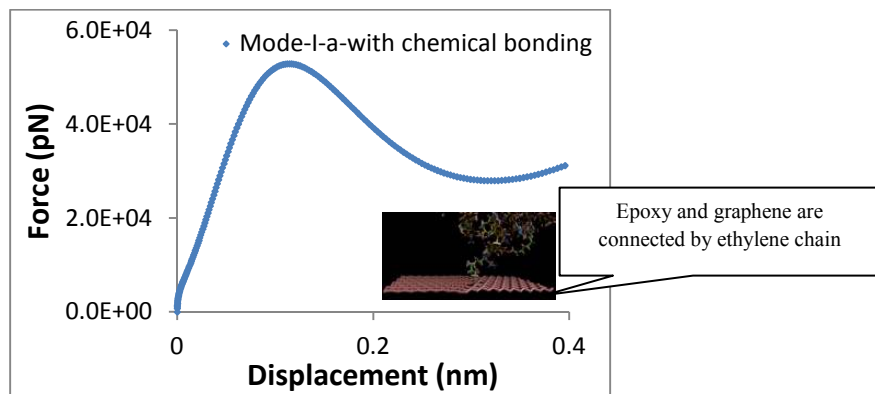


Figure 19. Force vs displacement curve for mode-I-a-with chemical bonding system

4.1.7 Conclusion

A molecular modeling frame work has been developed in order to determine Young's modulus, shear modulus and interfacial properties such as cohesive force and pullout force of graphene-epoxy nanocomposites. The effects of graphene weight concentrations, dispersion and aspect ratio have also been studied. The molecular energy, molecular density and radial density functions (RDF) have been analyzed for simulated model verification. The following conclusions are drawn from this investigation.

- i. The RDF of G-Ep system indicates that maximum concentration of epoxy molecules and graphene atoms is observed at an approximate pairwise separation distance 4 \AA .
- ii. The slope of molecular energy verses strain plots indicates progressive deformation in G-Ep system during MD simulation. The strength and elastic modulus of G-Ep nanocomposites are seen to be increased due to enhanced slope of molecular energy verses strain plots.
- iii. The atom density in MD model influences performance of G-Ep system. The Young's modulus is seen to be increased with enhanced atom density in MD model.
- iv. The RDF, molecular energy and atomic density of G-Ep system are influenced by graphene concentration and aspect ratios. High aspect ratio and graphene concentrations in the range 1-3% are observed to increase RDF, molecular energy and atomic density in G-Ep system.
- v. The Young's modulus and shear modulus data of G-Ep nanocomposites are seen to be comparatively 25-40 % higher than those of neat epoxy resin. The graphene concentrations in the range of 1-3% and graphene with higher aspect ratio provided

- improved Young's modulus. The Young's modulus determined by molecular modeling and nanoindentation tests showed a reasonable agreement.
- vi. It is observed that dispersed graphene provides improved in-plane Young's modulus of G-Ep in comparison to agglomerated graphene system. The out of plane modulus in aligned (unidirectional) G-Ep system is significantly low compared to in plane modulus in x and y direction.
 - vii. The maximum cohesive force and pullout force are seen to be increased with increased graphene aspect ratio. It is noticed that attachment of chemical bond at the interface significantly enhances cohesive force. This suggests functionalization of graphene for improved interfacial properties of G-Ep nanocomposites.

4.2 Molecular modeling and characterization of graphene-cellulose nanocomposites

Similar to previous work on graphene-epoxy nanocomposites, MD based modeling and characterization of graphene-cellulose nanocomposites was carried out for biomedical and biocomposite applications. Young's modulus, interfacial properties and effect of graphene concentration, dispersion on elastic constant were investigated using MD simulation. Theoretically calculated Young's modulus was compared with tensile test results.

4.2.1 Molecular modeling and simulation details

This work also considers MD simulation for three different types of graphene/cellulose systems. Firstly, the amorphous model is designed to study the effects of graphene weight concentrations and aspect ratios on Young's modulus. The stacked graphene model is used to study graphene's dispersion and agglomeration effect. Finally, the interfacial model is

considered for investigating normal and shear separation force at the graphene-cellulose interface region. The following sections describe the details about these models.

4.2.1.1 Amorphous models

Cellobiose is a repeat unit for cellulose (Figure 20). Twenty cellobiose units were used in constructing a long single cellulose chain. Each cellulose molecule consists of 843 atoms [7]. Based on variation in aspect ratio, as described in earlier section 4.1.1, each graphene-cellulose unitcell consists of type-a or type-b graphenes. Amorphous unit cells were constructed with 1%, 3% and 5% graphene weight concentrations by using one, three and five graphene sheets in individual system. This was done differently compared to graphene-epoxy system. The average density for all the amorphous systems was maintained within the range of 1.3 g/cc to 1.4 g/cc. This was carried out by changing number of cellulose molecules in individual system. All the GC unicells with type-a graphene consist of 11 cellulose molecules whereas unitcells with type-b graphene consist of 44 cellulose molecules. Periodic boundary condition (PBC) was applied on each unitcell during the equilibration and deformation process. The details about each amorphous unit cell after equilibration are shown in Table. 7.

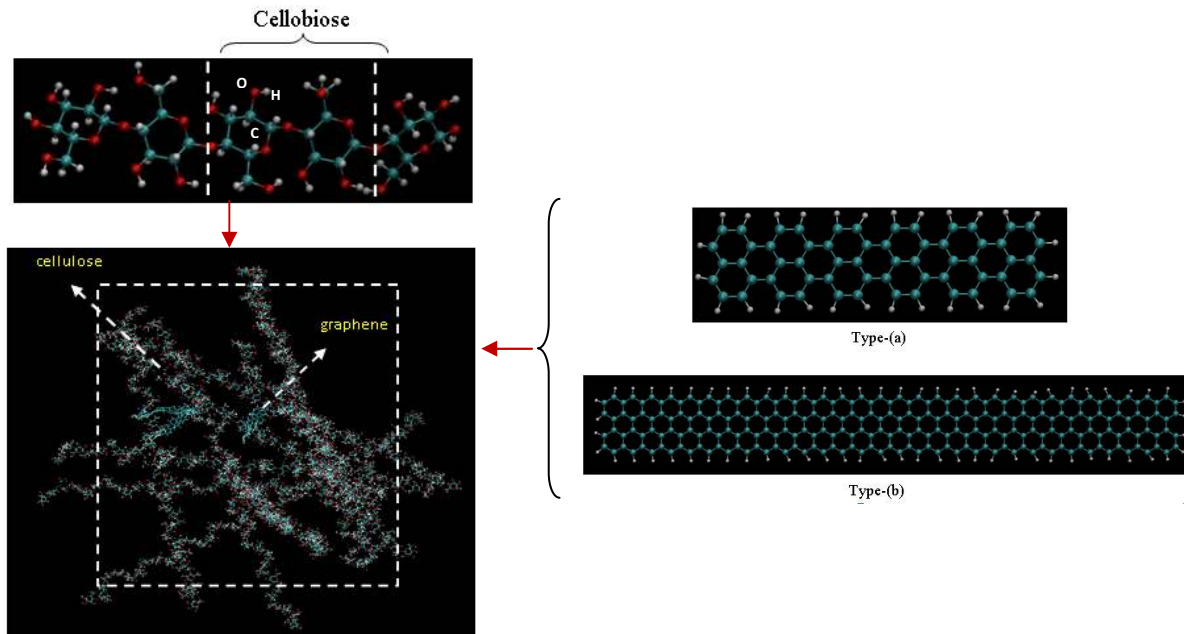


Figure 20. Graphenes (Type-a or Type-b) embedded in cellulose matrix to form amorphous graphene-cellulose system

Material Configuration	Aspect ratio (AR)	Weight percentage of graphene	Unit cell length (\AA^0)
GC-I	AR-LW \geq 5, AR-LT \geq 150 (Type-a)	1%	47.39
GC-II	AR-LW \geq 10, AR-LT \geq 480 (Type-b)	1%	74.63
GC-II	AR-LW \geq 5, AR-LT \geq 150 (Type-a)	3%	47.35
GC-IV	AR-LW \geq 10, AR-LT \geq 480 (Type-b)	3%	76.10
GC-V	AR-LW \geq 5, AR-LT \geq 150 (Type-a)	5%	48.70
GC-VI	AR-LW \geq 10, AR-LT \geq 480 (Type-b)	5%	72.73
Neat Cellulose			16.00

Table 7. Material configuration of each graphene-cellulose unitcell

Prior to applying deformation, molecules in each unit cell were relaxed in order to attain minimum residual stress in the system. This was done by molecular mechanics approach while achieving minimum energy at stable structural configurations (i.e. bond, angle, dihedral etc). Conjugate gradient algorithm was used for 1000 steps with 10^{-8} kcal/mole energy tolerance. Afterwards, the systems were equilibrated by isothermal-isobaric (NPT) molecular dynamics simulation for 30000 steps at 300 K temperature and 0.0 atm pressure. Size of each timestep was 0.1 femtoseconds. This leads to reduce the system's average pressure to significantly small. Nose-Hoover barostat was used to add damping parameter into the fluctuating pressure. Verlet time integration scheme was applied throughout the whole simulation.

At this stage, the amorphous systems were subjected uniaxial deformation with 0.0001 strain in every 100 steps. Size of each step was 0.7 fs and 0.5 fs for type-a and type-b systems, respectively. After each deformation, the atoms undergo isothermal molecular dynamics (NVT) for 1000 MD steps at 0.1K temperature.

4.2.1.2 Stacked graphene-cellulose models

Three different stacked graphene model (SGM) with single, agglomerated and dispersed graphene were constructed as shown in Figure 21. The objective is to study the effects of single, dispersed and agglomerated graphene on the mechanical properties of GC system. Each semi-crystalline GC unit cell contains 3% graphene with average density of 1.3-1.4 gm/cc. Unlike amorphous models, the graphenes reside among the amorphous cellulose with local order. All the unit cells were subjected to periodic boundary condition. A brief description of SGM is given in Table 8.

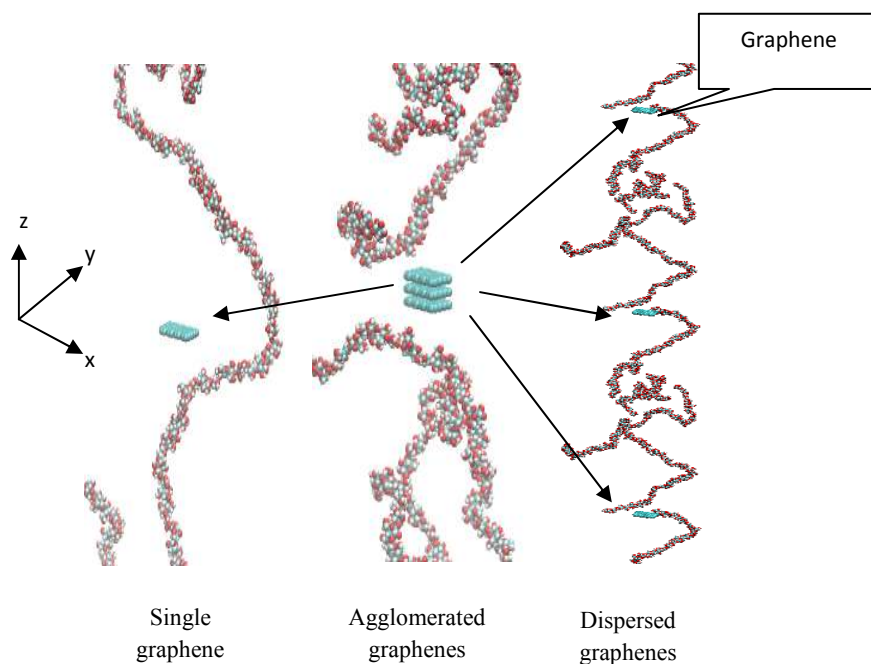


Figure 21. Schematic diagrams for cellulose based stacked graphene models

Configuration	Unit cell dimension (\AA^0)	Number of graphene plates
SGM-GC-I	a=9.84, b=19.02, c= 354.87	1
SGM-GC-II	a=9.84, b=19.02, c=1063.94	3 (Dispersed)
SGM-GC-III	a=9.84, b=19.02, c=557.35	3 (Agglomerated)

Table 8. Unit cell configuration for stacked graphene models

Similar to amorphous models, the SGMs were also equilibrated prior to applying deformation. Initially, optimum molecular configurations were achieved by minimizing the system energy based on conjugate gradient method for 1000 iterations. During energy minimization, the cell dimensions in x, y and z directions were also adjusted. Then, the systems were relaxed by isothermal-isobaric (NPT) molecular dynamics for 30000 steps with average step size of 0.5-1.0 femtoseconds. This was followed by deformation in x, y and z directions separately. The average applied strains were 0.00001 along z-direction and 0.001 along x and y directions. After each deformation, the atoms were subjected to isothermal (NVT) molecular dynamics for 100 steps with time step size of 0.5-1.0 femtoseconds. Nose-Hoover thermostat

was used. In addition to MD, the atoms in the systems were also subjected to Langevin dynamics with a damping term of 10 femtoseconds. After every applied deformation the running averaged hydrostatic stress $\bar{\sigma}$ was calculated using Equation (21). The Young's modulus was obtained from the slope of the linear regime of the stress-strain curve.

4.2.1.3 Interface models

Figure 22, shows the interface models for GC system under mode-I and mode-II separation scheme. A single graphene layer was embedded in each system having a number cellulose chains. Initially, the space between cellulose and graphene sheet was kept less than $2A^0$. Mode-I-a and Mode-II-b consist of 5306 and 11719 atoms respectively. Mode-II-a and Mode-II-b consist of 10370 and 22668 atoms respectively.

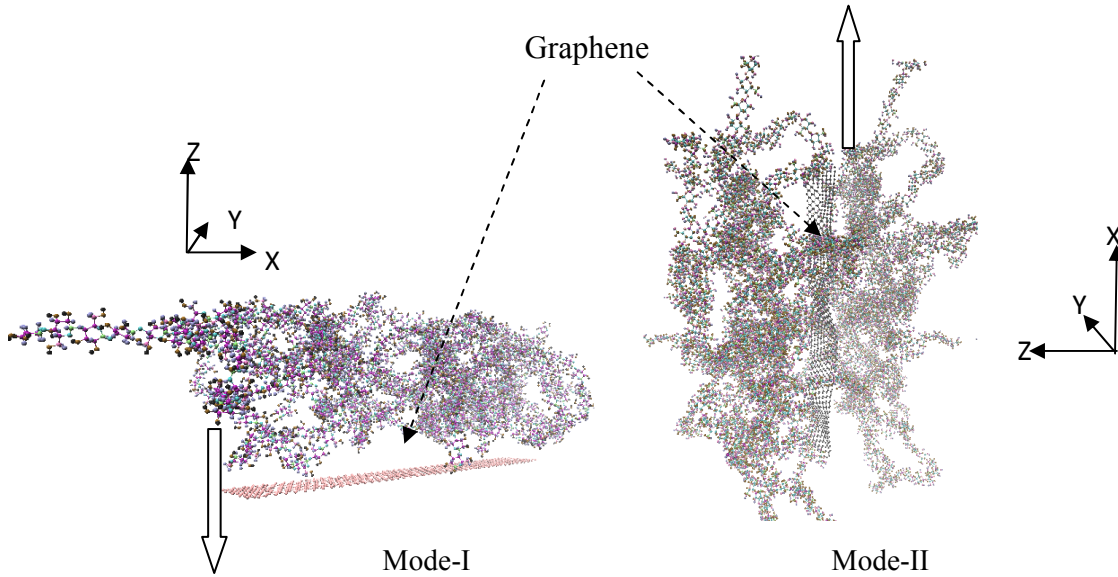


Figure 22. Mode-I and Mode-II separation of graphene from cellulose matrix

In this study the weight percentage of graphene is considered to be higher ($> 3\%$) in order to emphasize the effect of graphene on van der Waals interaction between cellulose and graphene. The details about GC unit cells are provided in Table 9.

Configuration	Graphene sheet dimension (length x widths) (\AA^0)²	Interaction force type
Mode-I-a	39.36 x 19.02	Normal
Mode-I-b	118.08 x 19.02	Normal
Mode-II-a	39.36 x 19.02	Shear
Mode-II-b	118.08 x 19.02	Shear

a = AR-LW 2.07 and b= AR-LW 6.20

Table 9. Unit cell configuration for interface model

Prior to transverse or longitudinal movements of graphene plate, each system's energy was minimized by conjugate gradient method with 1000 steps. Energy and force tolerance were in the order of 10^{-10} kcal/mole. As shown in Figure 22, both normal and shear separation forces were calculated on a slowly displaced graphene sheet in normal and shear directions, respectively [23]. The normal and shear movements lead to mode-I and mode-II fracture phenomena. Average displacement rate of graphene was 0.0001-0.00001 \AA^0 per femtoseconds for mode-I case and 0.001 \AA^0 per femto seconds for mode-II case. Velocity verlet scheme was used to update position and velocities of atoms while displacing the graphene in both normal and shear directions.

4.2.2 Results and discussion

The effects of graphene concentrations, aspect ratios and agglomeration on stress strain response and elastic constant of GC system are discussed in this section. Both amorphous as well as semi-crystalline systems are considered. The graphene/cellulose interfacial property is also highlighted using an interface model.

4.2.2.1 Effect of graphene weight concentration and aspect ratio on stress-strain response

The stress-strain response was calculated while deforming the unit cells under isothermal condition. Temperature was kept very low while deforming the unit cells. This was done in order

to reduce the effect of kinetic energy on system's overall stress. Hence, the change in stress was mostly dependent on the topological deformation (i.e. change in bond, angle or dihedral energy) of the amorphous polymer chains. In Figures 23 and 24, the stress-strain responses of GC amorphous systems with various graphene concentrations and aspect ratios are plotted. The Young's moduli calculated from these plots are provided in Table 10. It is clearly observed from the slopes of stress strain plots in Figures 23 and 24 that graphene enhances Young's modulus of cellulose based nanocomposites. Figure 23 shows increased Young's modulus of GC system with increased weight concentration of graphene (type-a, AR=150) in the range 1% to 5% compared to neat cellulose. It is evident in Table 4 that the Young's modulus of neat resin is 11.93 GPa whereas GC systems show the corresponding value 12.77 GPa, 20.63 GPa and 25.70 GPa with 1%, 3% and 5% graphene concentration. So, the results show more than 100 % enhancement of Young's modulus with 5% nanographene reinforcement. It is to be noted that all the stress-strain curves are seen to be well distinguished for type-a graphene reinforced GC system in Figure 23. Such feature was not prominent in Figure 24, type-b based systems. It is apparent in Figure 24 that reinforcement of 5% graphene (type-b, AR-480) improves the Young's modulus of GC system almost 75%. However, the effect of various weight concentrations of graphene (1%, 3% and 5%) in Figure 24 was not significant. In such cases, the stress-strain curves are seen to be very similar. Possibly, the numerical experiment in this case undergoes some errors in calibration scheme, i.e. ensemble, equilibration process etc.

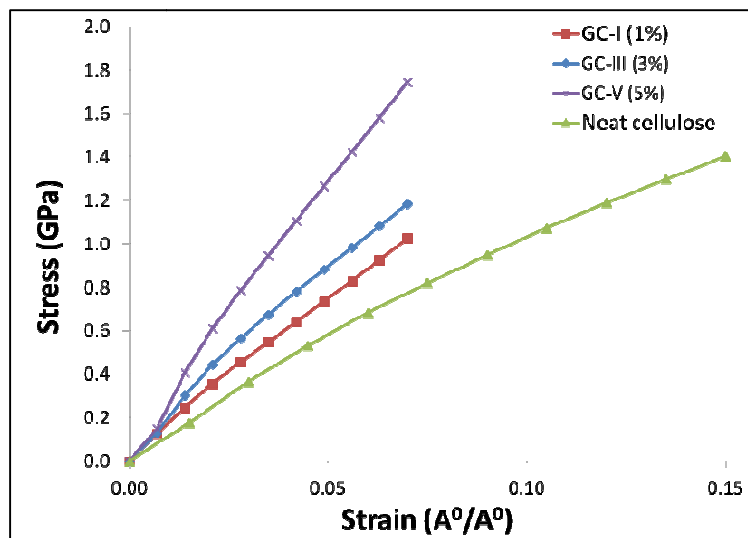


Figure 23. Stress-strain response of graphene/cellulose systems with type-a graphene

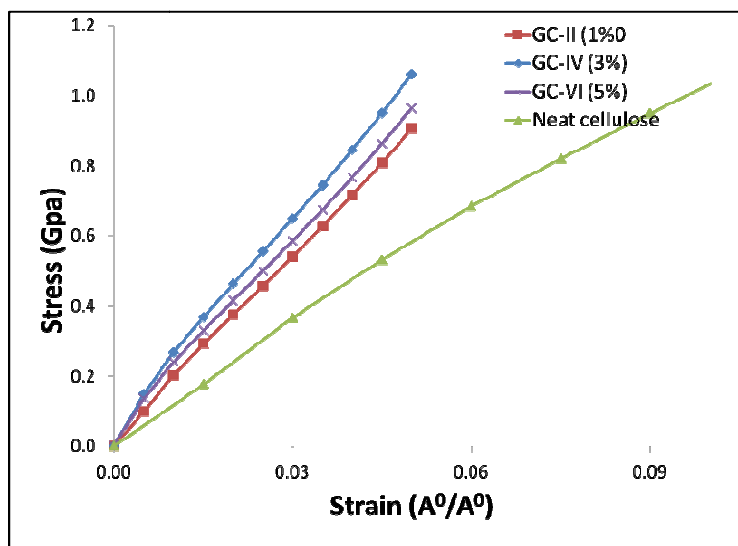


Figure 24. Stress-strain response of graphene/cellulose systems with type-b graphene

		Theoretical results		Experimental results		
Material Configuration in MD simulation	Aspect ratio (AR)	Weight percentage of graphene	Young's modulus (GPa)	Material Configuration in tensile tests	Weight percentage of graphene	Young's modulus (GPa)
GC-I	AR-LW \geq 5, AR-LT \geq 150 (Type-a)	1%	15.03	Exp-G-C-Nc-I	1.2%	14.75 \pm 1.84
GC-II	AR-LW \geq 10, AR-LT \geq 480 (Type-b)	1%	18.10			
GC-III	AR-LW \geq 5, AR-LT \geq 150 (Type-a)	3%	20.63	Exp-G-C-Nc-II	2%	16.57 \pm 2.06
GC-IV	AR-LW \geq 10, AR-LT \geq 480 (Type-b)	3%	21.52			
GC-V	AR-LW \geq 5, AR-LT \geq 150 (Type-a)	5%	25.70	Exp-G-C-Nc-III	5%	18.39 \pm 3.83
GC-VI	AR-LW \geq 10, AR-LT \geq 480 (Type-b)	5%	19.50			
Neat Cellulose (current work)			11.93	14.13 \pm 1.28		
Neat Cellulose (literature value)			10.42 [7]			

Table 10. Comparison of theoretically calculated Young's modulus and experimental data for amorphous graphene/cellulose systems

Finally, the MD simulation based stress-strain data was compared with in-house tensile test data of GC system as shown in Figure 25 and Table 10. The graphene weight percentages in these samples were slightly different from those of MD simulated test samples. In the experiments, 1.2%, 2% and 5% of graphene was used to prepare graphene/cellulose system. These data show a reasonable agreement with the Young's modulus calculated from MD simulation as shown in Table 10. The experimentally obtained Young's moduli have increasing trend with

respect to increasing weight percentage of graphene. This trend was also noticed in Young's modulus obtained from MD simulation. The linearly elastic region of stress-strain data in tensile test showed a reasonable resemblance with the simulated stress-strain response in MD simulation.

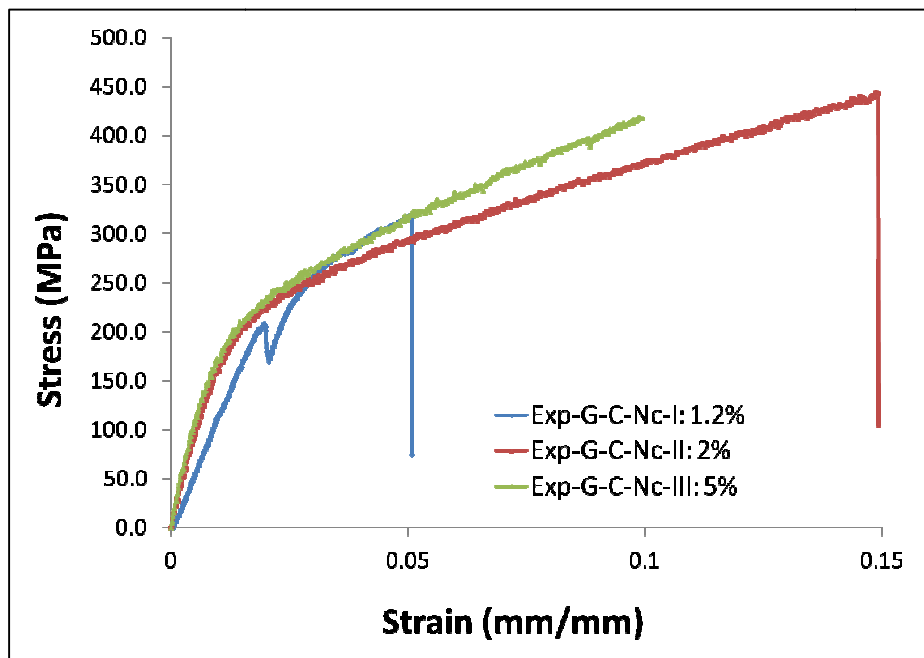


Figure 25. Stress-strain response of graphene/cellulose from tensile tests

4.2.2.2 Structural Configurations

The structural configurations of the GC amorphous system are discussed in this section using atomic pairwise radial distribution function (RDF), $g(r)$. Usually amorphous solid structures rarely show any long range order. Hence, the probability of any pair of atoms at a certain distance resembles the presence of disorder in the system. In this study, total RDF was analyzed in order to determine cellulose and graphene distribution pattern in a periodic unit cell.

Total RDF is constructed based on contribution from all atoms available in the system within the cutoff distance 8\AA . In Figure 26, RDFs from different amorphous systems listed in

Table 10 were observed to be very similar. The absence of any sharp peak ensures amorphous nature of the system. In all these amorphous models there is no correlation in distribution of atoms which are separated by distance more than 4.0 \AA . Structurally, all these graphene based amorphous systems are very similar to the neat cellulose. Hence, further analysis was carried out in order to study the effect of weight concentrations and aspect ratio on RDF. This can be accomplished by studying the structural backbone of both cellulose and graphene. As GC systems are mostly constructed by carbon atoms and carbon-carbon bonds are the backbone of the cellulose structure, the further investigation is focused on RDF of total carbon-carbon bonds in systems with type-a and type-b graphenes as shown in Figure 27. In both the cases a distinguishable sharp peak was observed at $2.1\text{-}2.2 \text{ \AA}$. These sharp peaks correspond to carbon atoms which are connected by one or two bonds. No evidence of local order in carbon atoms was also observed at a distance greater than 5 \AA . The effect of weight concentration is observed in type-a graphene based samples in terms of clearly distinguishable peaks around $2.1\text{-}2.2 \text{ \AA}$. However, this feature is diminished in type-b graphene based systems. This might explain the similarity in stress-strain response data for amorphous samples containing type-b graphenes.

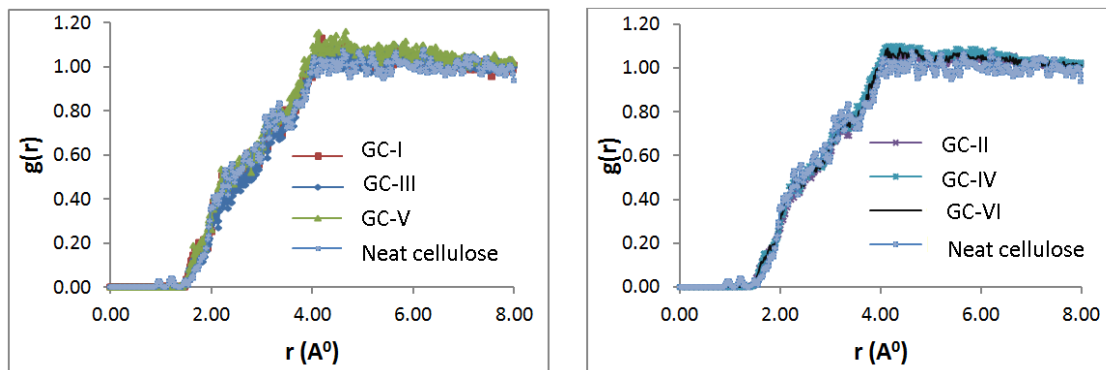


Figure 26. Radial distribution function of amorphous graphene-cellulose system with type-a (Left) and type-b (Right) graphene

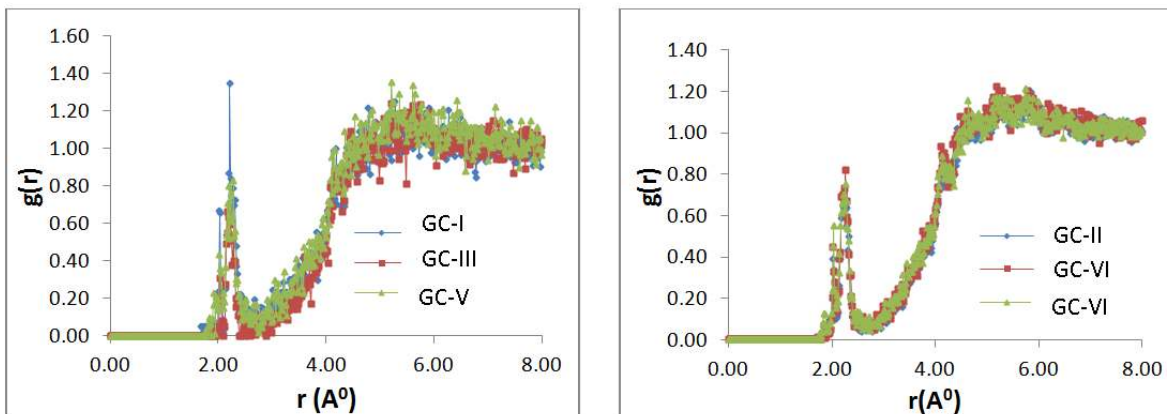


Figure 27. Radial distribution function for carbon-carbon atoms in amorphous graphene-cellulose system with type-a (Left) and type-b (Right) graphene

4.2.2.3 Energy evolution during deformation process

Typically the energy evolution due to applied deformation is related to the Young's modulus of the system. In this case the molecular energy is taken into consideration since it is directly related to the structural deformation of the polymer. The change in potential energy, $\Delta E = E - E_0$ during deformation in all GC systems is shown in Figure 28, where E corresponds to the energy at any instant and E_0 relates to initial energy. All these ΔE curves show similar behavior at the early stage of deformation. The energy in each system gradually increases with increasing applied strain. The slopes of these curves reflect the stiffness of the system. It is seen in Figure 28 that potential energy increased at highest rate in GC-V system compared to GC-I and III. This can be correlated to the higher Young's modulus of GC-V samples calculated from the slope of stress strain plot in Figure 23 and 24. It is observed in Figure 24, the stress-strain plots were very similar to each other for type-b graphene based samples. This was also reflected on the ΔE curves in Figure. 28. Potential energy is seen to change almost at similar rate in GC-II, IV and VI samples. Thus effect of weight concentration is not significant in type-b samples.

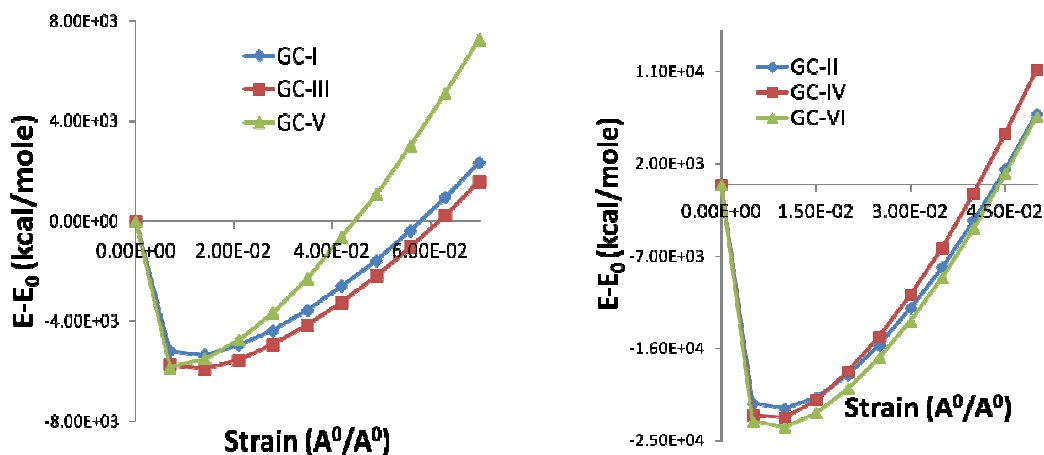


Figure 28. Change in potential energy in different amorphous systems

Left: type-a and Right: type-b

4.2.2.4 Bond stretch and bond angle evolution during deformation process

This analysis was carried out to study intrinsic structural parameters such as pairwise bond stretch and bond angle evolution due to applied strain. Pairwise bond stretch, and bond angle play an important role in the stiffness of the polymer. The atoms in the polymer molecule can be imagined as connected masses by springs. Hence, the stretching rate of the pairwise bond, and deflection rate of the bond angle due to applied strain are correlated to the stiffness of the polymer chain. For type-a graphene in Figure 29, the average pairwise bond stiffness in GC-V (5%) seems to be comparatively higher than other two cases. The slope of the curve is the steepest among all other cases. GC-I and GC-III possess very similar slopes. However, stiffer pairwise bonds in GC-III results less stretch in the bond length. Type-b graphene based amorphous systems in Figure 29 show different bond stretch behavior compared to previous case. In GC-II, IV and VI, the average pairwise bond stretch rates with respect to applied deformation are almost same. These curves are almost parallelly spaced with different initial bond

lengths. Hence, this may explain the highly correlated stress-strain response and ΔE for type-b based amorphous systems.

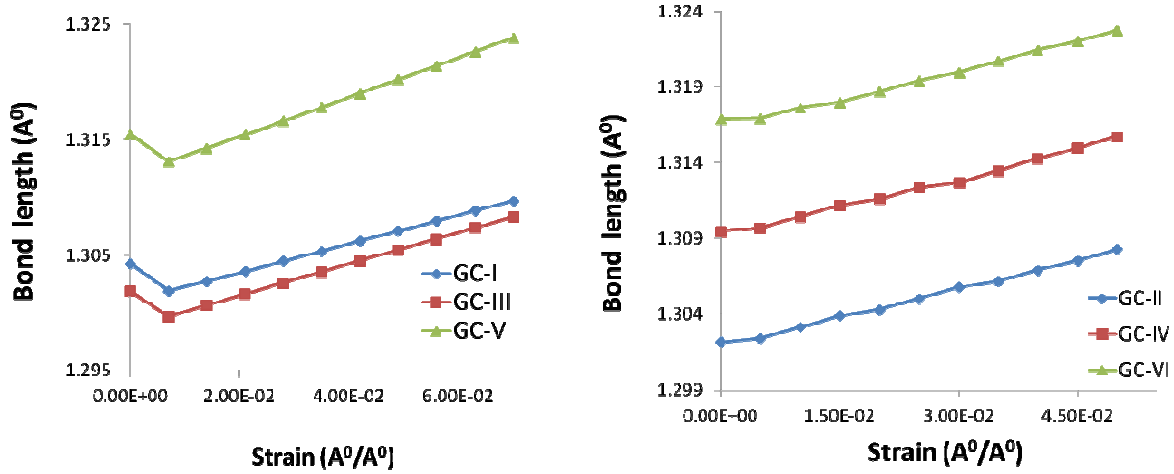


Figure 29. Pairwise bond stretch under applied strain in different amorphous systems

Left: type-a, Right: type-b

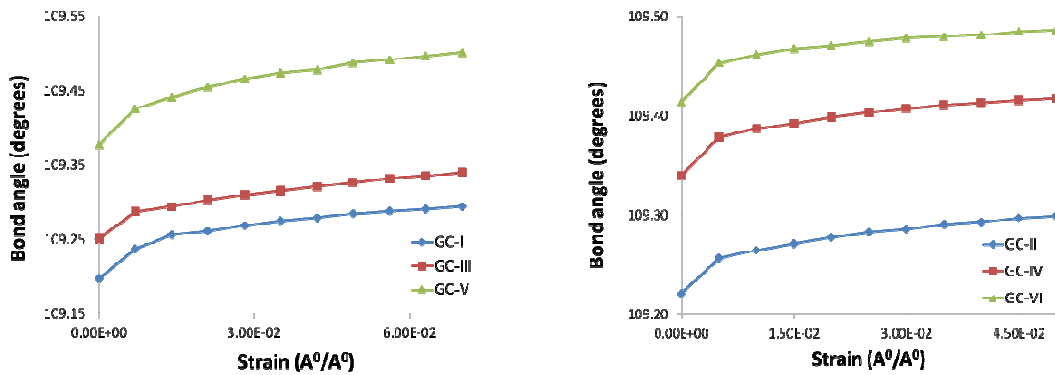


Figure 30. Bond angle evolution under applied strain in different amorphous systems

Left: type-a, Right: type-b

Similar to pairwise bond stretch, bond angle deflection of GC system is another important parameter which is shown in Figure 30. For both type-a and type-b graphenes, the average bond angle evolution due to applied deformation has noticeable resemblance with the bond length evolution. In Figure 30, bond angle increment rate with respect to applied strain is higher in GC-

V compared to GC-I and III. Average bond angle increment profiles are mutually parallel for GC-II, IV and VI systems. Initial bond length or bond angles are observed to be less in GC-I, III and V compared to GC-II, IV and VI which correlate with the geometry of graphene.

4.2.2.5 Effect of graphene dispersion on elastic property of graphene-cellulose nanocomposites

Stacked graphene model is used in studying the effect of agglomeration on mechanical properties of graphene/cellulose nanocomposites. Figure 31-33 show MD simulated stress-strain responses in x, y and z direction of single, dispersed and agglomerated GC models. In this case, x and y represent graphene length and width direction and z corresponds to thickness direction. The strain was applied independently in x, y and z directions. It is seen that stress generated in z direction is significantly low compared to x and y direction for all three cases. This occurs because stress in thickness direction is mostly matrix dominant whereas in plane properties are controlled by stronger reinforcing graphene. The variations in stress-strain responses in x and y direction as seen in Figures 31-33 are due to different graphene length to width ratio and variable cell size used in these models. Table 11 shows Young's modulus of single, agglomerated and dispersed graphene-cellulose systems calculated from stress-strain responses in x, y and z directions. It is evident that in plane Young's modulus, E_x and E_y for the dispersed system (11.78 GPa, 32.00 GPa) is comparatively higher than the same in agglomerated system (11.72 GPa, 21.81 GPa). It is to be noted that higher modulus was observed in graphene width direction rather than length direction. As a result well dispersed graphene with high aspect ratio is observed to provide improved in-plane Young's modulus. It is noticed that in-plane modulus in three agglomerated graphene based system is comparatively larger than single graphene system. This indicates that in-plane modulus is significantly influenced by graphene volume fraction since graphene's in-plane property is significantly high (Young's modulus, approximately 1

TPa). However, the out of plane Young's modulus, E_z of the GC nanocomposites is mostly controlled by E_z of matrix and van der waals interaction between graphene-cellulose or graphene-graphene. The results show lowest E_z value (0.07 GPa) for three layer dispersed graphene system whereas highest E_z value (2.81 GPa) was provided by three layer agglomerated system. The single layer graphene system shows E_z equals to 0.08 GPa. In agglomerated system, strong van der walls interaction between graphene-graphene possibly results such increased Young's modulus. From observation of non-bonded energy evolution between single and dispersed semi-crystalline models it was found that, the van der Waals energy changes by 4650 kcal/moles as number of graphene increases from one to three. This shows the effect of number of graphenes on the non-bonded energy of the system. Based on the results obtained from these semi-crystalline models, it can be concluded that graphene dispersion plays a vital role in controlling mechanical property in graphene based nanocomposites.

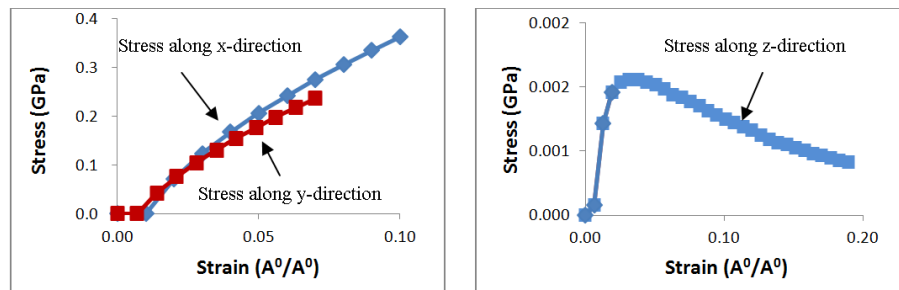


Figure 31. Stress-strain response of SGM with single graphene

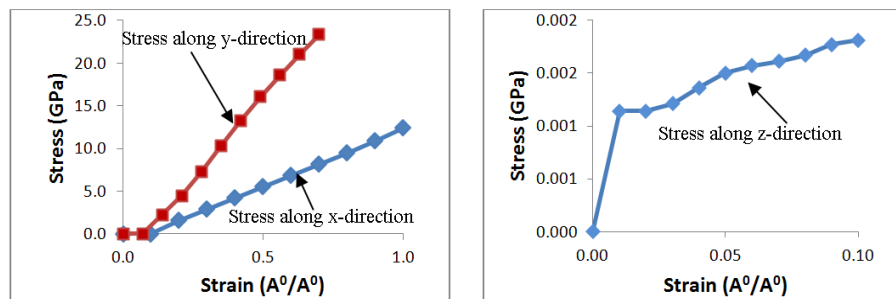


Figure 33. Stress-strain response of SGM with three dispersed graphenes

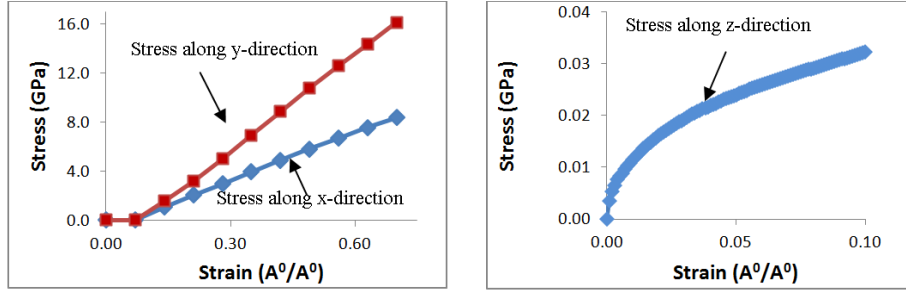


Figure 32. Stress-strain response of SGM with three agglomerated graphenes

Configuration	Number of graphene plates	E_x (GPa)	E_y (GPa)	E_z (GPa)
SGM-GC-I	1	4.04	3.63	0.08
SGM-GC-II	3 (dispersed)	11.78	32.00	0.07
SGM-GC-III	3 (agglomerated)	11.72	21.81	2.81

Table 11. Young's modulus calculated from stress-strain response for semi-crystalline model

4.2.2.6 Interfacial Property between graphene and cellulose

Interface between graphene and cellulose plays a significant role in load transfer mechanism between graphene and cellulose. In this study the normal and shear displacement at the interface under applied strain have been investigated. The normal displacement of graphene from the cellulose matrix helps to understand the nature of mode-I or cohesive separation at nanoscale whereas shear movement highlights on the mode-II or pullout separation. The unit cell configurations and relevant interface models under normal and shear displacements are shown in Table 9 and Figure 22. As MD simulation was conducted under displacement control, a reaction force was developed at the graphene due to the non-bonded interaction. This forces changes as the graphene moves away from the cellulose matrix.

Figure 34 shows force versus displacement plots at the interface under Mode-I separation for both type-a (AR-25.5) and type-b (AR-76.67) graphene sheets. The trend of the force-displacement plot under mode-I is seen to be linear at the initial stage. It shows some nonlinearity before reaching to a peak point. In Figure 34, the maximum cohesive force and the displacement for mode-I-a case are seen to be 88.08 picoNewtons and 0.056 nm but the same are observed to be 1116.60 picoNewtons and 1.6×10^{-3} nm for mode-I-b. As a result the maximum cohesive force is noticed to be enhanced with increased aspect ratio of the graphene sheet. Unlike cohesive force, the displacement at normal separation is observed to be much lower in mode-I-b.

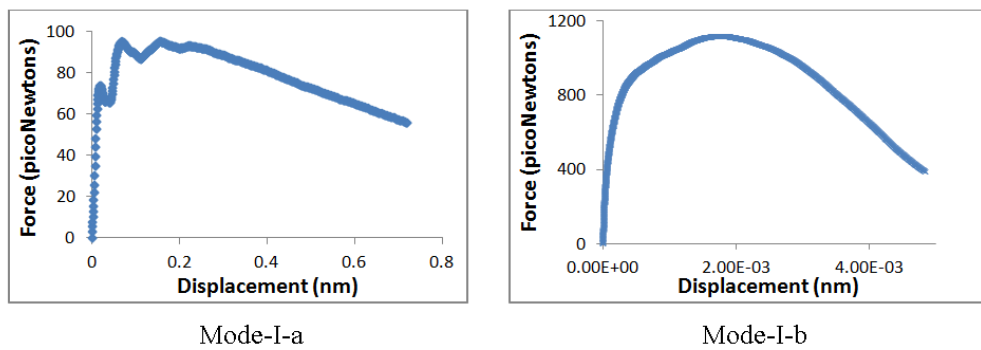


Figure 34. Force vs displacement plot of graphene in Mode-I-a and Mode-I-b cases

In Figure 35, shear force versus displacement plots are shown under pullout separation mode for both type-a (AR-25.5) and type-b (AR-76.67) graphene system. The maximum pullout force is observed to be 6 picoNewtons at a displacement of 5.02×10^{-3} nm for Mode-II-a sample. The same is seen to be 118 picoNewtons at a displacement of 0.2 nm for Mode-II-b sample. The maximum pullout force is also seen to be significantly improved with increased graphene aspect ratio due to enhanced interfacial surface area. It is obvious that maximum pullout force under shear separation mode is significantly low compared to maximum cohesive force under normal separation mode. It is to be noted that interfacial properties were entirely dependent on the non-

bonded interactions i.e. van der Waals force. This leads to comparatively weaker interfacial property. This study depicts a very useful picture of the correlation of nanoparticle size with load transfer property. It was observed in graphene-epoxy system that incorporation of covalent bond enhance interfacial properties significantly. As a result, functionalization of graphene by introducing a covalent bond is recommended for improving interfacial properties.

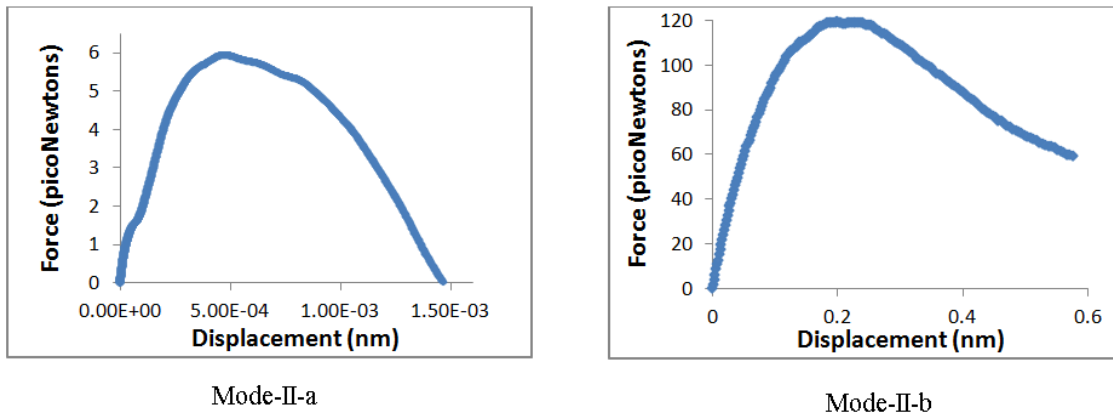


Figure 35. Force vs displacement plot of graphene in Mode-II-a and Mode-II-b cases

4.2.3 Conclusion

Classical molecular dynamics (MD) is applied to calculate the elastic properties of graphene-cellulose nanocomposites. The effects of graphene weight concentrations, dispersion and aspect ratio have also been studied. The following conclusions are drawn from this study:

- i. The Young's moduli of GC nanocomposites are seen to be comparatively higher than those of neat cellulose. The graphene concentrations in the range of 3% to 5% and graphene with higher aspect ratio provided improved Young's modulus. The Young's modulus determined by molecular modeling has good agreement with the experimental results.
- ii. The dispersed graphene provides improved in-plane Young's modulus of GC in comparison to agglomerated graphene system. The out of plane modulus in

aligned (unidirectional) GC system is significantly low compared to in plane modulus in x and y direction. This is interpreted in terms of the effect of van der Waals interactions between graphene layers.

- iii. The total RDF of GC system indicates that maximum concentration of cellulose molecules and graphene atoms is observed at an approximate pairwise separation distance 4 \AA . The RDFs of pairwise carbon-carbon atoms were also analyzed. For smaller graphene with 1% weight concentration, the RDF is slightly distinguishable. The first peak at $2.5\text{-}3 \text{ \AA}$ indicates the average bond distance between carbon atoms.
- iv. The slope of molecular energy verses strain plots indicates progressive deformation in GC system during MD simulation. The elastic moduli of GC nanocomposites are seen to be increased due to enhanced slope of molecular energy verses strain plots.
- v. The pairwise bond length and angle evolution in 5% graphene based system seems to be slightly higher compared to 1% and 3% graphene based amorphous systems.
- vi. The maximum cohesive force and pullout force are seen to be increased with increased graphene aspect ratio. This gives an insight on load transfer mechanism between graphene and cellulose matrix.

CHAPTER 5

MULTISCALE SIMULATION OF GRAPHENE-EPOXY NANOCOMPOSITES USING PERIDYNAMICS AND MOLECULAR DYNAMICS

In the previous chapter the discussions were solely limited to atomistic scale. The elastic and interfacial properties were calculated using classical MD simulation. All the analyses were done within few angstroms. But in real life applications most of the analyses are done in continuum scale (nanometer to meters). It is not computationally feasible to use atomistic simulation methods at continuum scale. At the same time atomistic scale models play vital role in explaining intrinsic physical properties or phenomena of material. Hence, it is a challenging and interesting problem to build up a multiscale modeling framework which considers a macroscopic problem and eventually establishes seamless connection with atomistic model. Peridynamics (PD) formulation is considered to define continuum scale problem. The seamless multiscale coupling method works in a hierarchical manner in order to scale down to atomistic model at few angstrom scale from several nanometer scales. This method is not been proposed in literature. The details are discussed in this chapter.

5.1 Fundamental formulation of peridynamics

The balance equation between rate of change of linear momentum and applied force on a deformable body Ω (Figure 36) develops the fundamental equation in classical continuum mechanics as follows

$$\rho(\mathbf{x})\ddot{\mathbf{u}}(\mathbf{x},t) = \nabla \cdot \boldsymbol{\sigma} + \mathbf{b}(\mathbf{x},t) \quad (27)$$

where, $\mathbf{x} \in \Omega$, t is time, ρ is the density, $\ddot{\mathbf{u}}$ is the acceleration vector, $\boldsymbol{\sigma}$ is the stress tensor and \mathbf{b} is the body force. This differential equation is not well defined at the discontinuities. PD formulation introduces integral form of this equation in order to mitigate this issue by calculating the force density on each material point [37, 38]. The new form of equation of motion is

$$\rho(\mathbf{x})\ddot{\mathbf{u}}(\mathbf{x},t) = \int_{\Omega_x} \mathbf{f}(\eta, \xi) dV_x + \mathbf{b}(\mathbf{x},t) \quad (28)$$

where, deformable body Ω is represented with respect to an arbitrary frame of reference, \mathbf{f} is the pairwise force applied on particle at x by a neighborhood particle at x' and Ω_x is a spherical region in the neighborhood region of x with radius δ . According to Figure 36, this region is referred to as “horizon”. The relative position and displacement vectors are $\xi = x' - x$ and $\eta = \mathbf{u}(x',t) - \mathbf{u}(x,t)$ respectively. For a certain $\delta > 0$, $\mathbf{f}(\eta, \xi) = 0$ for all η when $\|\xi\| > \delta$. This integral equation can be written more elaborately in terms of bond between x and x' [51, 52]. The integral equation and it's discrete form are shown in equations (29.1) and (29.2).

$$\rho(\mathbf{x})\ddot{\mathbf{u}}(\mathbf{x},t) = \int_{\Omega_x} \left\{ \underline{\mathbf{T}}[\mathbf{x},t] \langle \mathbf{x}' - \mathbf{x} \rangle - \underline{\mathbf{T}}[\mathbf{x}',t] \langle \mathbf{x} - \mathbf{x}' \rangle \right\} dV_x + \mathbf{b}(\mathbf{x},t). \quad (29.1)$$

$$\rho \ddot{\mathbf{u}}_i^n = \sum_{q \in U_{\Omega_x}} \left\{ \underline{\mathbf{T}}[\mathbf{x}_i,t] \langle \mathbf{x}'_q - \mathbf{x}_i \rangle - \underline{\mathbf{T}}[\mathbf{x}'_q,t] \langle \mathbf{x}_i - \mathbf{x}'_q \rangle \right\} V_q + \mathbf{b}_i^n, \quad (29.2)$$

The force vector state $\underline{\mathbf{T}}[\mathbf{x},t]$ is interpreted in terms of mapping the bond between x and x' to a force density per volume which has a cutoff range. This leads to bond based PD model by defining $\underline{\mathbf{T}}[\mathbf{x},t] = \underline{t} \underline{\mathbf{M}}$. Here, \underline{t} is the force scalar state. This is related to the bond between two particles along the direction $\underline{\mathbf{M}}$:

$$\underline{\mathbf{M}}\langle \xi \rangle = \begin{cases} \frac{\xi + \eta}{\|\xi + \eta\|} & \forall \|\xi + \eta\| \neq 0 \\ 0 & \forall \text{ Otherwise} \end{cases}, \quad (30)$$

This generic PD model is specialized to classical linearly elastic isotropic material based on the MD based characterization of amorphous graphene epoxy systems. Hence the ‘‘Linear Peridynamic Solid’’ (LPS) model is used in this work. For LPS the scalar force state takes the following form [51]:

$$\underline{t} = \frac{3K\theta}{m} \underline{\omega x} + \alpha \underline{\omega e^d}, \quad (31.1)$$

$$\alpha = \frac{15G}{m}, \quad (31.2)$$

$$\underline{x}\langle \xi \rangle = \|\xi\|, \quad (31.3)$$

$$m[\mathbf{x}] = \int_{\Omega_x} \underline{\omega}\langle \xi \rangle \underline{x}\langle \xi \rangle \underline{x}\langle \xi \rangle dV_\xi, \quad (31.4)$$

$$\underline{e}[\mathbf{x}, t]\langle \xi \rangle = \|\xi + \eta\| - \|\xi\|, \quad (31.5)$$

$$\theta[\mathbf{x}, t] = \frac{3}{m[\mathbf{x}]} \int_{\Omega_x} \underline{\omega}\langle \xi \rangle \underline{x}\langle \xi \rangle \underline{e}[\mathbf{x}, t]\langle \xi \rangle dV_\xi, \quad (31.6)$$

$$\underline{e}^i = \frac{\theta x}{3}, \quad (31.7)$$

$$\underline{e}^d = e - \underline{e}^i, \quad (31.8)$$

where, K is the bulk modulus and G is the shear modulus. In the above equations $\underline{x}\langle \xi \rangle$ is the reference position, $m[\mathbf{x}]$ is the weighted volume, $\underline{e}[\mathbf{x}, t]$ is the extension scalar state, $\theta[\mathbf{x}, t]$ is the dilatation, and $\underline{e}^i, \underline{e}^d$ are the isotropic and deviatoric part of the extension scalar state $\underline{e}[\mathbf{x}, t]$.

The nonnegative scalar parameter $\underline{\omega}\langle \xi \rangle$ is the influence function which depends on $\|\xi\|$. For

isotropic case the influence function is $\underline{\omega}\langle \xi \rangle = \frac{1}{\|\xi\|}$.

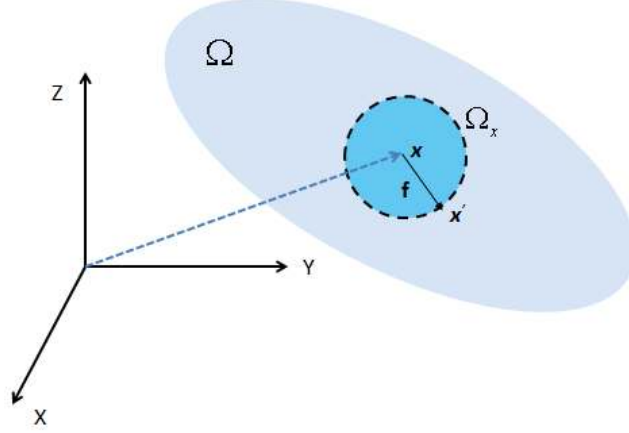


Figure 36. A schematic diagram of PD model

The Equation (27) needs to be deduced to a discrete form in order to be implemented. The problem domain is divided into particles constructing simple cubic lattice with lattice constant Δx . Each i^{th} particle has a volume fraction V_i which shares bond with a group of particles in the neighborhood region. Such a set associated with i^{th} particle is defined as $U_{\Omega_x} = \{q \mid \|x_q - x_i\| \leq \delta\}$. Besides the long range forces particles interact among themselves by short range force as well. Short range force is repulsive and defined by [51, 52]:

$$\mathbf{f}_S(\mathbf{u}_q, \mathbf{u}_i) = \min \left\{ 0, \frac{c_S}{\delta} (\|\mathbf{u}_q - \mathbf{u}_i\| - d_{qi}) \right\} \frac{\mathbf{u}_q - \mathbf{u}_i}{\|\mathbf{u}_q - \mathbf{u}_i\|}, \quad (32)$$

where, d_{qi} is short range interaction distance between q^{th} and i^{th} particle and $c_S = 15 \frac{18K}{\pi\delta^4}$ based on repulsive nature of short range force. The short range interaction distance is written as:

$$d_{qi} = \min \left\{ 0.9 \|\mathbf{x}_q - \mathbf{x}_i\|, 1.35 (r_q + r_i) \right\}, \quad (33)$$

where, r_q, r_i are the node radius of q^{th} and i^{th} particle respectively. Typically, for discrete lattice this is half of the lattice constant.

In PD model the long-range interaction represents bond between two particles. This generates the idea of bond breakage if the bond is stretched beyond a specific limit. The concept of bond breakage introduces fracture in PD model in a simplified fashion than in typical finite element model. The criteria for bond breaking is called “critical stretch criterion” in PD formulation. This is defined in terms of a scalar Boolean function μ :

$$\mu(t, \eta, \xi) = \begin{cases} 1 & \text{if } s(t', \eta, \xi) < \min(s_0(t', \eta, \xi), s_0(t', \eta', \xi')) \text{ for all } 0 \leq t' \leq t \\ 0 & \text{Otherwise} \end{cases}, \quad (34)$$

where, $s(t, \eta, \xi) = \frac{\|\eta + \xi\| - \|\xi\|}{\|\xi\|}$ is the bond stretch, $\xi' = x'' - x'$ and $\eta' = \mathbf{u}(x'', t) - \mathbf{u}(x', t)$. The

critical bond stretch is defined by:

$$s_0(t, \eta, \xi) = s_{00} - \alpha s_{\min}(t, \eta, \xi) \quad s_{\min}(t) = \min_{\xi} s(t, \eta, \xi), \quad (35)$$

where, s_{00}, α are material constants. The bond breaks when the bond stretches beyond s_0 . The above formulation of LPS is implemented by Parks and co-researchers [51, 52] in classical molecular dynamics code LAMMPS. During the simulation the velocities and positions are updated using velocity-Verlet scheme.

5.2 Hierarchical Multiscale Modeling

Peridynamics framework based hierarchical multiscale model (PFHMM) consists of several peridynamics (PD) models at different scales in order to establish a seamless hierarchical coupling with atomistic model. The coupling may be in both top-down and bottom-up directions. The methodology implied in PFHMM is explained in terms of an illustrative example with a 2D elastic plate problem as shown in Figure 37a.

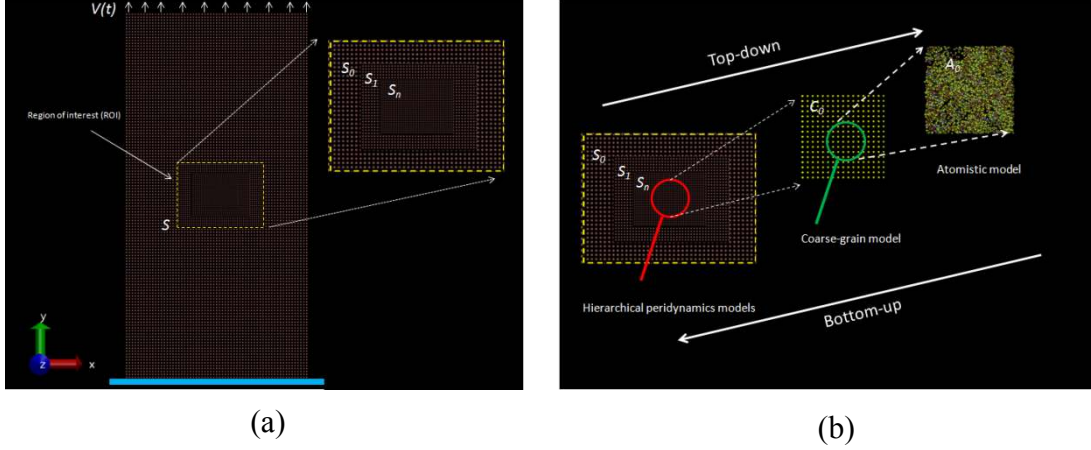


Figure 37: A schematic diagram of PFHMM

A velocity field $V(t)$ is applied at the free end of the plate in order to provide tensile deformation. The beam is constructed by peridynamic material points. An arbitrary region of interest is considered for the hierarchical multiscale coupling. Thus, a vector space, S may be defined which encapsulates all the position vectors of the particles in region of interest. The average pressure in the region of interest is calculated using the virial expression:

$$\langle P_M \rangle = \frac{1}{2A} \left(\sum_{i=1}^{M_S} r_i \cdot f_i \right), \quad (36)$$

Here, M_S is number of peridynamic particles in S , A is the area of the 2D region of interest (volume in 3D), r_i is the position vector of each particle and f_i is the force on each peridynamics particle from long-range and short-range interaction. It is to be noted that force in this case is calculated from the peridynamic equation of motion.

5.2.1 Top-down PFHMM

In top-down PFHMM, this pressure will be used as an applied pressure to the next hierarchical model. In Figure 37b and Figure 38 the top-down PFHMM is described in 2D and 3D schematic views. Mathematically, the space constructed by these peridynamic particles can

be written as $S_0 \supset S_1 \dots \supset S_n$. Here, n is the number of hierarchical levels of mutually independent peridynamics models. However, these mutually independent vector spaces are interlinked in terms of applied external pressure. Average internal pressure from the previous model works as boundary condition for the successive model. Particles in each model experience both short-range and long-range interaction with the system. Any model at n^{th} level may be imagined to be contained in a coarser model at $(n-1)^{\text{th}}$ level. Short and long range interactions from n^{th} level should influence the model as $(n-1)^{\text{th}}$ level. Hence, this is taken into consideration by applying average pressure $\langle P_{n-1} \rangle$ from $(n-1)^{\text{th}}$ level as an external pressure to n^{th} level model. The internal pressure in n^{th} model is calculated using the following virial formula

$$\langle P_n \rangle = \frac{1}{3V} \left(\sum_{i=1}^{M_{S_n}} r_i \cdot f_i \right), \quad (37)$$

Here, M_{S_n} is number of peridynamic particles in S_n , V is the volume of the unitcell, r_i is the position vector of each particle and f_i is the force on each peridynamics particle from long-range and short-range interaction.

An intermediate coarse-grain model C_0 is considered between hierarchical peridynamic models $S_0 \supset S_1 \dots \supset S_n$ and the atomistic model A_0 . Each atom in the atomistic model belongs to cross-linked epoxy molecule. Pcff forcefield [53] is used to define the interaction among atoms in the atomistic model A_0 . The intermediate coarse-grain model works as a handshake region between n^{th} peridynamics model and atomistic model. As shown in Figure 39, these coarse-grained atoms may be imagined as confining the real polymer molecules. Both coarse-grain

atoms and real atoms should ideally interact through van der waals force. It is to be noted that the average internal pressure (P_{CG}) in the coarse grain model is determined using the Lennard-Jones potential under the external applied pressure P_n . This pressure $\langle P_{CG} \rangle$ is used as an applied pressure on the atomistic model. At this stage, the goal is to study the respond of atomistic model due to the applied pressure under strain control. Every model in each level undergoes micro-canonical ensemble (NVE) based dynamics followed by isothermal-isobaric molecular dynamics (NPT) scale by using external pressure from coarser scale with a periodic boundary condition. The position and velocities of all the particles is updated using verlet algorithm.

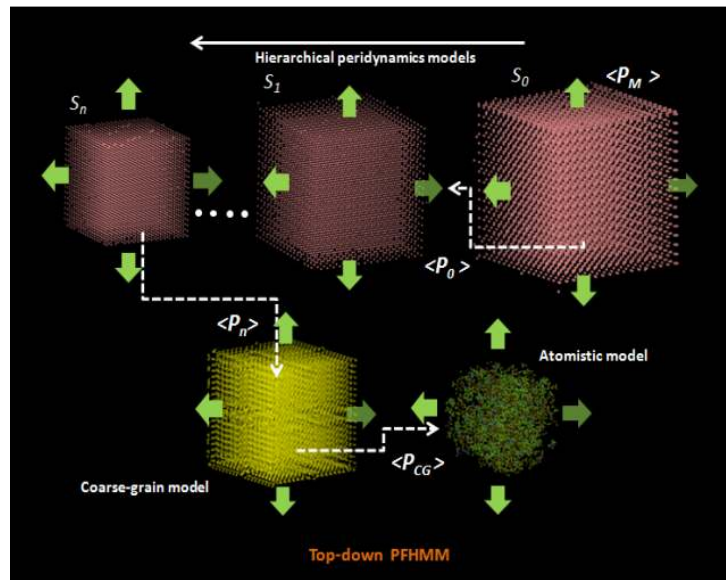


Figure 38. A schematic diagram for top-down PFHMM

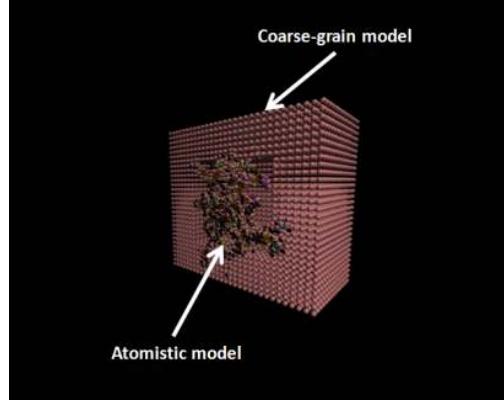


Figure 39. Coarse-grain model contains polymer molecules

5.2.2 Bottom-up PFHMM

Primary goal of this bottom-up model is to update the hierarchical models as shown in Figure 40 according to the change in atomistic model. It is clearly observable that transition from bottom to top scales requires a coarsening or averaging scheme. In order to pursue this idea, the atomistic model A_0 and the coarse-grain model C_0 are divided into $N_{C_0}^j$ and $N_{A_0}^j$ subcells (here $3 \times 3 \times 3$), respectively (Figure 40a). In each subcell the local centroid is calculated. Each of the centroid does not have any physical existence except position. These point objects are named as “Ghost atoms” as shown in Figure 40a. The purpose of these ghost atoms is to participate in a non-bonded interaction with other surrounding ghost atoms. The coordinates of these ghost atoms are written as follows

$$\bar{x}_{jk}^{-C_0} = \frac{\sum_{i=1}^{N_{C_0}^j} x_{ik}}{N_{C_0}^j} \quad \bar{x}_{jk}^{-A_0} = \frac{\sum_{i=1}^{N_{A_0}^j} x_{ik}}{N_{A_0}^j}, \quad (38)$$

In the above equations, $\bar{x}_{jk}^{-C_0}$ and $\bar{x}_{jk}^{-A_0}$ are the coordinates of ghost atom in j^{th} subcell of coarse-grain model C_0 and atomistic model A_0 , respectively, $N_{C_0}^j$ and $N_{A_0}^j$ are the number of

atoms in j^{th} subcell of coarse-grain model C_0 and atomistic model A_0 , respectively, $x_{ik} : k=1,2,3$ are the coordinates of the i^{th} atom in j^{th} subcell. Ghost atoms from C_0 , Gh_{C_0} and from A_0 , Gh_{A_0} are blended together while keeping their relative positions unchanged. These atoms are indistinguishable with respect to their source and lead to an interface model $AC_{\text{Interface}}$ between coarse-grain and atomistic models. Energy of the interaction between Gh_{C_0} and Gh_{A_0} is defined in terms of Lennard-Jones potential $V(r)$:

$$V(r) = 4\epsilon \left[\left(\frac{\sigma}{r} \right)^{12} - \left(\frac{\sigma}{r} \right)^6 \right], \quad (39)$$

where, $r = |\mathbf{r}_{lm}|$ the distance between l^{th} ghost atom in C_0 and m^{th} ghost atom in A_0 and ϵ is the depth of the potential wall and σ is the finite distance at which the interparticle potential is zero. This leads to interparticle force ${}^l \mathbf{f}_{ext}^{C_0}$ on l^{th} ghost atom in C_0 exerted by all the ghost atoms from A_0 :

$${}^l \mathbf{f}_{ext}^{C_0} = \sum_{m=1}^{NC_{A_0}} \mathbf{f}_{lm} \quad (40)$$

Where, $\mathbf{f}_{lm} = -\nabla V(r)$ is the force exerted on l^{th} ghost atom in C_0 by m^{th} ghost atom in A_0 . This applied force on each Gh_{C_0} is evenly distributed within the $N_{C_0}^l$ neighboring coarse-grain atoms in l^{th} subcell of coarse-grain model:

$${}^l_p \mathbf{f}_{ext}^{C_0} = \frac{{}^l \mathbf{f}_{ext}^{C_0}}{N_{C_0}^l} \quad (41)$$

Where, ${}^l \mathbf{f}_p^{C_0}$ is the applied external force on p^{th} coarse-grain atom in l^{th} subcell. In addition, external velocity boundary conditions are also applied to coarse grain atoms from previous peridynamics model. This is done by calculating average velocities of ghost atoms inherited from n^{th} peridynamics model S_n

$$\bar{\mathbf{v}}_j = \frac{\sum_{i=1}^{N_{S_n}^j} \mathbf{v}_i}{N_{S_n}^j} \quad {}^l \mathbf{v}_p^{C_0} = \frac{\sum_{j=1}^{NC_{S_n}} \psi(r) \bar{\mathbf{v}}_j}{N_{C_0}^l} \quad (42)$$

Where, $N_{S_n}^j$ is the number of peridynamic particles in j^{th} subcell, $\mathbf{v}_i = [v_{ix} \quad v_{iy} \quad v_{iz}]^T$ is the velocity vector of i^{th} particle, $\bar{\mathbf{v}}_j$ is the velocity vector of the ghost atom in j^{th} subcell, NC_{S_n} is the number of ghost atoms inherited from n^{th} peridynamics model S_n , $r = |\mathbf{r}_{lj}|$ the distance between l^{th} ghost atom in C_0 and j^{th} ghost atom in S_n , $\psi(r) = \frac{1}{\sqrt{\pi}h} e^{-\left(\frac{r}{h}\right)^2}$ is the interpolation function and $h = 30 \sim 80 \text{ \AA}$, ${}^l \mathbf{v}_p^{C_0}$ is the initial velocity assigned on any p^{th} atom by evenly distributing the velocity of each ghost atom Gh_{C_0} within the $N_{C_0}^l$ neighboring coarse-grain atoms in l^{th} subcell. This leads to define the equation of motion of any p^{th} coarse-grain atom

$$\begin{aligned} m_p \ddot{\mathbf{r}}_p &= \mathbf{f}_{int} + \mathbf{f}_{ext} \\ \mathbf{v}_0 &\equiv {}^l \mathbf{v}_p^{C_0} \\ \mathbf{f}_{ext} &\equiv {}^l \mathbf{f}_p^{C_0} \end{aligned} \quad (43)$$

Where, $m_p, \mathbf{r}_p, \ddot{\mathbf{r}}_p, \mathbf{f}_{int}, \mathbf{f}_{ext}, \mathbf{v}_0$ are mass, position vector, acceleration, internal force, external force and initial velocity of p^{th} coarse-grain atom respectively. The coarse-grain model

undergoes both NVE and NPT based MD equilibration by adjusting the volume of the periodic unitcell.

The external force on p^{th} ghost atom in PD model ${}^l \mathbf{f}_{ext}^{S_n}$ is applied by the coarse-grain ghost atoms using the similar manner as mentioned in Equations. (38-43). However, the velocity boundary conditions are not applied in this case. Using similar equations of motions as mentioned in Equation (43), the PD particles undergo NVE and NPT based MD equilibration. This leads to change the unitcell vectors. This is used to calculate the deformation gradient of the system. Let, n^{th} scale PD unitcell at has initial lattice vector $\mathbf{h}_0^{S_n} = [\mathbf{a}_0^{S_n} \quad \mathbf{b}_0^{S_n} \quad \mathbf{c}_0^{S_n}]^T$, where during the upscaling process the NPT based equilibration with zero external pressure changes the volume of the unitcell with atom positions. This leads to updated lattice vector $\mathbf{h}^{S_n} = [\mathbf{a}^{S_n} \quad \mathbf{b}^{S_n} \quad \mathbf{c}^{S_n}]^T$. Hence, the deformation gradient of this unitcell is $\mathbf{F}^{S_n} = (\mathbf{h}^{S_n}) \bullet (\mathbf{h}_0^{S_n})^{-1}$. This deformation gradient is applied to the next PD model. The core atoms in S_{n-1} are subjected to displacement guided by \mathbf{F}^{S_n} . Typically, the volume spanned by core atoms in S_{n-1} is same as the volume of S_n . Mathematically, if ${}_0 \mathbf{X}_{S_{n-1}}^{Core}$ refers to the vector space comprises of core atoms in S_{n-1} , the updated space ${}_1 \mathbf{X}_{S_{n-1}}^{Core}$ is obtained by ${}_1 \mathbf{X}_{S_{n-1}}^{Core} = \mathbf{F}^{S_n} \bullet {}_0 \mathbf{X}_{S_{n-1}}^{Core}$. The objective is to tie up the core region of S_{n-1} with S_n . The application of deformation gradient is followed by NVE and NPT based MD relaxation. During the NVE based MD relaxation, the atoms were restricted to small displacement in order to adjust the inter-atomic forces while conserving the prior deformation. Next, NPT based relaxation lead to adjust the volume of the unitcell with zero external pressure. The change in dimension of the unitcell leads to calculate the deformation gradient $\mathbf{F}^{S_{n-1}}$ which is applied to the next PD model. In this way the atoms in region of interest

S of the problem domain i.e. 2D beam, will experience a certain amount of displacement due to deformation gradient from pervious PD model. This is followed by NVE based relaxation. As a result the positions and forces in PD material points are updated for the next timestep $t_{M+1} = t_M + \Delta t$ with Δt increment. The overall picture of bottom-up PFHMM is given in Figures 40a and 40b.

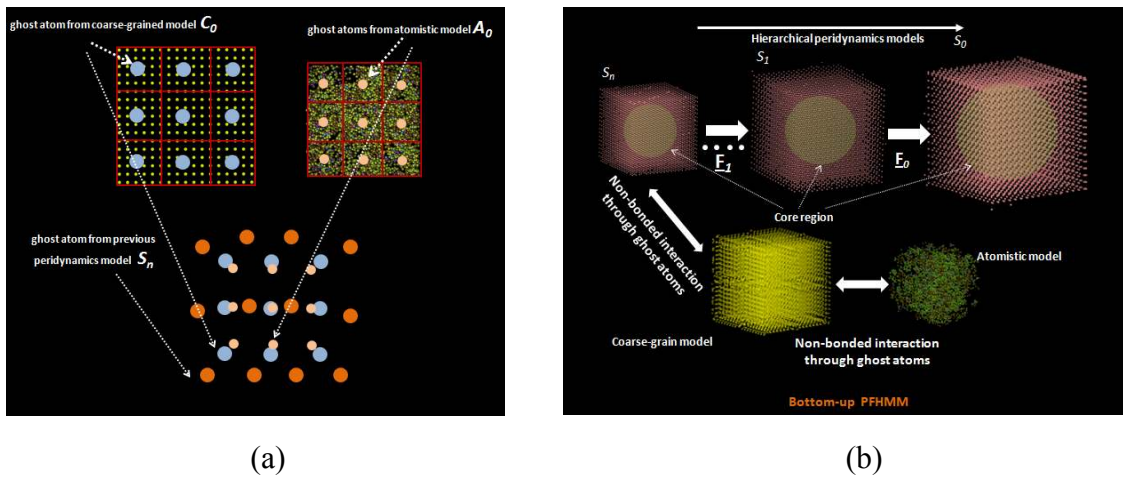


Figure 40. A schematic diagram for bottom-up PFHMM

Combining top-down and bottom-up PFHMM establishes a closed loop system for multiscale modeling as shown in Figure 41.

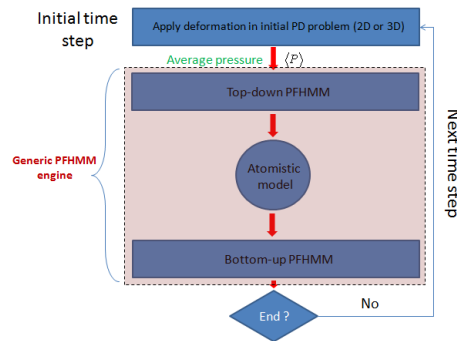


Figure 41: A schematic diagram closed loop PFHMM

5.3 Numerical Experiments and Results

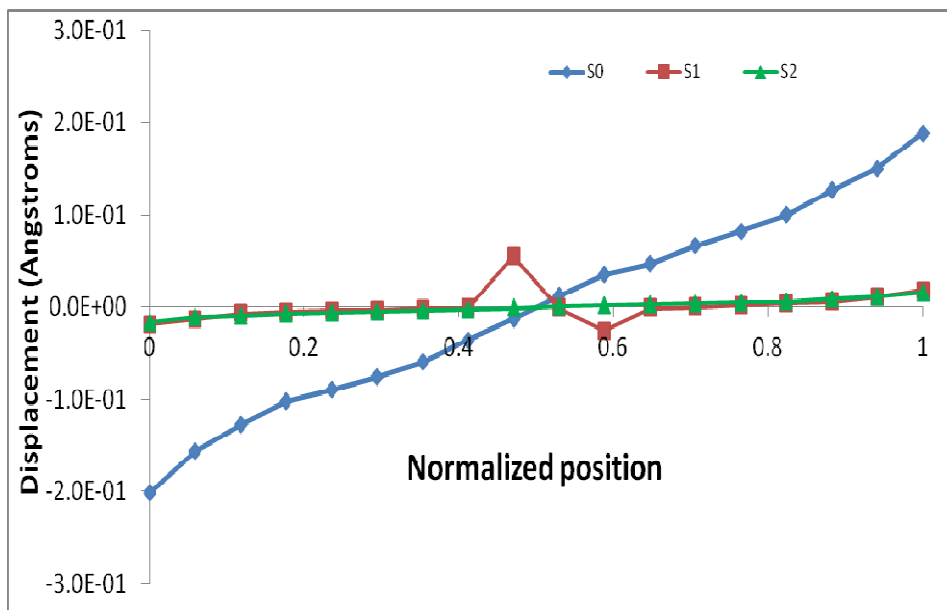
5.3.1 Two Dimensional (2D) Plate under Axial Load

A 2D plate under axial load is considered as problem domain (Figure 37a). The length and width of the plate is taken as 10000 \AA^0 and 5000 \AA^0 , respectively. The region of interest is defined by $S = \{(x, y) | 1500 \text{ \AA}^0 \leq x \leq 3500 \text{ \AA}^0, 3000 \text{ \AA}^0 \leq y \leq 7000 \text{ \AA}^0\}$. The plate consists of 7938 PD particles. The material was Epon 862 epoxy with bulk modulus $K=3.43 \text{ GPa}$, shear modulus $G = 1.22 \text{ GPa}$ and horizontal cutoff range $\delta = 400 \text{ \AA}^0$. The plate was fixed at one end while a velocity field $V(t) = 0.1 \frac{\text{\AA}^0}{\text{fs}}$ was applied at the free end in Y-direction for 100 steps. The positions of PD particles in 2D plate were updated under NVE ensemble. The plate was deformed by 0.01% in loading direction and developed an average internal pressure $P_m = 25 \text{ atm}$. Based on top-down PFHMM, P_m was used as an applied pressure to the next PD model, $S_0 = \{(x, y, z) | 0 \leq x \leq 500 \text{ \AA}^0, 0 \leq y \leq 500 \text{ \AA}^0, 0 \leq z \leq 500 \text{ \AA}^0\}$ which was a cubic lattice consisting of 5832 PD particles of Epon 862. The horizontal cutoff range was $\delta = 90 \text{ \AA}^0$. PD particles in S_0 is equilibrated under NVE ensemble for 5000 steps followed by 500 steps MD run under NPT ensemble while applying 25 atm external pressure. The temperature is scaled to 0.01K during the whole MD simulation. This leads to 0.08% deformation of the PD unit cell in all directions. The average developed pressure in S_0 was 16.23 atm. This developed pressure $\langle P_{S_0} \rangle = 16.23 \text{ atm}$ was applied to the next finer scale PD model, $S_1 = \{(x, y, z) | 0 \leq x \leq 300 \text{ \AA}^0, 0 \leq y \leq 300 \text{ \AA}^0, 0 \leq z \leq 300 \text{ \AA}^0\}$ with horizontal cutoff range $\delta = 54 \text{ \AA}^0$. The unit cell S_1 was expanded by 0.015% in all directions developing an internal

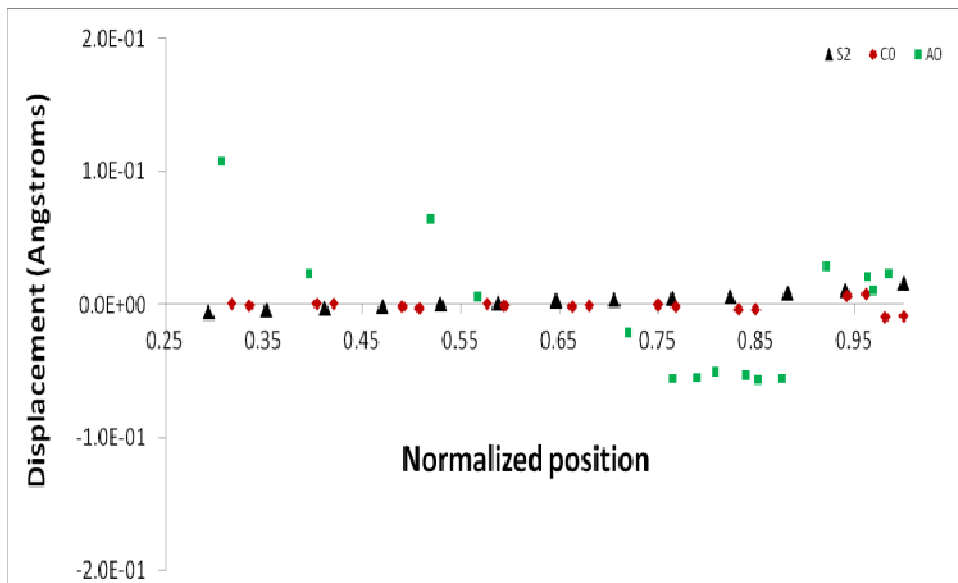
pressure $\langle P_{S_1} \rangle = 13.00$ atm. Using the same number of steps under NVE and NPT ensemble, the unit cell of S_1 is deformed by 0.015%. A further smaller PD model with 5832 particles was defined by $S_2 = \{(x, y, z) | 0 \leq x \leq 200 \text{ \AA}^0, 0 \leq y \leq 200 \text{ \AA}^0, 0 \leq z \leq 200 \text{ \AA}^0\}$ with horizontal cutoff radius $\delta = 40 \text{ \AA}^0$. In a similar manner, the unitcell was deformed by 0.0187% under external pressure $\langle P_{S_1} \rangle = 13.00$ atm from S_1 . This developed average internal pressure $\langle P_{S_2} \rangle = 92.31$ atm which was implied as applied pressure for next coarse-grain MD model C_0 . The reason behind increased pressure in smaller PD model is the increment of atoms in each atom's neighborhood list. $C_0 = \{(x, y, z) | 0 \leq x \leq 50 \text{ \AA}^0, 0 \leq y \leq 50 \text{ \AA}^0, 0 \leq z \leq 50 \text{ \AA}^0\}$ was a cubic lattice with 15625 atoms. The interaction among atoms was defined in terms of Lennard-Jones potential with $\epsilon = 0.5$ Kcal/mole, $\sigma = 1.0 \text{ \AA}^0$ and cutoff distance $r_c = 8.0 \text{ \AA}^0$. The model undergoes 5000 steps under NVE followed by 1000 steps under NPT ensemble. The coarse-grain model works as a handshake model between PD and atomistic model. C_0 had higher atom resolution than the PD models. The developed average pressure in CG model was $\langle P_{CG} \rangle = 38.60$ atm which was considered to be the applied pressure for the atomistic model A_0 . This is the final stage of top-down PFHMM. The coordinates of $A_0 = \{(x, y, z) | 0 \leq x \leq 44.37 \text{ \AA}^0, 0 \leq y \leq 44.37 \text{ \AA}^0, 0 \leq z \leq 44.37 \text{ \AA}^0\}$. It is an amorphous model of epoxy consisting of 5338 atoms. The atomistic model is subjected to 5000 steps of MD runs under NPT ensemble with the external pressure 38.60 atm. from CG model. After MD runs, the average pressure in the atomistic model is seen to be 37.03 atm and the unitcell is observed to deform by 0.92%. Figure 42a provides displacement profiles in the hierarchical peridynamic regions S_0 , S_1 and S_2 . It is to be noted that the positions of peridynamics points in each region are

normalized with the corresponding coordinates of the points at the boundary. In Figure 42a displacement profile of peridynamic points is shown only in x-direction passing through the centroid for cubic spaces S_0 , S_1 and S_2 . The displacement profiles of peridynamic points in y and z coordinate system are also seen to follow similar pattern. The results show comparatively higher displacement in S_0 region compared to S_1 and S_2 region due to corresponding strains 0.08%, 0.015% and 0.0187%, respectively. The PD particles near boundary show comparatively larger displacement than the particles around center point. The displacement is seen to be almost zero at the center point in all three scales. The displacement profiles are also seen to be inversely symmetric about the center point in all the scales. This inverse nature in the displacement profile is due to chosen coordinate system. The displacement profiles for S_1 and S_2 regions are seen almost similar due to close resembles in their size. Figure 42b shows the displacement profiles in the hierarchical peridynamic (S_2), coarse grain (C_0) and atomistic (A_0) regions. In Figure 42b, the positions of the peridynamics points in S_2 , coarse grain points in C_0 and atoms in A_0 are also normalized with the corresponding locations at the boundary i.e. $x = 200 \text{ \AA}^0$, 50 \AA^0 and 44.37 \AA^0 . The displacement profiles, u_x shown in Figure 42b correspond to peridynamics points and coarse grain atoms lie in x-axis which passes through the centroid of the unit cell. It is to be noted that the atomic model (A_0) consists of amorphous epoxy molecules. As a result atoms may not lie exactly on x-axis which passes through the center of the unit cell. On that basis the atoms in A_0 region were selected from the close neighborhood of x-coordinate which pass through center and the corresponding displacement, u_x of those atoms are shown in Figure 42b. The displacements of atoms in A_0 showed comparatively larger variance than PD models. This could be due to the effect of thermal noise at the atomistic scale and the amorphous nature of the polymer. Hence,

the displacements from the atomistic model were observed to be scattered around the displacements from C_0 and S_2 though the variation was not significantly large.



(a)



(b)

Figure 42: Displacement vs. position at different scales

In addition to the above analysis, the displacement field can be studied at different scales. For successful multiscale coupling it is important to obtain better correlation among displacements field from each scale. According to Figure 43, displacement fields at different scales are shown. The displacement fields are denoted with $u_{S_0}, u_{S_1}, u_{S_2}, u_{C_0}$ and u_{A_0} for PD models (S_0, S_1, S_2), coarse-grain model C_0 and the atomistic model A_0 respectively. For an example, u_{S_0} corresponds to the set of displacements of all PD particles in S_0 . Considering

displacement of i^{th} PD particle in S_0 as $u_{S_0}^i$, $u_{S_0} = \bigcup_i u_{S_0}^i$. Here,

$$u_{S_0}^i = \begin{matrix} \text{Initial} \\ \left[\begin{matrix} x \\ y \\ z \end{matrix} \right]_{S_0}^i \end{matrix} - \begin{matrix} \text{Final} \\ \left[\begin{matrix} x \\ y \\ z \end{matrix} \right]_{S_0}^i \end{matrix}. \text{ In this illustration the displacements are considered on XY-}$$

plane ($z=0$). However, these are similar in XZ and YZ planes. In Figure 43a, the displacements in S_0 and S_1 are addresses to be varying within the interval $[-0.25 \text{ \AA}^0, 0.25 \text{ \AA}^0]$. It is clearly observed that the displacement field of S_1 is contained in the displacement field of S_0 .

Mathematically, this variation can be expressed as $\|u_{S_0} - u_{S_1}\| < u_M$. Here, u_M is a number sufficiently less than 0.5 \AA^0 . Similar observation is made in Figure 43b. The displacement fields of S_1 and S_2 vary within the range of $\pm 0.08 \text{ \AA}^0$. Based on these three models the bounded variation can be rewritten as $\|u_{S_0} - u_{S_1}\| + \|u_{S_1} - u_{S_2}\| < u_M$. The displacements at coarse-grain and atomistic scales exhibit slightly different behavior. According to Figure 43c, though most of the atoms in CG model have displacements varying within the range $[-0.02 \text{ \AA}^0, 0.02 \text{ \AA}^0]$, few atoms exhibit scattered displacements compared to the displacement field in S_2 . This discrepancy

occurs may be due to the difference in formulation between continuum model (governed by non-local integro-differential equation) and the coarse-grained model (governed by Lennard-Jones interaction). Similar observation is made in Figure 43d. In this case the displacement fields are from C_0 (coarser scale) and A_0 (finer scale). The displacement fields in C_0 and A_0 are well correlated within the range $[-0.05 \text{ \AA}^0, 0.05 \text{ \AA}^0]$. Outside of this range displacement field in atomistic model gradually deviated from the one in coarse-grain model. This is expected as $u_{\text{Finer}} = u_{\text{Coarser}} + \text{Noise}$. It is evident that the displacement fields in all the scales have mutual correlation. This indicates that top-down PFHMM is able to establish coupling among all the scales appropriately.

The bottom-up PFHMM is also an important component of this multiscale modeling scheme. The objective is to evaluate deformation behavior in continuum region based on change in atomistic scale. Using the bottom-up methodologies explained in previous section the coarse-grain model C_0 was considered as starting point. The parameters for Lennard-Jones potential are $\epsilon=0.1 \text{ Kcal/mole}$, $\sigma=80.0 \text{ \AA}^0$. In the top-down PFHMM, the total energy in coarse-grain model is seen to be -21960 kcal/mole after deformation. But in bottom-up PFHMM scheme, the total energy is seen to be $-22450.245 \text{ kcal/mole}$ after distributing force from ghost atoms and equilibrating the model for 5000 steps under NVE and NPT conditions, respectively. This shows very insignificant change in CG model after being updated by bottom-up scheme. Furthermore, PD models S_2 , S_1 and S_0 were updated according to bottom-up PFHMM scheme. Total energies of these PD models were not changed significantly. During top-down coupling, the total energies of S_2 , S_1 and S_0 were 6.12 Kcal/mole , 4.76 Kcal/mole and 136.70 Kcal/mole , respectively. These were changed to 12.52 Kcal/mole , 4.63 Kcal/mole and 129.64 Kcal/mole , respectively.

after MD simulation using bottom-up scheme. Each atom on region of interest S of the 2D plate was displaced by 0.17 \AA in x, y directions while bottom-up PPFHMM was implied. It is to be noted in top-down scheme this deformation was 0.2 \AA . This illustrates that coupling ability of PPFHMM among different scales are effective using both top-down and bottom-up scheme.

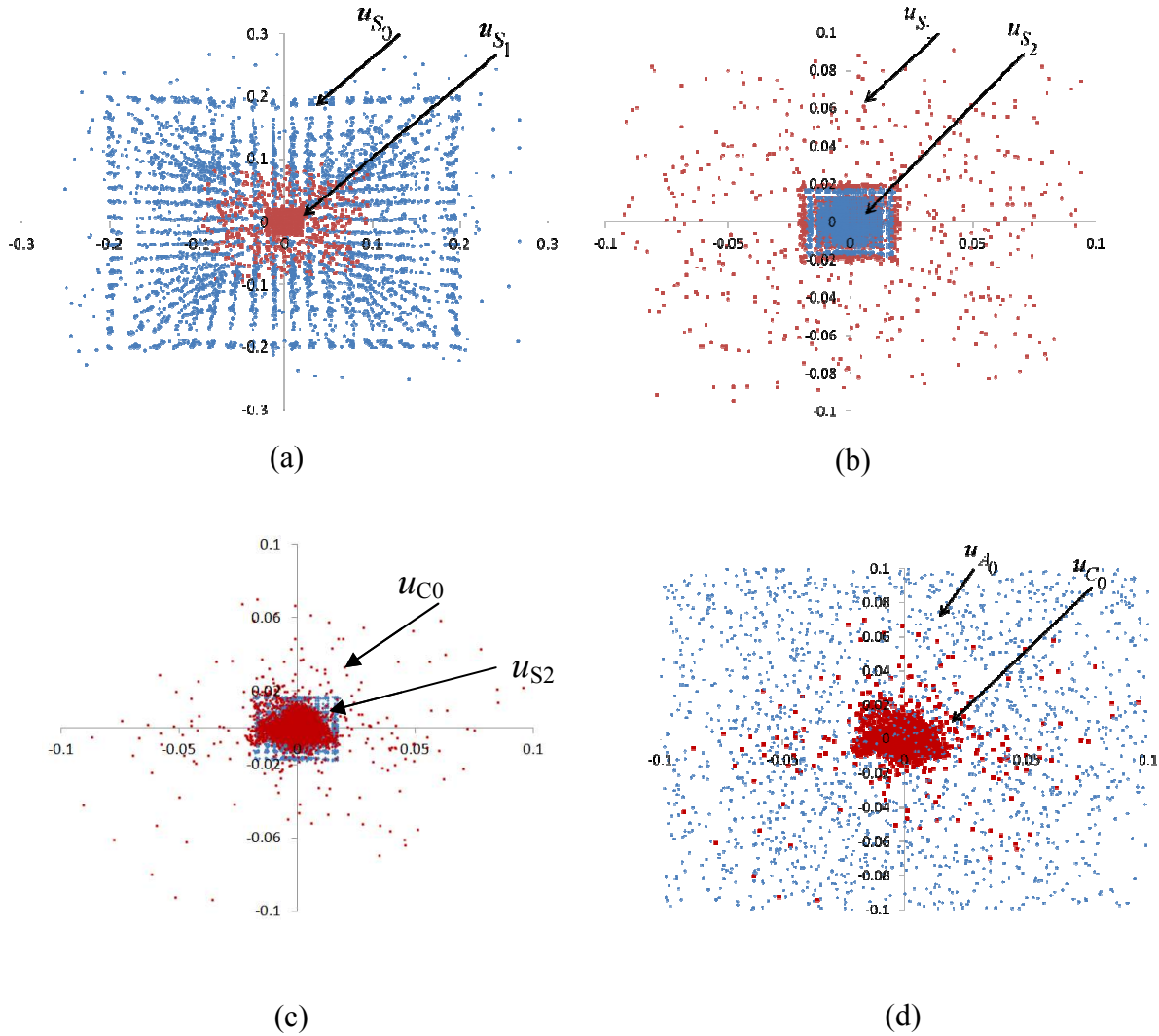


Figure 43. Displacement fields at different scales

5.3.2 Two Dimensional Plate with an Edge Crack

In this illustration a 2D plate with an edge crack was considered. The plate consists of 7912 PD particles of 3% graphene reinforced epoxy with bulk modulus $K=3.98 \text{ GPa}$, shear

modulus $G = 1.37$ GPa and horizontal cutoff range $\delta = 400 \text{ \AA}$. As shown in Figure 44a the number of hierarchical levels considered in this case was comparatively less (S , S_0 , C_0 , and A_0) than the previous case. In Figure 44a, the dimension of the 2D plate and region of interest S was kept same as section 4.3.2.1. The edge crack length and width were 1000\AA and 100\AA , respectively. The plate was fixed at one end while a velocity field $V(t) = 0.1 \frac{\text{\AA}}{\text{fs}}$ was applied at the free end in Y-direction for 500 steps. In all the cases crack lengths were to one fifth of the unit cell length. The crack widths were 90 \AA in S_0 , 20 \AA in C_0 and 16 \AA in A_0 in order to capture the crack opening distance. The hierarchical models S_0 , C_0 and A_0 are setup in such a way that the crack tip displacements at different scales can be captured.

This resulted 0.432% deformation in 2D plate and average internal pressure $\langle P_M \rangle = 960.15$ atm in the region S . It is to be noted that the region S lies in the neighborhood of the crack tip. Based on top-down PFHMM scheme, this was applied as an external pressure to the next PD model $S_0 = \{(x, y, z) | 0 \leq x \leq 500 \text{ \AA}, 0 \leq y \leq 500 \text{ \AA}, 0 \leq z \leq 500 \text{ \AA}\}$. It was a cubic lattice consisting of 4777 PD particles with cutoff range $\delta = 100 \text{ \AA}$. The PD particles possess similar mechanical properties as the ones in 2D model. Particles in S_0 were subjected to 5000 steps under NVE followed by 500 steps under NPT with an external pressure of 960.15 atm. This resulted 6.58% deformation in S_0 and an average internal pressure $\langle P_{S_0} \rangle = 1955.06$ atm. The developed pressure $\langle P_{S_0} \rangle = 1955.06$ atm is applied to the coarse-grain model $C_0 = \{(x, y, z) | 0 \leq x \leq 80 \text{ \AA}, 0 \leq y \leq 80 \text{ \AA}, 0 \leq z \leq 80 \text{ \AA}\}$. It was a cubic lattice with 59320 atoms. The interaction among atoms was defined in terms of Lennard-Jones potential with

$\varepsilon=0.5$ Kcal/mole, $\sigma=1.0 \text{ \AA}^0$ and cutoff distance $r_c = 8.0 \text{ \AA}^0$. The coarse-grain atoms were equilibrated under NVE for 5000 time steps and then 4000 steps under NPT with an external pressure $\langle P_{S_0} \rangle = 1955.06 \text{ atm}$. This resulted 27.31% deformation and $\langle P_{CG} \rangle = 441.30 \text{ atm}$ in CG model. This pressure was applied to the next atomistic model $A_0 = \{(x, y, z) | 0 \leq x \leq 45.93 \text{ \AA}^0, 0 \leq y \leq 45.93 \text{ \AA}^0, 0 \leq z \leq 45.93 \text{ \AA}^0\}$ with 9003 atoms. The atomistic model was subjected to 10000 steps of MD run under NPT ensemble. This resulted 16.0% deformation in A_0 and eventually leads to crack opening. At this stage the top-down PFHMM ends and bottom-up PFHMM starts. As discussed before, each model at different scales will be updated based on bottom-up PFHMM scheme. After the end of top-down PFHMM, the coupling between problem domain (S) and atomistic model (A_0) was reflected on the movement of crack tip in the atomistic model.

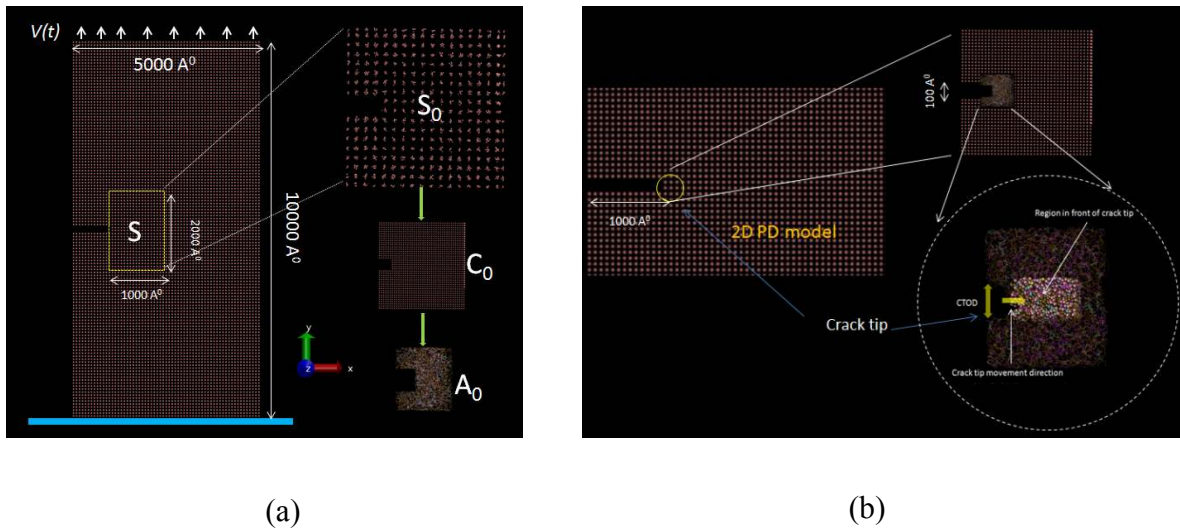


Figure 44: Illustration of 2D crack problem using PFHMM

The crack opening displacement (COD) and crack tip movement was captured from every scale in PFHMM. The COD data was captured from the deformed atoms/particles located slightly inside the crack. In Figures 44 (b) the crack opening is shown. As mentioned before, the

initial crack widths were $\zeta_{S_0} = 90 \text{ \AA}^0$ in S_0 , $\zeta_{C_0} = 20 \text{ \AA}^0$ in C_0 and $\zeta_{A_0} = 16 \text{ \AA}^0$. The CODs in Figure 45 shows the increments ($\Delta\zeta$) of the crack widths with respect to time. In the 2D plate the COD is 80 \AA^0 in 500 steps with initial crack width of 100 \AA^0 . It is clearly observed that COD is the highest in S_0 ($0.0 - 7.0 \text{ \AA}^0$) while the lowest in atomistic model A_0 ($0.0 - 1.2 \text{ \AA}^0$). The COD at atomistic scale less smooth compared to other coarser scales. It is also noticed that the rate of crack opening displacement gradually increases with time in S_0 and C_0 . In A_0 the rate of COD increases in first 20% of total time (1000 femtoseconds) then starts decreasing. It is to be noted that bond breakage was not considered initially. The goal of introducing bond breakage is to gain an insight on predicting crack growth at atomistic scale. During deformation, the average pairwise chemical bond length between atoms changes depending on strain rate, temperature, total energy, external pressure on the system etc. If any certain bond length between two atoms exceeds a predefined critical bond length, that bond is considered to be broken. This introduces damage in the material. In this case the COD is obtained at atomistic scale using PFHMM. The critical bond length is chosen to be 2.0 \AA^0 as it is observed that average bond length increases from 1.2 \AA^0 to 1.4 \AA^0 during deformation. Bond breakage is applied only in the region in front of crack tip at atomistic scale in order to capture its effect on COD. In Figure 45c it is observed that COD increases when bond breakage criteria is incorporated. Using the same boundary condition and MD runs, the maximum COD without bond breakage is seen to be less than 0.3 \AA^0 whereas considering bond breakage this becomes almost 1.0 \AA^0 . Hence, crack opens in a rapid manner if pairwise bonds break in front of crack tip. Prior to bond breakage there were 9420 bonds in A_0 . This reduced to 9021 bonds after applying bond breaking criterion.

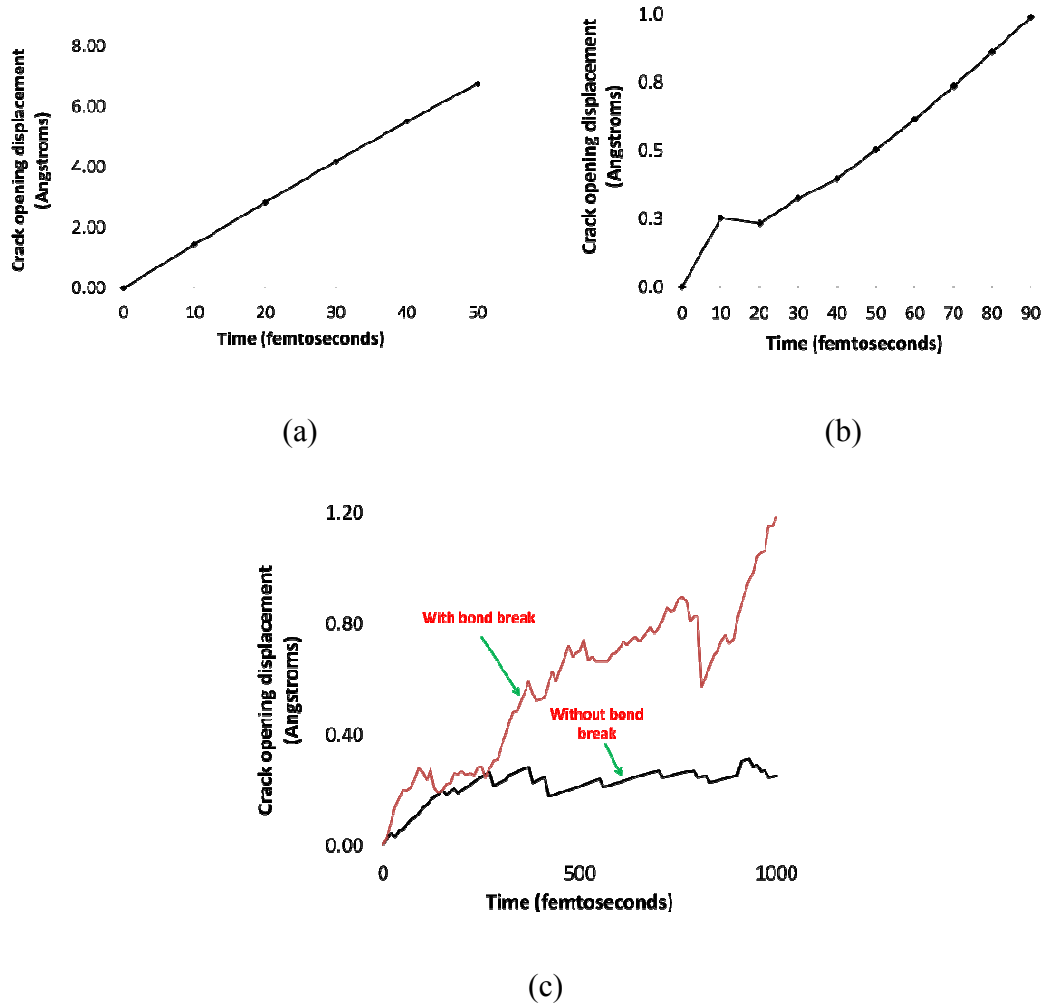


Figure 45 (a) Crack opening displacement vs. time in peridynamic model S_0 (b) Crack opening displacement vs. time in coarse-grain model C_0 and (c) Crack opening displacement vs. time in atomistic model A_0

The initial crack length was a is 20 \AA . The crack tip displacement can be interpreted as Δa . The result show almost linear movement of crack tip with time. Crack tip moves approximately 0.015 \AA in 1000 femtoseconds. The average crack tip movement in the 2D peridynamics model was seen to be 0.01 \AA in 50 femtoseconds. Bond breakage was not considered while evaluating crack tip displacement.

5.3.3 Three dimensional nanoindentation problem

The next demonstration of PFHMM considers a three dimensional nanoindentation problem. A 3D cubic unitcell with dimension: $2000 \text{ \AA} \times 2000 \text{ \AA} \times 2000 \text{ \AA}$ consisting of 74898 PD neat epoxy particles with bulk modulus $K=3.43 \text{ GPa}$, shear modulus $G = 1.22 \text{ GPa}$ and horizontal cutoff range $\delta = 100 \text{ \AA}$ was considered as problem domain. The objective is to apply indentation force at the center of the top surface along XY direction and keep the bottom surface fixed. PD particles are highly dense in the central region $S = \{(x, y, z) | 500 \leq x \leq 1500, 500 \leq y \leq 1500, 0 \leq z \leq 2000\}$ in order to capture atom displacement due to indentation. A spherical rigid indenter with 500 \AA diameter was used with 10 \AA per femtoseconds downward velocity. During nanoindentation process the PD particles were subjected to 2000 steps of NVE based dynamics. The location of indentation was at $(1000 \text{ \AA}, 1000 \text{ \AA}, 2000 \text{ \AA})$. Average pressure developed in S was $\langle P_S \rangle = 19.57 \text{ atm}$ which was used as an external compressive pressure for the next PD model S_0 . There were four epoxy PD models S_0, S_1, S_2 and S_3 in top-down PFHMM (section 5.2.1). These were cubic lattices with dimensions of $800 \times 800 \times 800 \text{ \AA}^3$, $480 \times 480 \times 480 \text{ \AA}^3$, $320 \times 320 \times 320 \text{ \AA}^3$ and $200 \times 200 \times 200 \text{ \AA}^3$, respectively. The cutoff distances for PD particles in S_0, S_1, S_2 and S_3 were $145.5 \text{ \AA}, 87.3 \text{ \AA}, 58.2 \text{ \AA}$ and 36.4 \AA , respectively. These PD models will experience compressive deformation during top-down PFHMM. After 5000 steps of NVE based relaxation, S_0 was deformed by 0.06% under external pressure $\langle P_{S_0} \rangle = 19.57 \text{ atm}$ from S followed by updating the positions and velocities of PD particles for 12000 steps under NVE. The developed pressure $\langle P_{S_0} \rangle = 7.60 \text{ atm}$ was applied as external pressure to the next PD model S_1 . This lead to 0.023% deformation of S_1

preceded by 5000 steps of NVE based equilibration. Afterwards the positions and velocities of the PD particles were updated for 2000 steps. Next, S_2 was deformed by 0.02% due to external pressure $\langle P_{S_1} \rangle = 6.978$ atm from previous PD model S_1 . Similarly, the PD particles were firstly equilibrated for 5000 steps then 2000 steps under NVE ensemble. This lead to develop average pressure $\langle P_{S_2} \rangle = 25.65$ atm in S_2 which was applied on S_3 and leads to 0.03% deformation of S_3 . Next, the average pressure pressure $\langle P_{S_3} \rangle = 143.48$ atm in S_3 worked as external pressure for the coarse-grain model $C_0 = \{(x, y, z) | 0 \leq x \leq 50 \text{ A}^0, 0 \leq y \leq 50 \text{ A}^0, 0 \leq z \leq 50 \text{ A}^0\}$. The interaction among 15625 atoms was defined in terms of Lennard-Jones potential with $\epsilon=0.5$ Kcal/mole, $\sigma=1.0 \text{ A}^0$ and cutoff distance $r_c = 8.0 \text{ A}^0$. As the PD model scales down from 800 A^0 to 200 A^0 , the average particle density in the neighborhood of each PD particle increased by 30%. This caused higher pressure in S_3 . The coarse-grain atoms in C_0 underwent NVE based equilibration for 5000 steps prior to 0.83% deformation. The average pressure developed in C_0 was $\langle P_{CG} \rangle = 138.499$ atm. This was applied to the atomistic model $A_0 = \{(x, y, z) | 0 \leq x \leq 45.93 \text{ A}^0, 0 \leq y \leq 45.93 \text{ A}^0, 0 \leq z \leq 45.93 \text{ A}^0\}$ with 9003 atoms. The atomistic model was subjected to 5000 steps of MD run under NPT ensemble. This lead to 1.6% deformation of the atomistic model with 139.19 atm average pressure. This ends the top-down PFHMM and starts bottom-up PFHMM using the formulations discussed in section 5.2.2. The schematic diagram of this demonstration is given in Figure 46.

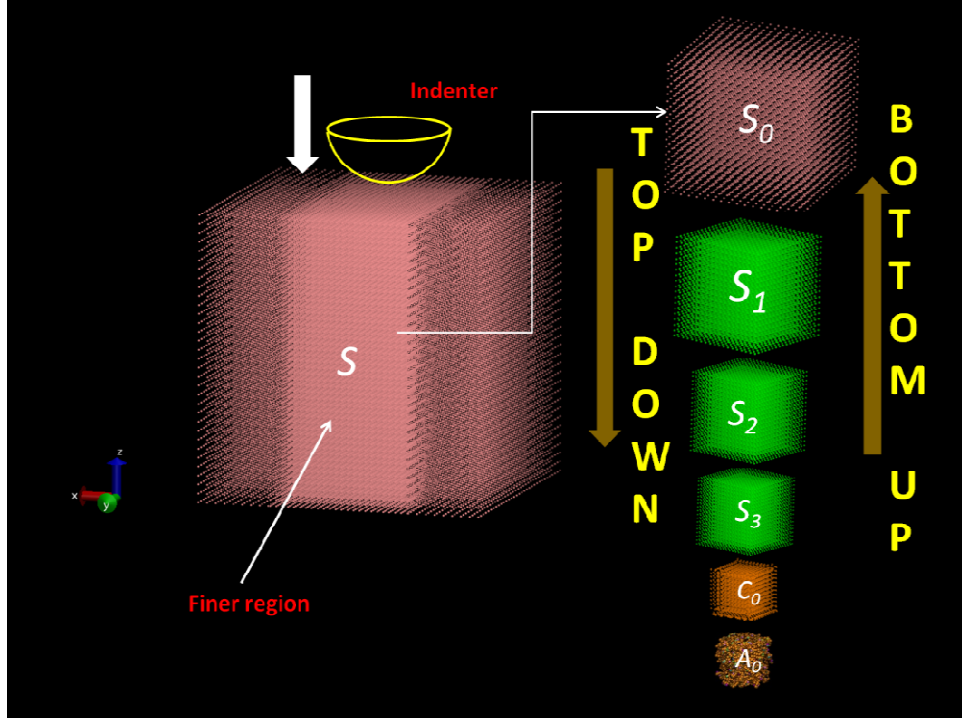


Figure 46. Schematic diagram of PFHMM of a nanoindentation problem

Similar to previous discussion in section 5.2.3.3, the displacement fields in different scales are shown in Figure 47. These displacement fields are obtained from YZ-plane. According to Figure 47a, the displacement fields in S (20% of central region) and S_0 are shown. It is noticed that there is slight deviation between u_S and u_{S_0} .

But the displacement field from S_0 is bounded by the displacement field from S . Hence it is possible to write $\|u_{S_0} - u_S\| < u_M$, where

u_M is less than $2 A^0$. Next, the displacement fields from different PD models are shown in Figure 47b. It is evident that the displacements at different scales have good correlation.

Mathematically, this can be expressed as $\|u_{S_1} - u_{S_0}\| + \|u_{S_2} - u_{S_1}\| + \|u_{S_3} - u_{S_2}\| < u_M$. This

correlation hold better in the core regions of the displacement fields i.e. within the range of

$\pm 0.05 A^0$ from center. In a similar manner the displacement fields between S_3 , C_0 and A_0 are

compared in Figure 47c. The displacement fields in C_0 and A_0 are obtained from the atoms which reside within 80% from the center of the unitcell. Within range of $\pm 0.1 \text{ \AA}$, u_{S_3} , u_{C_0} and u_{A_0} have better correlation. The atoms from in C_0 and A_0 seem to have comparatively larger displacement than S_3 . These well correlated displacements ensure that PFHMM is able to establish coupling among different scales seamlessly. This can be observed in Figure 47d.

It is important to address the total energy evolution during top-down and bottom-up PFHMM. The energy in each model is expected to have consistency in both ways. Prior to entering the bottom-up PFHMM, the total energy of C_0 was 20522.348 kcal/mole. This became 20980.473 kcal/mole after the bottom-up scheme. The parameters for Lennard-Jones potential are $\epsilon=0.001 \text{ Kcal/mole}$, $\sigma=100.0 \text{ \AA}$ in order to define non-bonded interaction among the ghost atoms. The total energies of S_3 , S_2 , S_1 and S_0 were 152.97 kcal/mole, 11.38 kcal/mole, 11.81 kcal/mole and 73.14 kcal/mole, respectively after top-down PFHMM. At the end of bottom-up scheme the total energies of S_3 , S_2 , S_1 and S_0 are seen to be 163.06 kcal/mole, 8.5 kcal/mole, 5.43 kcal/mole and 65 kcal/mole, respectively. This indicates that the energies are not significantly changed. Thus it completes a single loop of PFHMM.

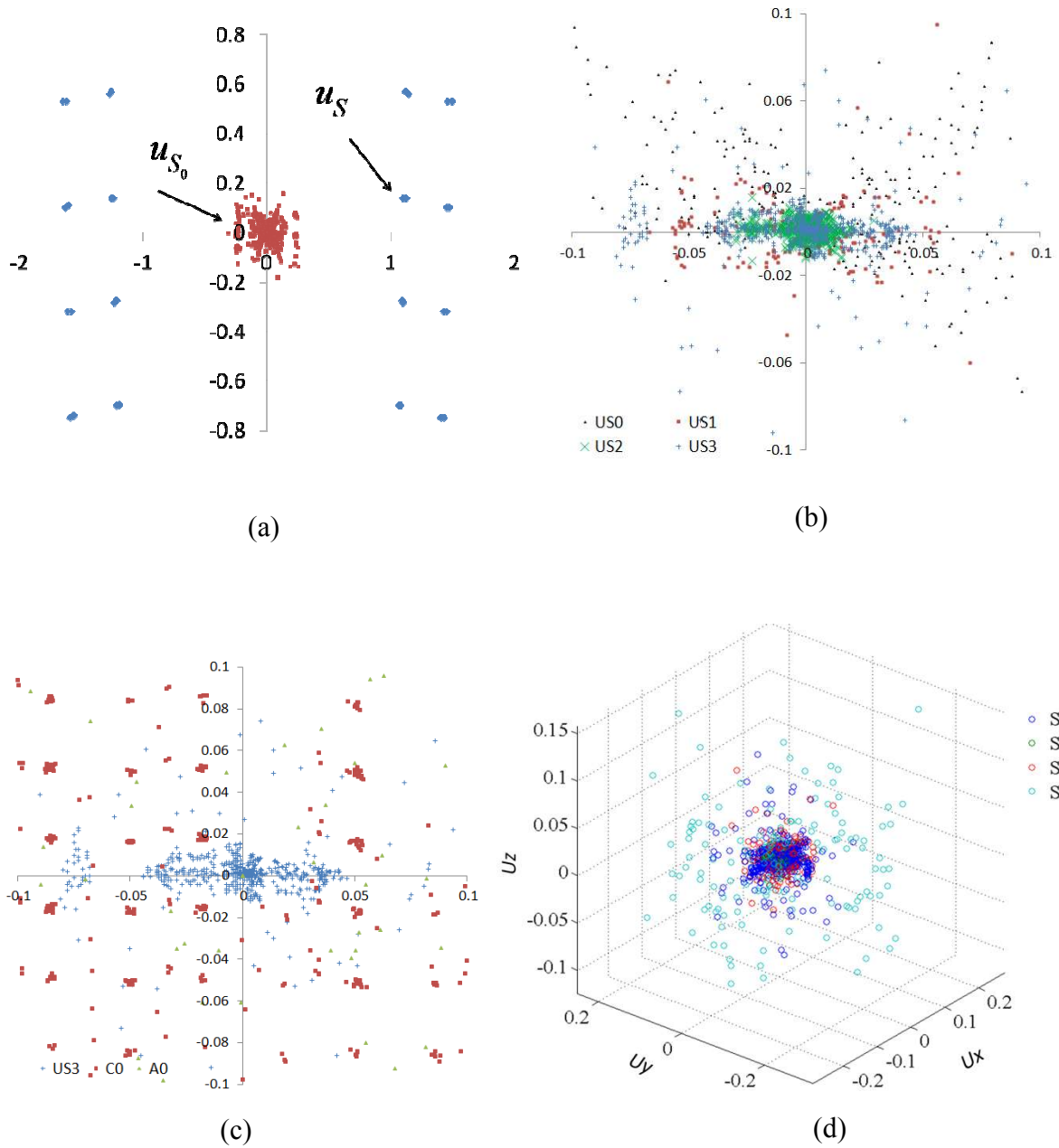


Figure 47. (a) Displacement fields in S and S_0 on YZ plane (b) Displacement fields in S_0 , S_1 , S_2 and S_3 on YZ plane (c) Displacement fields in S_3 , C_0 and A_0 on YZ plane (d) 3D Displacement fields in S_0 , S_1 , S_2 and S_3

5.4 Benchmark analysis between FEA, PD and MD

5.4.1 Case-I

In this case, the benchmarking was carried out on 2D graphene models at the atomistic scale. A 2D graphene sheet bar (length= 40 \AA , width= 20 \AA) under uniaxial load was modeled using FEA, PD and MD as shown in Figure 48. In all these three models the graphene bar was fixed at one end and the other end was displaced with the velocity of 0.1 \AA/fs . The Young's modulus and shear modulus were considered to be 1.03 TPa and 0.4 TPa , respectively. The y-displacements at $y=20 \text{ \AA}$ were recorded while varying the distances along the x-direction within the range of 2 \AA to 12 \AA .

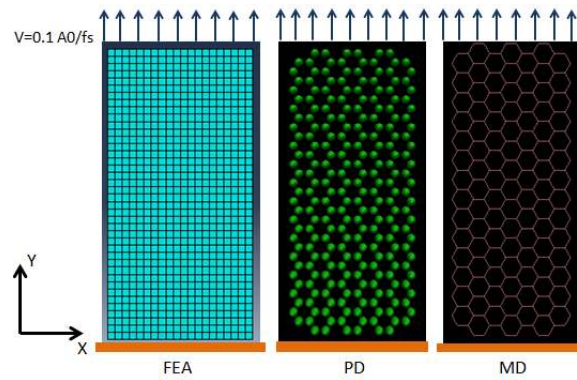


Figure 48. Different graphene sheet models

The y-displacements obtained from PD, MD and FEA at location $y = 20 \text{ \AA}$ and $x = 2 \text{ \AA}$ to 12 \AA are shown in Figure 49a. The average y-displacements along x-axis were seen to be approximately 0.4 \AA in both PD and MD models. But the y-displacements obtained from FEA were seen to be comparatively higher (0.5 \AA). In Figure 49b, the y-displacements are shown at a midpoint ($x=10 \text{ \AA}$, $y=30 \text{ \AA}$) as a function of time. The displacement from FEA is also seen to be slightly higher than the displacement obtained from PD and MD. A very good agreement is

seen between PD and MD simulation at the atomistic scale. This is possibly due to the fact that both PD and MD are based on nonlocal formulation of solid mechanics whereas the continuum model (FEA) relies on the local formulation [38].

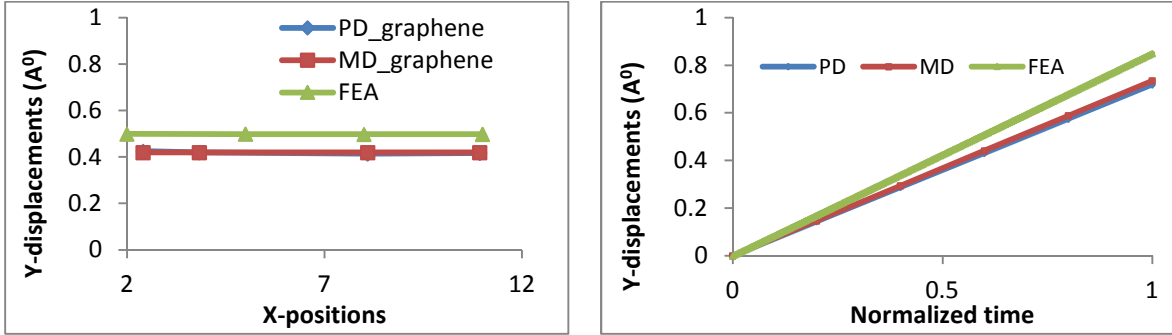


Figure 49a. Y-displacements at different X-locations, Figure 49b. Y-displacements at different timesteps

5.4.2 Case-II

In case-II, graphene sheets were considered with an edge crack. The objective was to compare the crack opening displacement (COD) in multiscale frameworks. It is to be noted that fracture and crack growth were not considered in this models. Here COD represents opening of the crack near the crack tip in y-direction. The PD and FEA models of graphene were considered to be larger than the molecular model (MD) as shown in Figure 50. The length and width of FEA and PD models were 100 A⁰ and 50 A⁰, respectively whereas the length and width of the MD model were 40 A⁰ and 20 A⁰, respectively. In all these three models (FEA, PD & MD), the edge crack width was same (5 A⁰). The FEA and PD models were fixed at one end while the other end was subjected to a velocity of $v_0 = 0.1$ A⁰/fs. The developed pressure in the PD model was applied as an external pressure on the MD model considering PFHMM formulation. The crack

lengths were 20 \AA in FEA and PD models and 4 \AA in MD model. The average pressure of 6511 atm was developed in PD model which was applied in MD model.

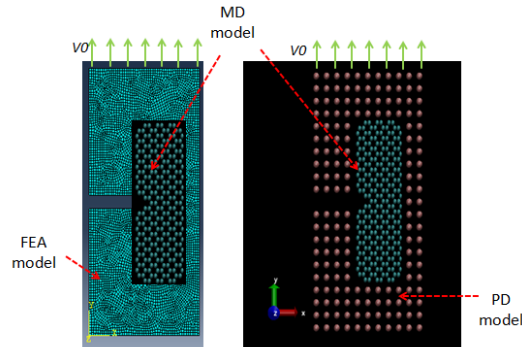


Figure 50. FEA, PD and MD models with an edge crack in graphene

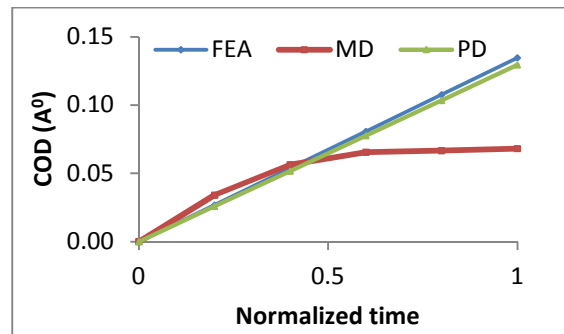


Figure 51. COD vs. time at $x=19 \text{ \AA}$ near crack tip

The crack opening displacements (COD) from these models were compared. Figure 51 shows the COD vs. time plots at $x=0$ obtained from both PD and FEA models. The COD from FEA and PD model is recorded at $x=19 \text{ \AA}$ along the crack length (20 \AA) whereas the COD from MD is determined at $x = 0$ along the crack length (4 \AA) of MD model. As a result in Figure 51, the locations of COD in FEA, PD and MD models are very close to each other near the crack tip.

The COD in MD model is seen to be increasing nonlinearly during first half of the time interval and then gradually it became almost asymptotic to the x-axis. Although, the COD from FEA and PD was observed to be linear during the complete time interval. A good agreement is seen between FEA, PD and MD at the early stage but later MD simulation deviated from PD and FEA. The crack length in MD model was comparatively smaller than PD and FEA model. The MD model was subjected to deform under NPT ensemble under external pressure (6511 atm). The discrepancy in COD among MD, PD and FEA models in the second half of the time interval is possibly due to the equilibration of interaction forces between PD and MD over the simulation time.

Besides the above analysis, COD was also compared between the peridynamics, atomistic and finite element models of graphene with edge crack. As shown in Figure 52, the length and width in both of the models were 40 \AA and 20 \AA , respectively. The length and width of the edge crack was 4 \AA and 5 \AA , respectively. One end was fixed while other end was subjected to velocity of 0.1 \AA/fs . According to Figure 54, the COD from MD and PD are observed to be smaller than the one from FEA. The COD from PD and MD models had very close agreement. This is possibly due to the non-local formulation and discrete geometry in the atomistic as well as peridynamics model. Similar type of observation was made in the work by Cao and Chen [60]. They studied buckling of CNT by using FEA and MD simulation. The deformation in FEA was seen to be higher than the deformation in MD model. The discrete nature in the atomistic model of CNT compared to continuous and smooth geometry in FEA model was considered to be the primary reason behind this discrepancy. Seleson and coworkers also observed the difference between displacements from classical continuum and atomistic

models [38]. Based on their study, the nonlocal formulation in PD and MD models may be considered for such discrepancy.

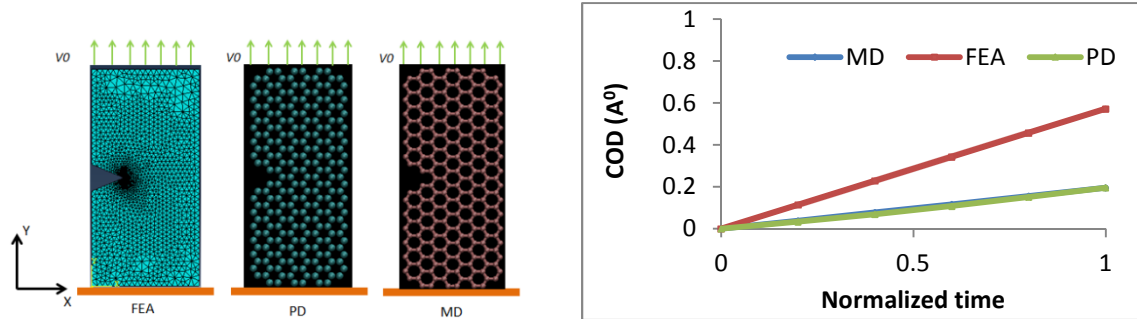


Figure 52. (Left) FEA, PD and MD model of graphene sheet, Figure 54. (Right) COD (at $x=0$ along the crack length) from FEA, PD and MD models

5.5 Conclusion

In this part of the work a coupling framework PFHMM has been established between PD based continuum model and fine scale molecular model. Multiple PD based continuum models and a coarse grain atomic model are embedded in the system to ensure smooth coupling between PD and MD region. Both top-down and bottom-up scales were considered. The mathematical formulations have been provided for peridynamics, coarse grain and atomistic models along with schematic explanations. PFHMM has been demonstrated considering three cases such as i) 2D plate under axial load and ii) 2D plate with an edge crack under axial load and iii) 3D nanoindentation problem. Average pressure and displacement fields at different scales were analyzed. By analyzing the displacement fields PFHMM is seen to establish smooth coupling among different scales. Both crack opening displacement (CTOD) and crack tip movement at different scales has been evaluated using PFHMM framework. The results show reasonable agreement between PD and atomistic models.

6. CONCLUSION

A theoretical framework has been established for predicting mechanical properties of graphene/epoxy and graphene/cellulose nanocomposites using atomistic model. The molecular dynamics based modeling was able to predict the Young's modulus and interfacial properties of nanocomposites. Effects of graphene concentration, aspect ratio and agglomeration were investigated. Theoretically calculated results were compared with the experimental data. Further, the atomistic scale model was integrated with continuum model by developing a atomistic-continuum coupling framework. In order to pursue this idea a "Peridynamics based framework for hierarchical multiscale modeling" (PFHMM) was developed. PFHMM was demonstrated in case studies relating 2D and 3D epoxy, graphene and graphene-epoxy nanocomposites.

REFERENCES

1. Sasha Stankovich, Dmitriy A. Dikin, Geoffrey H. B. Dommett, Kevin M. Kohlhaas, Eric J. Zimney, Eric A. Stach, Richard D. Piner, SonBinh T. Nguyen and Rodney S. Ruoff (2006), Graphene-based composite materials, *Nature*, **442**, 282-286
2. Leach. Andrew, R. Molecular Modelling: Principles and Applications (1997), *Addison Wesley*
3. K.S. Novoselov and A.K Geim, S.V. Morozov, D. Jiang, Y. Zhang, S.V Dubonos, I.V. Grigorieva, A. A Firsov, (2004), Electric Field Effect in Atomically Thin Carbon Films, *Science*, **306**, 666-669
4. Wu, Chaofu and Xu, Weijian. (2006), Atomistic molecular modeling of crosslinked epoxy resin, *Polymer*. **47**: 6004-6009
5. Fan, Bo, Hai and Yuen, M.F. Matthew. (2007), Material properties of the cross-linked epoxy resin compound predicted by molecular dynamics simulation, *Polymer*. **48**: 2174-2178
6. Bandyopadhyay, Ananyo., Jensen, D., Valavala K. Pavan and Odegard M. Georgory. (2010), Atomistic modeling of cross-linked epoxy polymer, presented at 51st AIAA/ASME/ASCE/ASC Structures, Structural Dynamics and Materials conference, 12-15th April, 2010
7. Wei Chen, Gary C. Lickfield, Charles Q. Yang, (2004), Molecular modeling of cellulose in amorphous state. Part I: model building and plastic deformation study, *Polymer*, **45**: 1063-1071
8. Favier, V.; Canova, G. R.; Cavaille', J.-Y.; Chanzy, H.; Dufresne, A., (1995) Gauthier, C. Nanocomposites materials from latex and cellulose whiskers. *Polym. Adv. Technol.* **6**: 351-355
9. Shoichiro Yano, Hyoe Hatakeyama' Tatsuko Hatakeyama, (1976), Effect of hydrogen bond formation on dynamic mechanical properties of amorphous cellulose, *Journal of applied polymer science*, **20**: 3221-3231
10. Hao Bu, Yunfei Chena, Min Zou, Hong Yi, Kedong Bi, and Zhonghua Ni, (2009), Atomistic simulations of mechanical properties of graphene nanoribbons, *Physics Letters A*, **373**: 3359-3362
11. Frank, I. W.; Tanenbaum, D. M.; van der Zande, A. M.; McEuen, P. L., (2007), mechanical properties of suspended graphene sheets, *J of Vac Sci and Technol B*, **25**: 2558
12. Changgu Lee, Xiaoding Wei, Jeffrey W. Kysar, and James Hone, (2008), Measurement of the Elastic Properties and Intrinsic Strength of Monolayer Graphene, *Science*, **321**: 385-388

13. F. Liu, P.M. Ming, J. Li, (2007), *Ab initio* calculation of ideal strength and phonon instability of graphene under tension, *Phys Rev B*, **76**: 064120
14. C D Reddy, S Rajendran and K M Liew. (2006), Equilibrium configuration and continuum elastic properties of finite sized graphene, *Nanotechnology*, **17**: 864
15. Y. Huang, J. Wu, and K. C. Hwang, (2006), Thickness of graphene and single-wall carbon nanotubes, *Phys. Rev. B*, **74**: 245413
16. K. V. Zakharchenko, M. I. Katsnelson, and A. Fasolino, (2009), Finite Temperature Lattice Properties of Graphene beyond the Quasiharmonic Approximation, *Phys. Rev. Lett.*, **102**: 046808
17. Yu, Suyoung., Yang, Seunghwa., and Cho, Maenghyo. (2009), Multi-scale modeling of cross-linked epoxy nanocomposites, *Polymer*. **50**: 945-952
18. Zhu, R., Pan, E. and Roy, A.K. (2007), Molecular dynamics study of the stress-strain behavior of carbon-nanotube Epon 862 composites, *Materials science and engineering A*. **447**: 51-57
19. Franklans S.J.V, Harik V.M., Odegard G.M., Brenner D.W., and Gates T.S. (2003), The stress–strain behavior of polymer–nanotube composites from molecular dynamics simulation, *Composites Science and Technology*, **63**: 1655-1661
20. Yasmin, Asma., Daniel, M. Issac. (2004), Mechanical and thermal properties of graphite/epoxy composites, *Polymer*. **45**: 8211-8219
21. Ji. Xiang-Ying; Cao. Yan-Ping; Feng, and Xi-Qiao.(2010), Micromechanics prediction of the effective elastic moduli of graphene sheet-reinforced polymer nanocomposites , *Modelling and Simulation in Materials Science and Engineering*, 16:45005-45020
22. Rafiee MA, Rafiee J, Wang Z, Song H, Yu ZZ, and Koratkar N.(2009), Enhanced mechanical properties of nanocomposites at low graphene content, *ACS Nanoletters*, 3(12):3884-90
23. Amnaya P. Awasthi, Dimitris C. Lagoudas, Daniel C. Hammerand. (2009), Modeling of graphene–polymer interfacial mechanical behavior using molecular dynamics, *Modelling and Simulation in Materials Science and Engineering*, 17: 015002
24. Liao, Kin; Li, Sean. (2001), Interfacial characteristics of a carbon nanotube–polystyrene composite system, *Applied Physics Letters*, 79: 4225 – 4227
25. E. Saether¹, V. Yamakov and E. H. Glaessgen, (2009), An embedded statistical method for coupling molecular dynamics and finite element analyses, *Int. J. Numer. Meth. Engng*, 78:1292–1319

26. Gumbsch P, Beltz GE., (1995), On the continuum versus atomistic description of dislocation nucleation and cleavage in nickel, *Modelling and Simulation in Materials Science and Engineering*, **3**: 597
27. Broughton JQ, Abraham FF, Bernstein N, Kaxiras E., (1999) Concurrent coupling of length scales: methodology and application. *Physical Review B*, **60**: 2391
28. Miller RR, Tadmor EB., (2002), The quasicontinuum method: overview, applications and current directions. *Journal of Computer Aided Materials Design*, **9**: 203
29. Steinmann P, Elizondo A, (2007), Sunyk R. Studies of validity of the Cauchy–Born rule by direct comparison of continuum and atomistic modelling. *Modelling and Simulation in Materials Science and Engineering*, **15**:S271
30. Xiao SP, Belytschko T., (2004), A bridging domain method for coupling continua with molecular dynamics. *Computer Methods in Applied Mechanics and Engineering*, **193**:1645
31. Onate E, Idelsohn S, Zienkiewicz OZ and Taylor RL (1996), A Finite Point Method in Computational Mechanics. Applications to Convective Transport and Fluid Flow. *Int. J. Numer. Methods Engrg.*, **39**: 3839-3867
32. Wu Z (1992), Hermite-Birkhoff interpolation of scattered data by radial basis function, *Approx. Theory Appl.*, **8**: 1-10
33. Belytschko T, Lu YY and Gu L (1994), Element free Galerkin methods, *International Journal for Numerical Methods in Engineering*, **37**: 229-256
34. Wang JG and Liu GR, (2002), A point interpolation meshless method based on radial basis Functions, *Int. J. Numer. Meth. Eng.*, **54**: 1623-1648
35. Liu GR and Gu YT, (2001a), A point interpolation method for two-dimensional solids, *Int. J. Numer. Meth. Engng*, **50**: 937-951
36. Liu GR and Gu YT, (2001b), A local radial point interpolation method (LR-PIM) for free vibration analyses of 2-D solids, *J. of Sound and Vibration*, **246**
37. S.A. Silling, M. Zimmermann and R. Abeyarante, 2003, Deformation of peridynamic bar, *J. of Elasticity*, **73**: 173-190
38. Pablo Seleson, Michael L. Parks, Max Gunzburger and Richard B. Lehoucq, 2009, Peridynamics as an upscaling of molecular dynamics, *Multiscale modeling and simulation*, **8**: 204-227
39. Sulsky, D., Chen, Z., & Schreyer, H. 1994, A particle method for history-dependent materials. *Computational Methods in Applied Mechanics and Engineering*, **118**: 179-196

40. York, A. R., Sulsky, D., & Schreyer, H. L, 2000, Fluid-membrane interaction based on the material point method. *International Journal for Numerical Methods in Engineering*, **48**: 901-92
41. Guilkey, J., Harman, T., Xiz, A., Kashiwa, B., & McMurtry, P, 2003, An eulerian-lagrangian approach for large deformation fluid structure interactions problems, part I: Algorithm development. In *Proceedings of the Second International Conference on Fluid Structure Interaction*, Cadiz, Spain
42. Zhang, H., Wang, K., & Chen, Z, 2009, Material point method for dynamic analysis of saturated porous media under external contact/impact of solid bodies. *Computational Methods in Applied Mechanics and Engineering*, **198**: 1456-147
43. Wieckowski, Z, 2004, The material point method in large strain engineering problems. *Computer Methods in Applied Mechanics and Engineering*, **193**: 4417-4438
44. Tan, H. & Nairn, J. A, 2002, Hierarchical, adaptive, material point method for dynamic energy release rate calculations, *Computer Methods in Applied Mechanics and Engineering*, **191**: 2095-2109
45. Daphalapurkar, N. P., Lu, H., Coker, D., & Komanduri, R., 2007, Simulation of dynamic crack growth using the generalized interpolation material point (gimp) method, *International Journal of Fracture*, **143**: 79-102
46. Gilmanov, A. & Acharya, S., 2008, A computational strategy for simulating heat transfer and flow past deformable objects, *International Journal of Heat and Mass Transfer*, **51**: 4415-4426
47. Zhang, D., Zou, Q., VanderHeyden, W. B., & Ma, X., 2008. Material point method applied to multiphase flows. *Journal of Computational Physics*, **227**: 3159-3173
48. Ma, J., Lu, H., Wang, B., Hornung, R., Wissink, A., & Komanduri, R. 2006, Multiscale simulation using generalized interpolation material point (gimp) method and molecular dynamics (md). *Computer Modeling in Engineering & Sciences*, **14 (2)**: 101-117
49. Lu, H., Daphalapurkar, N., Wang, B., Roy, S., & Komanduri, R. (2006). Multiscale simulation from atomistic to continuum coupling molecular dynamics (md) with material point method (mpm). *Philosophical Magazine*, **86 (20)**: 2971-2994
50. S. Roy and A. Nair, "Concurrent Multi-scale Modeling of Nanoparticle Reinforced Polymers using Statistical Coupling of MD and GIMPM", special session on Nanostructured Materials, *Proceedings of the 52nd AIAA-SDM Conference*, Denver, CO, April 4-7, 2011
51. <http://www.sandia.gov/~mlparks/papers/PDLAMMPS.pdf>
52. Michael L. Parks, Richard B. Lehoucq, Steven J. Plimpton, and Stewart A. Silling, 2008, Implementing peridynamics in molecular dynamics code, *Computer physics communication*, **179**: 777-783

53. Sun H. Compass, 1998, An ab initio force field optimized for condensed phase applications Overview with details on Alken and Benzene compounds *Journal of Physical chemistry B*, **102** (38): 7338-7364
54. Zhu R., Pan E. and Roy, 2007 A.K. Molecular dynamics study of the stress-strain behavior of carbon-nanotube Epon 862 composites *Materials science and engineering A*; **447**: 51-57
55. Fan Feng, Cun. and Hsu Ling, Shaw. 1992 Application of the molecular Simulation technique to characterize the structure and properties of an aromatic polysulfone system. Mechanical and Thermal Properties *Macromolecules* **25** 266-270
56. Yu Suyoung., Yang Seunghwa., and Cho Maenghyo. 2009 Multi-scale modeling of cross-linked epoxy nanocomposites *Polymer* **50** 945-952
57. Pour-Sakhaee, A. 2009 Elastic properties of single layered graphene sheet, *Solid state communications* **149** 91-95
58. S.M.-M. Dubois, Z. Zanolli, X. Declerck, and J.-C. Charlier 2009 Electronic properties and quantum transport in Graphene-based nanostructures *Europian Physical Journal B* **71(1)** 1-24
59. <http://lammps.sandia.gov/>
60. Guoxin Cao and Xi Chen, 2006, Buckling of single-walled carbon nanotubes upon bending: Molecular dynamics simulations and finite element method, *Physical review B*, **73**: 1554351-10
61. Xiaodong Li, Hongsheng Gao, Wally A Scrivens, Dongling Fei, Xiaoyou Xu, Michael A Sutton, Anthony P Reynolds and Michael L Myrick, 2004, Nanomechanical characterization of single-walled carbon nanotube reinforced epoxy composites *Nanotechnology* **15**: 1416-1423
62. X. Chen, Max Gunzburger, 2011, Continuous and discontinuous finite element methods for a peridynamics model of mechanics, *Comput. Methods Appl. Mech. Engrg*, **200**: 1237-1250
63. S. Silling, 2000, Reformulation of elasticity theory for discontinuities and long-range forces, *J. Mech. Phys. Solids* **48**: 175–209

APPENDIX

A.1 Parametric study of cutoff distance in PD models

A 2D epoxy bar was considered for this analysis. The length and width of the bar was 10000 \AA and 5000 \AA , respectively. The lattice spacing was approximately $h = 301.2 \text{ \AA}$. Three different cutoff distances $\delta = 1.7h, \delta = 2.3h$ and $\delta = 3.3h$ were considered. The 2D bar is fixed at one end while other end was subjected to a velocity of 0.1 \AA/fs . The stress-strain responses were plotted in Fig. 4. The material properties $E=3.3 \text{ GPa}$ and $G=1.22\text{GPa}$ were incorporated in the model. The calculated Young's moduli from the stress-strain responses were 7.35 GPa , 3.9 GPa and 2.076 GPa for $\delta = 1.7h, \delta = 2.3h$ and $\delta = 3.3h$, respectively. It is seen that the Young's modulus increases with decreased cutoff distances. The most reasonable approximation is achieved when δ is approximately equal to $3h$.

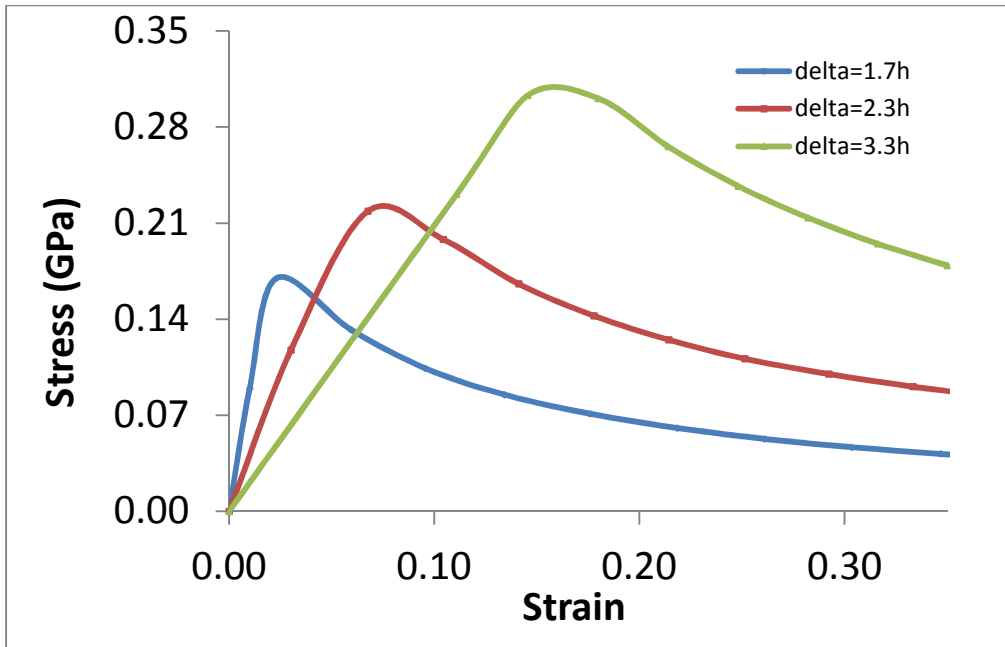


Figure 54. Stress-strain responses for different cutoff distances

In practice δ is chosen proportional to the grid size h , so that δ decreases as h decreases. In fact, such a strategy is even suggested in the paper that introduced peridynamics, where the choice of $\delta = 3h$ is recommended [62, 63].